Exoplanets and Asteroseismology: Know the star, know the planet

by

Thomas Samuel Harry North

A thesis submitted to the

University of Birmingham

for the degree of

DOCTOR OF PHILOSOPHY

High-Resolution Optical Spectroscopy (HiROS)

School of Physics and Astronomy

University of Birmingham

Birmingham, B15 2TT

February 2018

Abstract

This thesis primarily considers evolved exoplanetary systems through the use of asteroseismology as a tool to investigate the fundamental properties of the host stars, and the inferred planetary parameters. Of particular interest are the masses of evolved stars, and investigating how the available observables may bias the recovered mass estimates. Accurate and precise stellar masses are of critical importance. Whilst most of this work considers ensemble analysis, where relevant individual systems are considered, including a binary star system with an M dwarf and an asteroseismic red giant primary star. Another system of note is a transiting gas giant orbiting a red giant host, that will be consumed by the expansion of the host star. The metallicity distributions of evolved exoplanet hosts, and a suitable ensemble of field stars are also investigated using spectroscopy. This is to determine if evolved giant planet exoplanet hosts display the same metallicity excess seen in main sequence giant planet hosts. We fail to find a statistically significant excess in metallicity. Finally the noise properties of evolved stars are considered, including predicting the noise properties from stellar parameters, and how the elevated noise levels in evolved stars impact the detectable of planets around them.

Acknowledgements

This thesis would not have been completed without the help and support of many people in my life. Firstly, my parents, sister, and grandparents who have spent the last 20 years or so listening to me talk about space and planets all the time. Without their help and encouragement I would never have gotten here. Secondly, to my supervisor Bill Chaplin for putting up with me for another 4 years after supervising my Masters project and being extremely helpful and supportive throughout my PhD. Thirdly, to my officemates and all members of HiROS, but particularly James and Caitlin for helping me fix code and drink wine. Finally, a special mention should be made to Taylors coffee for sustaining me through the many long hours of writing and editing this thesis[1].

[1] see Upper (1974)

Contents

List of Figures

List of Tables

Structure of Thesis

This thesis is comprised of four analysis chapters in addition to an introduction and conclusion. These chapters cover five separate projects I have completed during my PhD. At the start of each chapter a detailed statement is given explaining the contribution of work by myself or collaborators for each project.

Chapters 2 and 5 have already been published (North et al. 2017b and North et al. 2017a respectively), where I am first author on both works. These chapters are reproductions of the published works, aside from minor formatting changes to comply with thesis regulations.

Chapter 3 is comprised of two separate works that share many analysis techniques. Both halves of the chapter are presented in a format commensurate with the structure of a paper. Two papers are in preparation and will be submitted soon. I shall be first and second author on these papers respectively.

Finally, Chapter 4 is also presented in a format similar to a paper, and is essentially a draft near to submission, that again I shall be first author on.

As some of the chapters are verbatim reproductions of published or works in preparation, there is a level of repetition between some of the introductory and analysis sections, in each chapter, and Chapter 1.

1 Introduction

While the majority of this chapter was written for the thesis, parts of Sec 1.9 were written for North et al. (2017a) and have been adapted from the introduction in that work to limit repetition.

1.1 Introduction

The night sky, and the vast emptiness of space has enthralled humanity for all of known history. What is the universe made of? Why do the stars shine? Why do some of them seem to wander across the sky whilst other appear fixed on the celestial sphere? Perhaps most fundamentally, what is our place in the universe and are we alone? It is only with the invention of the telescope that humanity began to unlock the heavens, with the true nature of the universe being far more fascinating than anyone could have imagined.

In this thesis we will encounter planets orbiting dying stars, and tackle some of the more contentious issues facing exoplanetary astronomy at present. We will use the signature of sound waves trapped inside the stars themselves to uncover their internal and fundamental properties, and discover how the noise signatures of a star can be estimated from its fundamental properties. A topic that will returned to several times throughout this thesis is the use of complementary data, or synergistic usage of the same data to achieve very different results.

Before we start on the main body of the thesis, the contents of each chapter and the main themes within are given in outline first.

Chapter 1 introduces all the concepts we will explore throughout this thesis, including; methods for detecting exoplanets (and their shortcomings), stellar evolution, asteroseismology and spectroscopy (and their relevant observables). Also covered is how stellar properties are recovered from stellar models used in conjunction with stellar observable parameters. Finally synergies between the separate fields of exoplanets and asteroseismology are possible, and the benefits to both fields. With these concepts introduced we move to the first analysis chapter.

Chapter 2 immediately introduces a difficult problem in astrophysics, measuring the mass of single stars, particularly evolved stars. If observables are compared to theoretical models to recover the stellar properties, any errors or biases in the stellar model can be compounded by issues in the method used to identify the correct model. Ultimately this can severely bias the recovered stellar mass and all subsequent analysis from this, such as the occurrence rate of planets or the inferred properties of any planets orbiting these stars. In this chapter we focus on the impact of space-based asteroseismology on the recovery of stellar masses for a sample of red giants that have been previously subject to long-term radial velocity observations to detect any planets.

Chapter 3 keeps us on the theme of evolved stars, incorporating the synergies of asteroseismology and exoplanet science. We look at the potential exoplanet host KOI-6194, believed to be a giant planet on a relatively short period orbit around a red giant star. The unusual binary system KOI-3890 is also studied, a system composed of a red giant star with a low mass dwarf binary component on a highly eccentric orbit. In this system the dwarf star is beginning to tidally distort the primary star, as the primary continues to evolve and expand. This distortion creates a "heartbeat" in the lightcurve of the primary star.

In Chapter 4 we take a break from asteroseismology, and use spectroscopy to investigate another intriguing property of exoplanet hosts. As an ensemble they appear to possess higher levels of elements heavier than helium than non-hosts.

Using a homogeneous set of spectroscopic data, we investigate the validity of this theory, when applied to giant stars, with giant planets.

In Chapter 5 we use asteroseismic scaling relations, to investigate, and predict the noise levels of evolved stars, and impact of this noise on the detection of exoplanets these evolved giant stars. Finally the thesis is concluded in Chapter 6.

1.2 History of stellar and planetary astronomy

Since prehistoric times, 6 of the planets in the Solar System have been known for "wandering" across the sky – with the word planet deriving from the Greek for wanderer. The discovery of Uranus and Neptune (and Pluto) would have to wait until the invention of large telescopes. It was with the introduction of the Copernican model of a heliocentric (centred on the Sun) universe during the Renaissance, that astronomy began to enter the modern realm of scientific thought. This was expanded upon by the work of Galileo, who was the first to observe bodies that did not appear to orbit the Sun, in this case the four major moons of Jupiter, now known as the Galilean moons.

Galileo can also be credited with the some of the first observations of the Sun through a telescope, and showing that sunspots were features on the "surface" of the Sun, rather than orbiting bodies. The apparent motion of the sunspots across the visible face of the Sun also proved that the Sun rotated about an axis, not the static, unchanging body it was considered in antiquity.

1.2.1 Existence of planets outside the Solar System

The first scientific work towards detecting planets around other stars outside the Solar System (hence exoplanet) would have to wait for advanced telescopes to be developed in the mid to late 20th Century, with claimed detections around the nearby M-dwarf Barnard's Star (van de Kamp, 1963, 1969), which were later refuted (Gatewood & Eichhorn, 1973). Dedicated surveys using large telescopes and sensitive spectrographs started in the 1980s, with several detections of radial velocity

variations consistent with planetary masses (Campbell et al., 1988; Latham et al., 1989), (see Sec 1.5.3) before the first confirmed detection of a planet around a solar-like star, 51 Pegasi b (Mayor & Queloz, 1995). With the advent of long-term ground and space based surveys to discover exoplanets, thousands of new worlds have now been found (Batalha, 2014; Fischer et al., 2014). Whilst many of these worlds are unlike any planet seen in the Solar System, they can still be broadly classified into types, based upon fundamental properties. We will introduce the different classes of planets, and methods for observing them, before moving onto stellar physics and asteroseismology.

1.3 Types of planets

1.3.1 Types of planets and formation

Broadly speaking, a planet's characteristics are entirely determined by the mass gathered during the turbulent era of its formation and its proximity to its host star. The composition of elements making up the planet also play a role, particularly for smaller planets. If a gravitationally unstable molecular cloud collapses, to form a stellar system, conservation of angular momentum prevents some material from collapsing onto the star. Instead a disk is formed around the forming protostar. It is this material that forms planets, and a means by which planet formation can be considered a natural consequence of star formation.

Since planets require heavy elements to form (carbon, silicon, oxygen, iron etc), it is believed that the very first stars (the not yet observed Population III stars) would have not harboured planets. However once they exploded as supernovae, heavier elements were released into the universe to form the seeds of planets. One of most exciting discoveries of the *Kepler* mission was the system Kepler-444 (Campante et al., 2015a), a star that is 11.2 Gyr old, that plays host to 5 small ($R \sim R_{\oplus}$) planets, thus suggesting planets have been common debris from star formation for most of the history of the universe.

Below I detail the different types of planets and broad outlines of one possible planet formation theory, namely the core accretion model (Lissauer, 1993; Pollack et al., 1996). The details are beyond the scope of this work, however the foundation is needed in later chapters when discussing occurrence rates and the properties of the planets around evolved hosts.

1.3.2 Terrestrial planets to mini-Neptunes

In the vicinity of the forming star near the centre of the disc, temperatures are higher and so volatile gases that constituted most of the stellar nebula such as hydrogen and helium cannot condense. This limits the inner planets to forming from the residual materials such as iron and silicates. This material self accumulates into boulder sized objects via electrostatic forces, at which stage gravitational forces begin to be significant. How these boulders form protoplanets is a major stumbling block in planet formation theory Once protoplanets have formed (Moon-Mars sized objects) the mass of material left in the vicinity of the forming planets determines what happens next. In the case of our Solar System, there was little remaining gas or dust in the inner parts of the system to sustain further planetary growth. Through a series of dynamical interactions, many of the planetary bodies in the inner Solar System collided, or were scattered out of the system entirely, until the 4 planets we know today remained (these interactions most likely leading to the formation of the Moon also).

In addition to this theory, and tied to the formation of the giant planets, is that the current terrestrial planets in our Solar System may represent a second generation of planets, formed after a so-called "Grand Tack" migration inwards and subsequent reversal by Jupiter (Masset & Snellgrove, 2001; Walsh et al., 2011; Batygin & Laughlin, 2015). The initial migration inwards would capture protoplanets inwards of the young Jupiter in resonances and deposit a significant fraction of the early inner protoplanetary disc into the Sun – either in the form of protoplanets or

gas and dust. This theory would explain several oddities of our Solar System; the lack of super-Earth mass planets or Hot Jupiter planets.

In planetary systems where an outer giant planet does not wander into the inner system, there remains extra material in the vicinity of the young star that allows the rocky planet to accumulate a little more mass, but there is insufficient gas to trigger runaway accretion (see below). This allows for the formation of higher mass terrestrial planets, so-called Super-Earths. At the high mass end of these types of planets ($M \leq 10M_{\oplus}$), small amounts of hydrogen and helium can be gathered from the surrounding nebula, with these planets generally called mini-Neptunes (Barnes et al., 2009; de Mooij et al., 2012), due to the more extended atmosphere, and lower average density.

1.3.3 Gas/Ice giants

In the outer Solar System, there remained plenty of dust beyond the so-called "ice line", where temperatures drop sufficiently for ices (water, CO_2, CH_4 etc) to condense out of the nebula gas (Martin & Livio, 2012, 2013; Schlaufman & Winn, 2016). This additional material was gathered by the growing planetesimals, until the bodies grow to sufficient size $\geq 10M_{\oplus}$ to directly gather the lightest gases, hydrogen and helium, the primary constituents of the surrounding nebula. This triggers runaway growth, until the gas reservoir in the vicinity of the planet is depleted. Further dynamical interactions during this time can scatter some of these planets to larger orbits, where reduced gas density prevent these planets gathering appreciable gas envelopes. This is a current theory for the formation of Uranus and Neptune (Thommes et al., 2002) in our Solar System.

1.3.4 Remaining material

Remaining scattered throughout the early Solar System would have been a large quantity of planetesimals (mountain-sized objects) that would continue to impact all of the planets for a time. This material was either gathered by the planets,

ejected from the system (as is believed for the detection of an extrasolar asteroid Meech et al. 2017), or migrated into stable orbits. The modern day asteroid belt between Mars and Jupiter, along with the Kuiper Belt and Oort Cloud in the outer Solar System, are believed to be remaining remnants of this material.

1.3.5 Hot Jupiters

Hot Jupiters are giant planet in close proximity to the host star ($P < 10$days), in a region of space it is generally believed they cannot form in. The current theory states that giant planets form much like Jupiter, beyond the ice line, and undergo migrations inwards. There are several theories for how the migration occurs (Baruteau & Masset, 2013). Either the planet interacts with the surrounding gas in the protoplanetary disk, in a fashion to act as a torque on the planet, or planets interact dynamically with large scattering events occurring, sending at least one planet into the inner system, where it will either remain on an eccentric orbit, or tidal forces between the star and planet may circularise the planet's orbit at a smaller semi-major axis (Petrovich, 2015).

These planets are relatively rare with an occurrence rate around 1% (Johnson et al., 2010b; Fressin et al., 2013). There is tension between results from different detection methods however, and we will return to this topic in chapters 5 and 3. Since such proximity to their stars, they are highly probable to transit (with deep transits) and due to the large radial velocity signals they give due to their higher masses and proximity to the host star, they are over-represented in survey results, giving the illusion they are common, this is an example of an observation bias. This was particularly the case in the first large exoplanet surveys.

It is also possible that Hot Jupiters might over time lose their initial atmosphere, leaving only the massive core. CoRoT-7b may be an example of such a planet (Leitzinger et al., 2011; Ehrenreich et al., 2015). Possible subclasses of Hot Jupiters are "warm Jupiters", "hot Neptunes" and "inflated giants".

Warm Jupiters are also Jupiter sized planets, however they exist at higher orbital periods ($10 < P \lesssim 50$days), and so incident flux from the host star on the main sequence is lower than for hot Jupiters. Hot Neptunes on the other hand, are giant planets of similar masses to Neptune, on short period orbits. In literature there are further subclasses sometimes discussed, but I shall not be considering them. The evolved host discussed in Chapter 3 would qualify as a warm Jupiter, however due to the evolved state of the host star, the incident flux on the planet is comparable to that incident on hot Jupiters. There is additional debate if hot and warm Jupiters represent the same population, or require different formation and migration histories (Huang et al., 2016).

As they age and lose the heat generated and trapped during their formation, hot (and cold) Jupiters shrink in physical radius. It is possible to re-inflate these planets if the incident flux on them increases, for example, as the host stars evolves into a giant star and the luminosity increases dramatically (Lopez & Fortney, 2016; Grunblatt et al., 2016, 2017), this produces the final subclass of inflated giants.

1.3.6 Exotic planetary systems

Whilst the majority of exotic planet systems discussed in this thesis will be giant planets around solar-like main sequence, or red giant stars, more exotic planets and planetary mass objects are possible. I detail below a few particular examples for completeness. These planets are exotic in nature either due to post formation evolution of the system, or due to an unusual formation location.

1.3.6.1 Pulsar planets

Planets orbiting pulsar stars, supernova remnants of high mass ($> 8M_{\odot}$) stars have been found to host planets (Wolszczan & Frail, 1992), and were in fact the first exoplanets to be detected and confirmed. These planets were possibly formed from the supernova debris directly, or from the destruction of a low mass companion star (Bailes et al., 2011).

1.3.6.2 Sub-Dwarf B Star planets

Kepler 70 is an unusual multi-planet exoplanet host. It is a sub-dwarf B star (sdB). These are stars that during the expansion of the star onto the red giant branch somehow lose the outer layers of the star, exposing the contracted core of the star that is still undergoing helium fusion. Few other sdB stars are known to host planets, with V391 Pegasi the first detected sdB host (Silvotti et al., 2007). Whilst sdB stars are in themselves interesting, it is the presence of two extremely short period planets, having orbital periods 5.76 and 8.23 hours, around this star that are of particular note. Reported in Charpinet et al. (2011), it is believed these planets are the cores of giant planets that plunged deep into the red giant envelope of the star, and may have triggered the expulsion of the envelope regions. In this manner planets may directly influence the evolution of their hosts, a theme we will return to later in Chapter 3.

1.3.6.3 Circumbinary planets

It is also possible to form planets in stable orbits around binary star systems of various mass fractions. *Kepler* has discovered several such planets, including planets in the habitable zones of the binary system. One such example is Kepler 16b, a giant planet announced in Doyle et al. (2011). As might be expected, these systems require interesting dynamics to remain stable over astronomical timescales.

1.3.6.4 Free-floating (rogue) planets

These objects blur the line between stars and planets (see Sec 1.4 for more details). These objects have some similarity to mini-planetary systems, much like the moons of Jupiter or Saturn, scaled. They are also sometimes termed sub brown dwarf stars, depending on the mass of the object, but could also be planets that were ejected from stellar systems due to a dynamic interaction during formation or subsequently. Detecting and characterising these objects is difficult, due to the lack of illumination on the planet for direct imaging, nor the presence of a star to be influenced by the

presence of the object.

1.4 To be (a planet) or not to be?

Before we move to the body of the thesis, precisely what classifies as a planet should be defined further. There are two main arguments to consider, does the object ever undergo nuclear fusion during its life, and how did it form?

1.4.1 Nuclear burning limit

Objects below a mass of $\sim 75 M_J$ ($\sim 0.07 Ms$) never achieve the required internal pressure to ignite sustained hydrogen fusion in their cores and so can be considered failed stars, and are called brown dwarfs (Kumar, 1963). Below this mass threshold there are various other available fusion pathways that can be sustained for a portion of the object's lifetime (Kulkarni, 1997), particularly whilst the brown dwarf is young and still hot from formation. At the low mass limit, deuterium burning occurs, with a rule of thumb condition that objects of mass $M \gtrsim 13 M_J$ classified as brown dawrfs (Spiegel et al., 2011). However this does not consider the formation pathway of the object in question. Brown dwarfs of lower mass than $13 M_J$ are possible.

1.4.2 Formation pathway

The formation of planets is still an area of intense debate, with two leading theories; accretion and direct collapse. The distinction between the lowest mass brown dwarfs and the highest mass planets is a murky region around $M \approx 13 M_J$. It is believed that brown dwarfs form in a similar fashion to stars, through the direct gravitational collapse of a gas cloud (in the case of brown dwarfs, the gas cloud fragments and only a small region collapses to form the failed star). Planets are believed to form as a byproduct of this process. As the star forms a disk is formed around the collapsing protostar, due to angular momentum conservation. In this disk, dust can accumulate into grains, which self assemble into larger bodies. In this work all of the objects discussed are clearly distinguished between being stars and planets.

1.5 Detecting planets

Since planets are generally much smaller and less massive than the host star, as well as being non-luminous, directly imaging planets against the glare of the host star is typically the limiting factor, though advances in optical systems are expanding the ability to directly image planets (Kuzuhara et al., 2013).

As such most planets are detected indirectly, through the influence they have on the host star. I will only discuss two highly complementary methods of detecting exoplanets in detail, the transit method utilised by photometric surveys such as *Kepler*, and the radial velocity (also known as Doppler wobble) method, utilised by spectroscopic observations, such as used in the discovery of the first exoplanet to be found around a sun-like star 51 Pegasi b (Mayor & Queloz, 1995). Other methods are only briefly discussed after this.

1.5.1 Transits

If a planet passes in front of the star, as viewed from Earth, we see a transit, as the planet blocks a small percentage of the light from the star. The first transiting system discovered was HD 209458 b (Charbonneau et al., 2000). Whether or not the transit is seen from our vantage point is dictated by the solid angle the planet's shadow sweeps out on the sky. Figure 1.1 illustrates this.

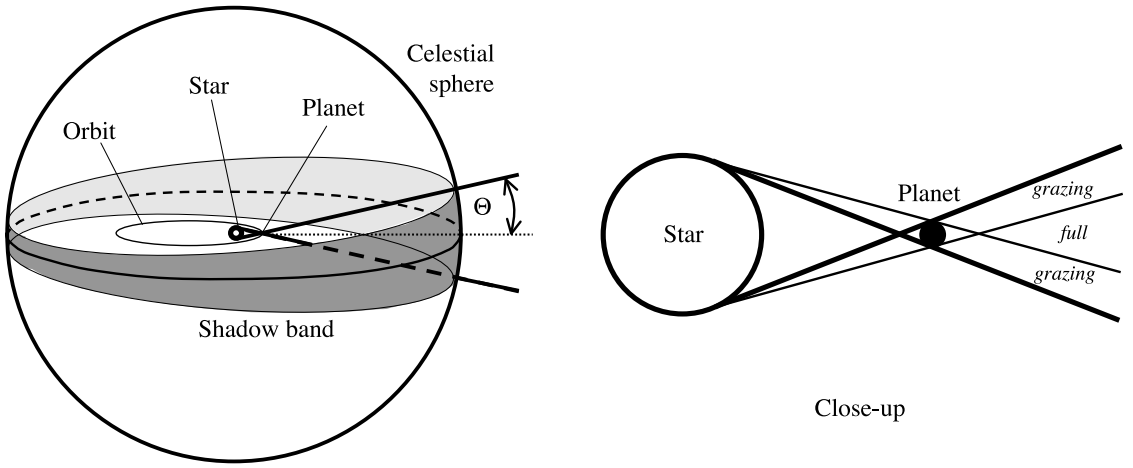

Figure 1.1: Areas of the sky that observe a transit. As can be seen, for eccentric orbits, the shadow bands covers a greater area of the sky at periastron. The close up on the right represents a flattened version of the geometry, and shows the cases where the transit would be grazing or full. Grazing transits occur within the penumbra, the cone defined by angle θ, with $\sin\theta = (R_\star + R_P)/a$ where a is the semi-major axis of the planet orbit, assuming circular orbits. Figure from Winn (2010)

As the figure shows, and is intuitively obvious, at periastron – the closest approach of the planet to the star – the shadow band covers the greatest portion of the sky.

Since a transit is a geometric alignment of host star, planet and observer, it is interesting to investigate the probability of observing a transit around any given star. This has important implications for the minimum size survey required to find a planet in a particular orbit.

The solid angle of the shadow band in Figure 1.1, assuming circular orbits, is,

$$\frac{4\pi(R_P + R_\star)}{a}, \tag{1.1}$$

where a is the semi-major axis of the planet orbit. To find the probability the band is along the required line of sight, this solid angle needs dividing by the total solid angle of the sky, 4π, to give the geometric transit probability. If the planet radius is also ignored, and assumed to be negligible compared to the stellar radius, the

probability becomes,

$$p_{\rm tran} = \frac{R_\star}{a}. \tag{1.2}$$

Barnes (2007) includes the effect of eccentric planets, and finds that the probability of detection is actually enhanced for eccentric planets, as seen in Eq 1.3 where e is the orbital eccentricity term.

$$p_{\rm tran} = \frac{R_\star}{a(1-e^2)}. \tag{1.3}$$

In the case of an Earth-like transiting system, the geometric probability of detection is 0.46%, which if inverted provides the average minimum number of systems needing to be observed to find a Earth like transit, 217 systems with solar-like stars, assuming all observed stars have an Earth-like planet on an Earth-like orbit. Obviously this is a simplistic argument, with every corrective factor included (such as true occurrence rate of Earth analog systems) increasing the number of systems required. Eq 1.2 also demonstrates an underlying bias in transit searches, i.e. for a given stellar radius, one is biased towards detecting close in planets as they have a higher probability of transiting.

Where on the star the planet appears to cross is called the impact parameter of the planet. It is defined by the angle of planet's orbit observed from Earth, relative to the plane of the sky (see Figure 1.2). The exoplanet convention is to define the plane of sky to be 0° whilst orbits that lie "edge-on" as seen from Earth are at an inclination of 90°. The relation of inclination to impact parameter can be considered by how closely the transit band intercepts the line of sight, i.e.

$$b \approx \frac{a\cos i}{R_\star} \tag{1.4}$$

where b is the impact parameter and is defined between 0 and 1, with $b = 0$ corresponding to a 90° inclination transit. In the above equation, the effect of eccentricity has been ignored, and also assumed is $R_P \ll R_\star$. The impact parameter is primarily

of interest in terms of validation of a planet, since high impact planets that transit close to the limb of the star are more likely to be false positives, most likely a misidentified eclipsing binary.

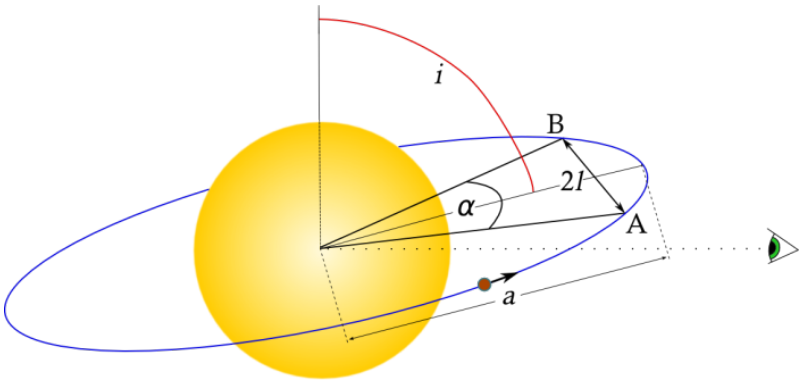

Figure 1.2: General geometry of a transit. i is the inclination of the planet relative to the plane of the sky. Therefore most transits are observed around $i = 90^o$. During a transit the planet passes through angle α, and for a small angle approximation, the chord and arc length between points A and B are considered the same.

It can be easily shown that the fraction of the star's light blocked by the planet ($\frac{\Delta F}{F}$, typically denoted as δ) is proportional to the ratio of the areas of star and planet (Winn, 2010),

$$\delta \approx \left(\frac{R_P}{R_\star}\right)^2, \tag{1.5}$$

where R_P and R_S are the planetary and stellar radii respectively. This relation is only approximate due to the star not being a uniformly illuminated body, nor the star or planet strictly being a perfectly spherical body due to rotation. The impact of the star not being uniformly illuminated is known as limb darkening (see below). Eq 1.5 also assumes that the planet is neither emitting, nor reflecting any light (an assumption that is typically valid during transit). In the case that the transiting body does possess intrinsic luminosity (e.g. a binary star system), the equation becomes,

$$\delta \approx \left(\frac{R_P}{R_\star}\right)^2 \left(1 - \frac{I_P}{I_\star}\right), \tag{1.6}$$

Figures 1.3 and 1.4 illustrate the transit detection process. The upper panel shows the raw lightcurve of Kepler-423, for 3 quarters of long cadence data (∼30min

integrations). The lower panel shows the lightcurve detrended and normalised around zero, such that transits register as periods of negative flux.

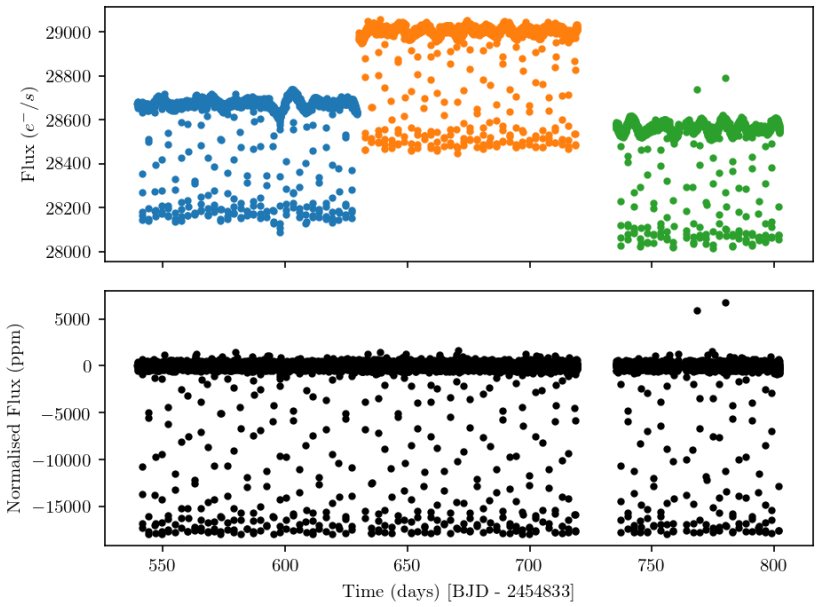

Figure 1.3: Upper: Kepler-423, raw lightcurve for 3 quarters of long cadence-∼30 minute integrations, showing a clear transit signature. Lower: detrended lightcurve normalised to zero flux.

One of the main issues in finding the planets is being able to efficient search the lightcurve for a small periodic signal caused by transits, without being thrown off by other signals. Whilst Figure 1.3 has been chosen to be detectable by eye, normally the method is automated, where efficient search algorithms are required. One method astronomers use is called the "box least-squares" (BLS) method (Kovács et al., 2002a), that describes the transit as either an inverted top hat function, or a trapezoid, and then rapidly searches for various widths, depths and periodicities of that shape in the lightcurve. Figure 1.4 shows the result of a BLS pipeline. The upper panel shows the strength of a signal at a given period. The lower plot is the lightcurve phase-folded on the best period the BLS search found. As expected it stacks the transits on top of each other. The upper panel also shows that such a search algorithm can be disrupted by aliases of the true period.

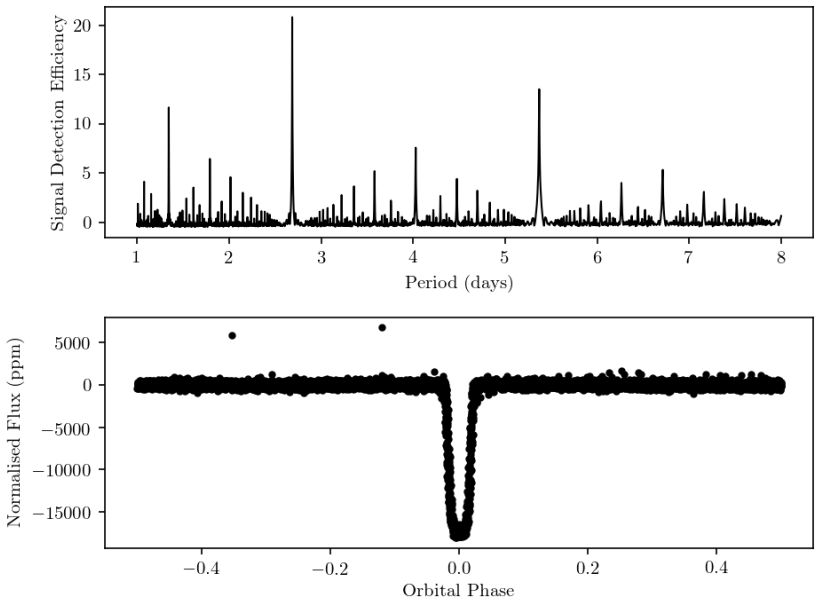

Figure 1.4: BLS search for a transit. A strong signal is found at ∼2.75days, and at the harmonic of that at 5.5days. The lower panel shows the lightcurve of Kepler-423 folded on the detected period, with the transit clearly visible.

The lower panel of Figure 1.4 also illustrates the impact of limb darkening on the shape of a transit. Photons emitted from near the limb (edge) of the star, in order to be detected on Earth, have to travel through more of the star's atmosphere to reach Earth, compared to those emitted from the centre of the disk. Since photons can be scattered in the stellar atmosphere, only those emitted higher in the atmosphere are able to escape to reach our detectors, so we cannot see to the same optical depth on the limb of the star as the centre. Therefore the "surface" of star is not a constant radius. The photons detected from the centre of the star are from greater depth inside the star, and subsequently from regions of higher temperature. This has the effect of the star appearing brighter in the centre of the disk. This can clearly be seen in an image of the Sun in Figure 1.5.

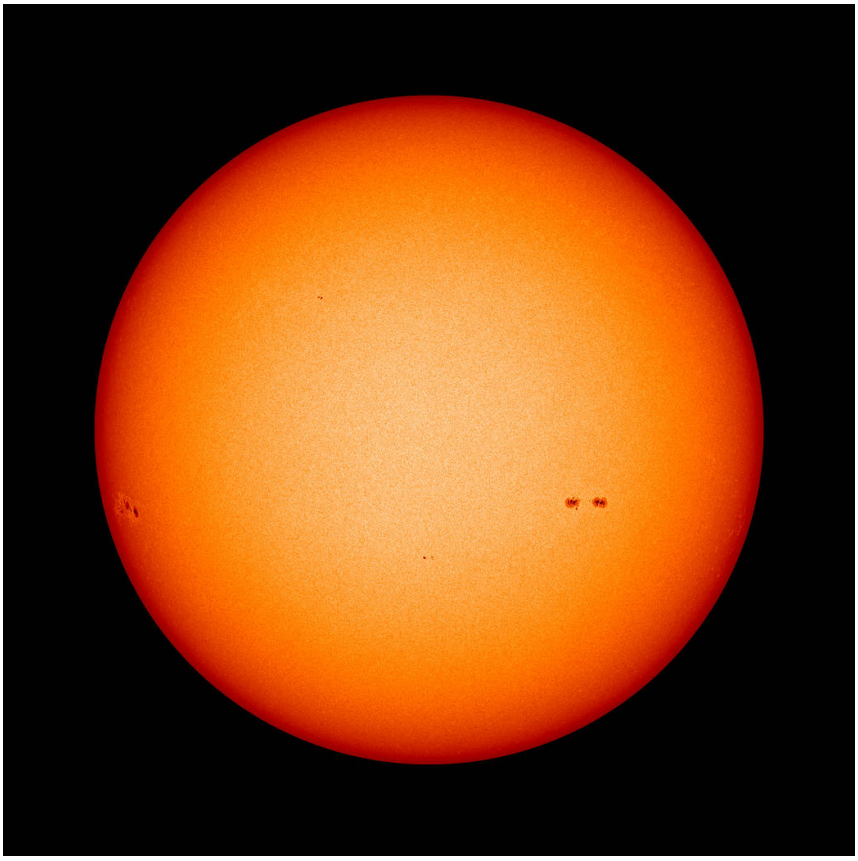

Figure 1.5: NASA Solar Dynamics Observatory image of the Sun, showing limb darkening, with the Sun brightest at the centre of the image, due to the line of sight allowing an external observer to see further into the photosphere of the star.

Without limb darkening the star would appear to be uniformly illuminated disk and a transit would appear as a trapezoid, with clear ingress and egress times, allowing for clear measurable transit times. Limb darkening blurs this out into a smooth curve. Figure 1.6 demonstrates the final impact of limb darkening on transits. If the planet transits the centre of the stellar disk, it is covering the brightest part of the star and so produces the deepest transit. Therefore for the same planet, slightly different observation angles on the transit shadow band see different latitudes of the star transited. This in turn produces different transit depths (and transit durations, due to a smaller chord of the star being transited). The upper panel shows the same system being observed in a narrow range of inclination angles with limb darkening. The lower panels shows the same system without limb darkening. The impact of limb darkening can be mitigated by observing at longer wavelengths

(see Figure 3 of Knutson et al. 2007).

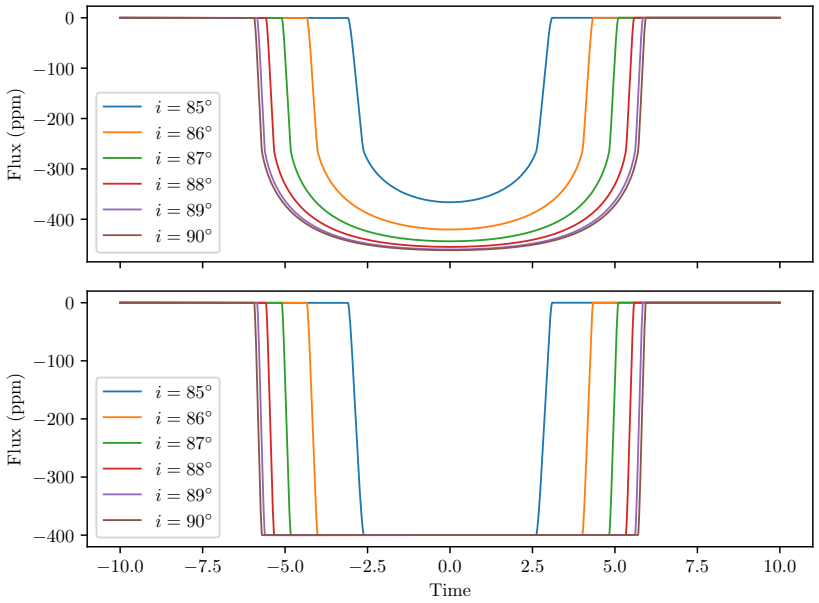

Figure 1.6: Limb darkening blurs trapezoidal transits into curves, and also impacts transit depth, with same system producing a deeper transit when transiting the centre of the stellar disk. At lower inclination angles, a shorter transit is also observed due to the planet transiting a chord of the star smaller than the diameter.

Limb darkening must be accounted for when fitting a transit model to observations. Different function forms exists to describe limb darkening, a quadratic form being popular. Many transit model codes either allow for the limb darkening parameters to be included as fixed or free parameters in the fitting procedure, with large tables of limb darkening for various stellar model atmospheres and missions available (Sing, 2010; Claret & Bloemen, 2011).

1.5.1.1 Sensitivity to e and ω

Transit observations also allow constraints on the shape of the orbit, described by the orbital eccentricity e and the argument of periastron ω, the angle between the position of nearest approach and the line of sight. Figure 1.7 shows the impact of varying ω for a series of model transits. Since for $e > 0$ the orbital velocity is no longer constant, the viewing angle of the orbit is now important. If the transit is observed near to periastron then the transit duration will be shorter (due to higher

orbital velocity) than for the equivalent $e = 0$ orbit (and vice-versa for a transit observed near apastron).

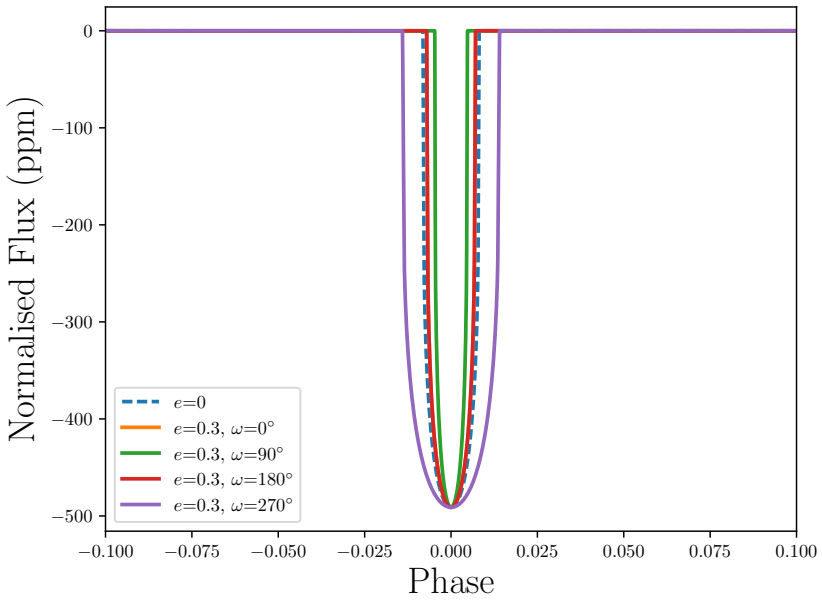

Figure 1.7: The dashed line is the model transit for a circular orbit. The other models are all at an eccentricity of $e = 0.3$, with varying ω, between 0° and 270°. Transits observed near apastron are longer than the circular case, despite the orbit being the same period, due to the lower orbital velocity.

1.5.2 Estimating stellar density

A planet transit also gives the opportunity to measure the mean stellar density, derived from Kepler's Third Law and the transit duration, (see Winn 2010),

$$\rho_\star + k^3\rho_p = \frac{3\pi}{GP^2}\left(\frac{a}{R_\star}\right)^3. \tag{1.7}$$

In the above equation, $k = R_p/R_\star$. This value is typically small and the second term on the left hand side is usually ignored. Therefore, transit photometry allows direct access to the mean stellar density. A caveat on the above equation is the assumption of circular orbits ($e = 0$). This is an important result we will return to in Sec 1.9.4 after considering other means of accessing the stellar density in Sec 1.9.

1.5.2.1 Biases and shortcomings of method

As with all forms of observations, large scale transit surveys suffer from biases. For a thorough review, see Gaidos & Mann (2013). If we return to the probability of detecting a transit, Eq 1.2, it is clear that for a fixed stellar radius, orbits on smaller semi-major axes have a higher probability of detection, which biases towards short period planets being detected. Typically three transits are required to confirm a detection of a planet to then be followed up. This limits the impact of false positive detections. If only one or two events were required, many false period detections would be made. E.g. a star with two dips in the lightcurve would generate a signal with a periodicity of the gap between the two dips, if only two "transits" were required. While it is possible to observe three transits in only two orbital periods, in most cases this limits any survey to orbital periods $P \leq T/3$ where T is the length of time the survey is in operation. In the case of the 4 year *Kepler* mission, that limits detections to orbital periods a little over a year. Eq 1.5 shows that a larger planet will have a significantly deeper transit, and so easier to detect. This biases towards giant planets. Additionally the same size planet will produce a much deeper transit around a smaller star. This limits the spectral types of stars that are typically searched for transits, to smaller, cooler stars of FGKM types. This constraint also means the giant stars are not typically included in transit surveys e.g. a $1R_J$ transit around a $1R_\odot$ star produces a $> 10 \times 10^4$ppm signal. Around a low luminosity red giant of just $4R_\odot$, the transit would be just ~ 650ppm.

Additionally any other signature that induces periodic variations in the lightcurve of a star can mimic a planetary signature, when it is in fact a false positive, or entirely hide the signature of a planet. Sunspots, a surface signature of stellar activity can produce similar brightness variations to that of a small planet, however they persist on the surface of a star for timescales of weeks, whereas a transit signal lasts only a matter of hours. A final problem can be the impact of contaminating light from other stars in the vicinity of the target star. In particular, eclipsing binaries in

the background can, when they contribute only a small fraction of the total light of the lightcurve, have the appearance of a transit of the object being imaged. Background eclipsing binaries are the primary source of false positives in *Kepler* data (Batalha et al., 2010). Background eclipsing binaries can also have eclipses last a similar timescale to that of a transit (on the order of ∼10hours for a Earth-like planet transiting a Sun-like star on a 1 yr orbital period).

The final shortcoming of the transit method is that it is insensitive to the mass of the planet directly. If the system contains multiple transits in close orbits then variation in the timing of the transits (TTVs) due to dynamical effects can help constrain the masses of the planets (Ballard et al., 2011), provided the system can be modelled accurately.

Normally a second independent detection is required to confirm the detection of a planet. Typically this is the "Doppler wobble" or radial velocity method, thereby not only confirming the presence of a periodic signal consistent with the transit signal, but also providing constraint on the planet radius and mass independently. However, additional transits of the same depth observed by a different observatory and wavelength are also accepted since transits are achromatic (Désert et al., 2015) e.g. Kepler-22b, which was observed by *Kepler* and *Spitzer* to confirm it as a planet, as radial velocity observations were unable provide a precise measurement of mass, just an upper limit (Borucki et al., 2012).

1.5.3 Dopper wobble

In a planetary system, all masses orbit the combined barycentre. For a multi-planet system, such as the Solar System, this is a complicated function of time. For a simple two body system on a circular orbit, the barycentre can be considered a fixed point around which both bodies orbit.

For systems with 3 or more bodies, the motion of the barycentre is a complicated pattern in space. Given the vast mass difference between stars and planets, the

barycentre typically lies inside or near to the star, which will appear to wobble in space due to the influence of any orbiting planets.

Typically these measurements are taken by comparing the observed spectral lines of a star against a known reference spectrum. The periodic red and blue shifting of the spectrum can be translated into a signal of a planet "wobbling" the host star. The size of the wobble induced by a Jupiter mass planet around a Sun-like star on a similar orbit to Jupiter is of the order 10ms^{-1}. For an Earth analogue i.e, Earth mass planet on a 1 year orbit, that signal is around 0.1ms^{-1}. One weakness of this method is that only the component of the wobble along the line of sight can be measured, as such only $M \sin i$ can be measured, unless there is independent constraint on the inclination of the planet. If the system also transits then it can be assumed that $\sin i \sim 1$ and so the inferred mass is close to the true mass. Otherwise the mass estimate is only the minimum possible mass.

For non-circular orbits, the shape of the velocity curve can also give strong constraint on the eccentricity and orientation of the orbit. Figure 1.8 shows several radial velocity curves for the same hypothetical planet, with the only change being the orbital eccentricity.

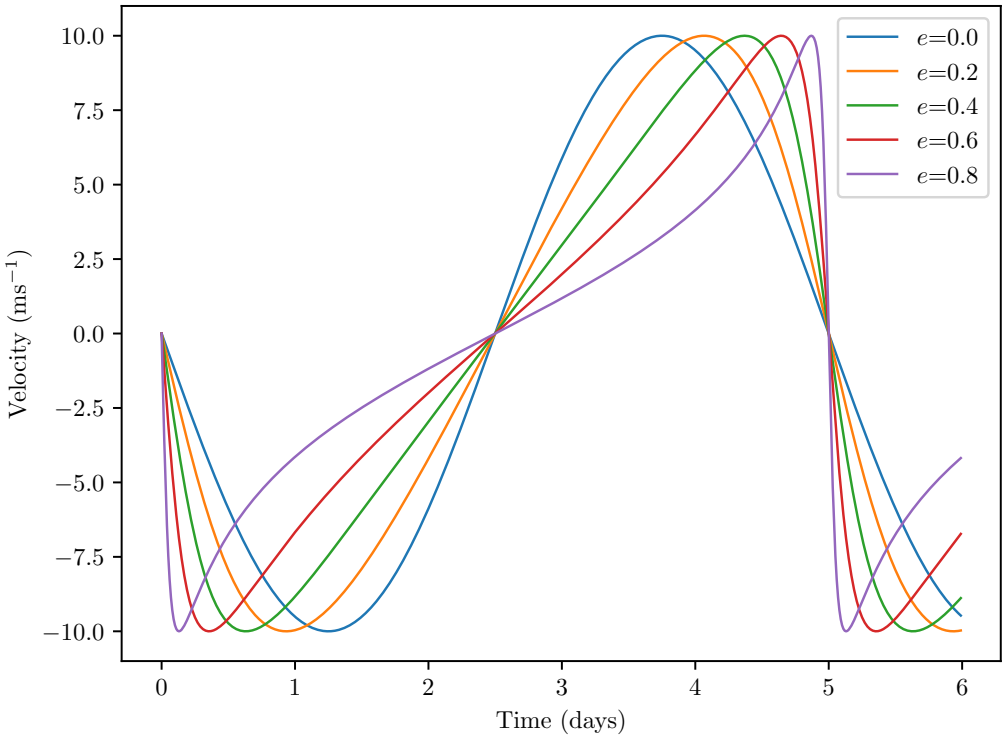

Figure 1.8: Model radial velocity curves for a planet inducing a 10ms^{-1} in its host star, for a variety of orbital eccentricities.

The equation governing the observed radial velocity curve of the star is,

$$V(t) = K(\cos f(t) + \omega + e\cos\omega), \tag{1.8}$$

where K is the semi-amplitude of the wobble, e the orbital eccentricity, and ω the argument of periastron. ω is related to the angle between the planet's position when closest to the star (periastron), and when the orbit crosses the reference plane. $f(t)$ is called the true anomaly, and is a complicated function of time and orbital eccentricity that must be solved numerically for cases where $e > 0$. For more information see Perryman (2011, Ch. 2).

K, the semi-amplitude, is related to the mass of planet by the following equation

Cumming et al. (1999, Eq. 1),

$$K = \left(\frac{2\pi G}{P}\right)^{1/3} \frac{M_P \sin i}{(M_\star + M_P)^{2/3}} \frac{1}{(1-e^2)^{1/2}}. \tag{1.9}$$

It should be clear from this equation that the mass of the planet M_P is not directly accessible from the semi-amplitude. However if the approximation is made that $M_P \ll M_\star$, then the denominator simplifies to $M_\star$, and the mass of the planet can be accessed, with only a $\sin i$ term remaining, due to the unknown system inclination i with respect to the line of sight. When combined with the transit method, constraint can be placed on all major planetary properties, as i may be inferred from the transit.

1.5.3.1 Biases and shortcomings of method

If we consider Eq 1.9 it is clear that for stars of the same mass either shorter period planets, or higher mass planets will produce the strongest signal. As such the method is biased towards detecting such hot Jupiter type planets. In a reversal of the situation for transits, the radial velocity method is particularly sensitive to the shape of the planet's orbit (P, e and ω), but not to the radius of the planet.

Again stellar activity can have severe effects on the detection of planets, and since the photometric lightcurve may not be available, separating a planetary signal from a stellar rotation induced signal can be extremely difficult, and false positive planets have been reported in literature (Robertson et al., 2014).

Rapidly rotating stars are also a problem for radial velocity observations, since the star is not resolved, and the spectrum observed is hence some average given by the contributions from across the disc of the star. As such, rapid rotation broadens the spectral line that is being measured. This somewhat limits the typical target selection for Doppler surveys to lower mass stars, which tend to rotate more slowly than their higher mass conunterparts. A final problem with higher mass stars is a lack of spectral lines, due to higher temperatures leading to most elements being

highly ionized.

Typically Doppler surveys target lower main sequence targets (see Butler et al. (2017) and references therein), as with transit surveys. However large scale surveys of giant stars are also possible, due to the slower rotation and cooler temperatures of these stars compared to when they were on the main sequence (Setiawan et al., 2004; Döllinger et al., 2007; Johnson et al., 2007a; Lee et al., 2014). This will be returned to in Chapter 2.

As with all observations, radial velocities measurements are subject to noise. For radial velocities it is known as "stellar jitter". This noise can be of astrophysical origin (such as granulation, or oscillations) or instrumental in nature (Wright, 2005; Isaacson & Fischer, 2010). In the case of lower mass main sequence stars, where convection is driving a stellar magnetic dynamo, signatures of activity are present in the velocity measurements and both stellar flares and sunspots can contribute to the jitter signature (Saar et al., 1998; Oshagh et al., 2017).

For more evolved stars, the dominant noise signature within radial velocity measurements are the stellar oscillations themselves (Udry et al., 2007; O'Toole et al., 2008). For giant stars, the amplitude of these oscillations can reach tens of metres per second (Kjeldsen & Bedding, 1995), which can severely impact the types of planets detectable around giant stars. To overcome the impact of jitter on observations, more observations are needed, across a longer baseline encompassing several orbital periods to ensure any detected planetary signal is genuine (Reffert et al., 2015).

The final shortcoming of the method, already mentioned, is that unlike transits very little information on the inclination of the system can be inferred. The only information available is that the planet has a velocity component along the line of sight, i.e. it does not orbit on the plane of the sky (see discussion of astrometry below). Due to the lack of constraint on inclination, the inferred mass of any planet is a lower limit on the true mass of the planet. This does leave potential for some of the giant planets currently considered planets to in fact be stellar or sub-stellar com-

panions. This is particularly relevant for companions found at orbital separations $a \gtrsim 3$AU, outside of the so-called "brown dwarf desert" (Grether & Lineweaver, 2006), this is an apparent paucity of brown dwarf companions on close orbits.

1.5.4 Other detection methods

There are additional methods of detecting exoplanets. If the star is relatively nearby, and the planet on a wide orbit, it is possible to directly resolve the planet, such the multiplanet system HR 8799 (Marois et al., 2008, 2010). To do so requires separating the small fraction of light reflected (or emitted) by the planet from the glare of the host star. This can be done using adaptive optics, in conjunction with a coronagraph to physically block the incoming light from the star.

Another method is astrometric wobble, which can be considered similar to the Doppler wobble, projected onto the plane of the sky. As the planet orbits the host, the star orbits around their combined barycentre, this small motion is detectable, with the current *Gaia* mission expected to detect several thousand exoplanets via this method (Perryman et al., 2014). The astrometric method measures the motion of the star itself directly, whilst the Doppler method as discussed above, measures the velocity of the star. The star is monitored photometrically, with an implicit assumption that any periodic motion in the centre of light from the star is indicative of a planetary companion, rather than blending or another false positive signal.

1.5.5 Characterising exoplanets

Since both the transit and Doppler detection methods are indirect, they rely on observations of the host star to infer the presence of a planet and as such characterising the planet is fundamentally tied to how well characterised the star is. This is a topic that will be returned to throughout this thesis. Do you want to know the radius of a planet from the transit depth at 5% precision? You need to know the stellar radius to higher precision than this. Want to claim a detection of a Earth-like planet in the habitable zone of a Sun-like star? You need to know the mass and

radius of the host star to high precision. In addition to this, the stellar luminosity would be needed to claim a habitable zone detection. This can be measured either from a precise parallax measurement, or through the stellar effective temperature and radius. Asteroseismology can be used to provide high precision stellar radii and masses, a clear benefit to exoplanetary science and the ability to predict the habitability of the exoplanet. Additional planetary parameters such as albedo, atmospheric composition and rotation would also have an impact on the habitability of a planet. The theme of synergies between asteroseismology and exoplanets will be explored further in Sec 1.9.

1.6 Planetary system evolution and destruction

Star and planet evolution are fundamentally linked. Whilst an exhaustive discussion of planet formation is beyond the scope of this work, we will briefly discuss what effect the evolution of a star will have on any planets orbiting it. A good review is given by Veras (2016) for the evolution of planetary systems after the host star leaves the main sequence.

1.6.1 Orbital migration during subgiant expansion

A topic we will return to throughout this thesis is that the distribution of stellar and planet properties around evolved stars does not match the distributions of planets around main-sequence stars of similar masses. One possible cause is the destruction/ingestion of planets as the star turns off the main-sequence and begins its evolution into a giant star. A more in depth discussion of stellar evolution is given in Sec 1.7. One theory is as the star evolves into a subgiant, the onset or expansion of surface convection zones leads to angular momentum of the orbiting planet being deposited in the star due to tidal forces, resulting in the in-spiral of the planet (Schlaufman & Winn, 2013). This theory has particularly been invoked to explain the lack of hot Jupiters seen orbiting evolved stars (Schlaufman & Winn, 2013). A final theory is that the masses of subgiant and giant stars have been overestimated

from spectroscopic properties. This topic is explored in Chapter 2.

1.6.2 Ingestion during RGB ascent

At larger orbital separation tidal forces are limited between the star and planet initially, and the star can evolve onto, and up the red giant branch before encountering the planet. Several planets doomed to be ingested by their star have been found by the *Kepler* mission (Huber et al., 2013a; Ciceri et al., 2015). These planets are expected to be ingested by their hosts in a few tens of millions of years, a relatively short timescale in astronomical terms. We return to this in Chapter 3

Planet ingestion has also been invoked to explain rapid rotation rates seen in some evolved stars (Massarotti, 2008; Carlberg et al., 2009), as well as enhanced levels of lithium detected in some giant stars (Sandquist et al., 2002; Adamów et al., 2012a).

In the case of our Solar System, the Earth's fate is uncertain, but is believed to end by being consumed by the evolving Sun (Rybicki & Denis, 2001; Schröder & Connon Smith, 2008; Veras, 2016). As the Sun evolves into a red giant, consuming Mercury and Venus in the process, it will expand to a maximum radius of 1.2AU, beyond the Earth's current orbit. Significant mass loss during the ascent of the RGB causes the planets orbits to spiral outwards. While this offers hope for the Earth to survive it would still be inside the solar atmosphere. The increased drag on the Earth, and tidal interactions with the expanded Sun will cause the Earth to spiral into the Sun. Mars is expected to survive. All the outer planets are expected to survive, on expanded orbits, until the end of solar evolution.

As we have seen throughout this section, the evolutionary status of the star has a strong impact on the observability, and indeed, existence of any planetary system. We will now move to look at stellar evolution and characterisation, across the main sequence and post main sequence evolution for stars $M \leq 2\mathrm{M}_{\odot}$.

1.7 Stars

When considered naively, stars are very simple objects. Self-gravitation is attempting to collapse the star, this is balanced by the pressure gradient inside a star exerting a force outwards against gravity. The pressure gradient itself is maintained by the temperature (and density) gradients inside the star, due to the nuclear reactions inside the core generating energy. This balance of forces – known as hydrostatic equilibrium – is maintained until the fuel in the centre of the star runs out. This is of course a very simple explanation, but serves as a good place to start. In the discussion below we will focus on relatively low mass mass stars, in the range $\sim 0.8 - 2 M_{\odot}$. While this is a narrow range in stellar mass it covers an important boundary in stellar physics, between stars with convective interiors (cores), and those with convective exteriors (envelopes). Whilst an exhaustive discussion of star formation and evolution is far beyond the scope of this thesis, the key points are discussed below, and the impact that internal stellar structure has on the evolution of the star during the main sequence and beyond.

1.7.1 Stellar formation and evolution

1.7.1.1 Formation: Gas cloud to main sequence

The beginnings of star formation are triggered by the collapse of a molecular cloud under its own gravity, possibly triggered by a perturbation from a nearby supernova (Cameron & Truran, 1977). This collapse may fragment into smaller concentrations, that will go on to form individual stars. Inside an individual fragment, the gas continues to collapse under it's own gravity, releasing gravitational potential energy radiatively. As gas density increases the cloud will become optically thick, raising temperatures and forming a protostar (Larson, 1969). As the outer parts of the cloud continue to collapse onto the forming protostar, simultaneously forming a protostellar disk, temperatures and internal pressures continue to rise until nuclear

fusion begins, initially deuterium fusion, but finally hydrogen fusion begins in the core. Any surrounding material in the near-stellar environment evaporates off, and the star settles onto the main-sequence. During this process, material (gas and dust) in the vicinity of the star also collapses to form a protoplanetary disk out of which planets of various sizes and orbits form, (see Sec 1.3.1).

1.7.1.2 Main Sequence Lifetime

The main sequence is the long-lived period of a star's life, as it fuses hydrogen to helium in the core. For stars below $M \leq 1.1\mathrm{M}_{\odot}$ the dominant fusion pathway is via the pp mechanism, whilst at higher masses (and so higher core temperatures) a catalysed fusion pathway, known as the CNO cycle, is the dominant energy source (Salaris & Cassisi, 2005). The amount of time a star of given mass will live on the main sequence can be approximated by

$$\tau_{\mathrm{MS}} \approx 10^{10} \left(\frac{M}{\mathrm{M}_{\odot}} \right)^{-2.5}, \tag{1.10}$$

where τ_{MS} is in years. This relation holds well for stars where the luminosity-mass relation can be expressed as $L \propto M^{3.5}$ which in turn is valid for stars $0.4\mathrm{M}_{\odot} \lesssim M_{\star} \lesssim 50\mathrm{M}_{\odot}$. The Sun has an expected main sequence lifetime of 10 billion years and is approximately halfway through this at the present epoch. For stars twice the mass of the sun, the highest mass stars we will consider in this thesis, the main sequence lifetime is approximately 1.75 billion years. During this time, the star is relatively stable, with the helium concentration slowly increasing in the core. Throughout the main sequence lifetime, the stellar effective temperature and luminosity rise. This has the consequence that the habitable zone of a star is not static throughout the main sequence lifetime, but time varying. If the luminosity of the Sun grows with time, it implies it was lower in the past. Lower solar luminosity would be insufficient to maintain current climate and atmospheric conditions on Earth, particularly the mostly ice-free liquid ocean. This conundrum is at the core of the so-called "faint

young Sun" problem (see Feulner (2012) and references therein). It is a conundrum due to geological records indicating that liquid water has been present on the surface of the planet for at least 3.8Gyr. A less luminous Sun would also be unable to maintain liquid water on the surface of Mars, which evidence suggests was present in the distant past.

It is at this point that the role of convection separates the future evolution of the star. Convection occurs in stars where the absolute value of the radiative temperature gradient is greater than the adiabatic temperature gradient.

$$\left|\frac{dT}{dr}\right| > \left|\frac{dT}{dr}\right|_{\rm ad} \tag{1.11}$$

Across the main sequence convection occurs in distinct regions of stars, dependent on mass. For low mass stars $M \lesssim 0.3\mathrm{M}_\odot$, the entire star is convective, and helium does not accumulate in the core of the star, instead the star will slowly evolve along the main sequence (using Eq 1.10 $\tau_{\rm MS} \sim 200$Gyr for a $0.3\mathrm{M}_\odot$ star) until nearly all hydrogen in the star has been fused, and then evolve directly to a helium white dwarf, without any giant phase of evolution (Laughlin et al., 1997).

Stars in the mass range 0.3-1.3$\mathrm{M}_\odot$ are composed of a radiative interior, overlaid by a convective envelope, with the convective envelope becoming thinner with increasing mass. Meanwhile in the core of the star, the CNO cycle is the dominant energy generation pathway for $M > 1.1\mathrm{M}_\odot$. The CNO fusion pathway has a higher temperature dependence than the pp cycle, and creates a stronger temperature gradient inside the core of the star. This in turn triggers the core to become convective ($M \gtrsim 1.3\mathrm{M}_\odot$), whilst the outer regions are radiative.

For all stars above $0.3\mathrm{M}_\odot$ once hydrogen runs out in the core region of the star where fusion can be sustained, the core will begin to collapse, due to a lack of internal pressure to support it against gravity. This contraction releases energy into the surrounding layers of star. The star has started to become a subgiant. Most of

the stars discussed in this thesis are subgiants and red giant stars

1.7.1.3 Subgiant to Red Giant

As the core contracts under gravity, the potential energy released heats the surrounding layers to the point that hydrogen fusion can begin in a shell surrounding the now mostly inert, non-degenerate core. Due to the lower pressure outside the core, a higher temperature is needed to sustain fusion. Since the rate of energy generation is temperature dependent, a higher temperature means the shell burning proceeds at a higher rate than the hydrogen burning in the core previously did, this subsequently shortens the timescale of shell burning relative to the main sequence lifetime of the star. This shell burning also triggers the expansion of the outer layers of the star, and a reduction in effective temperature. These factors combine to approximately maintain a constant luminosity across the subgiant branch of stellar evolution (Pols et al., 1998). The core contraction, and subsequent shell burning phase is relatively slow in low mass stars. Helium will continue to rain down on the core from the surrounding hydrogen burning shell, increasing pressure and density in the helium core. For stars of mass $M < 2\mathrm{M}_{\odot}$ the accumulation of helium in the core drives the core to the point that thermal pressure can no longer sustain it against gravity, and it at least partially collapses to a degenerate state of matter, supported against further collapse by quantum mechanical effects. This collapse also releases additional potential energy, driving the rate of shell burning up. At this point the star is about to transition to a red giant. For stars of $M \geq 1.3\mathrm{M}_{\odot}$, as the effective temperature of the expanding envelope drops, the opacity of the material increases to the point that convection takes over as the dominant energy transport mechanism. Lower mass stars are already convective. The luminosity of the star begins to rise rapidly, and the envelope expands, whilst roughly maintaining the same effective temperature. The star is now becoming a red giant.

1.7.1.4 Red giant to Asymptotic Giant Branch

At this point, a partially degenerate core composed of helium is surrounded by a thin hydrogen burning shell and an expanding convective envelope. As the hydrogen shell continues to deposit helium on the core, the conditions continue to increase in pressure. Under degenerate conditions, a rise in pressure produces a decrease in radius of the core, releasing more potential energy into the burning shell, which in turn drives up the nuclear reaction rate and temperature of the hydrogen shell. This is a runaway process. The energy in the burning shell is also increasing the temperature of the degenerate core, almost uniformly, due to the highly conductive properties of degenerate matter. As the rate of nuclear reaction in the shell accelerates, the luminosity of the star is rapidly increasing, and the radius of the star is increasing from around $5R_{\odot}$ at the base of the red giant branch (known as low luminosity red giants), to hundreds of solar radii, on a timescale of tens of millions of years, rapid in astronomical terms. The maximum extent of the Sun at this point in its evolution will most likely lead to the consumption of Earth (Schröder & Connon Smith, 2008) as noted previously.

Finally the core conditions become critical, and helium ignition begins rapidly. Due to the nuclear ignition occurring in degenerate conditions, temperature and pressure are mostly decoupled, and a runaway nuclear reaction occurs, as the temperature rises due to ignition, in turn accelerating nuclear reaction rates. This event is known as the helium flash, and occurs at the tip of the red giant branch. The core temperature continues to rise, until thermal pressure overcomes degeneracy pressure, and the core expands, this also producing a reduction in the radius of the envelope. The star now descends the red giant branch becoming a red clump star, with helium core burning, surrounded by a layer of hydrogen shell burning.

Whilst these stars are typically hotter than the red giant stars they formed from, distinguishing between them observationally is difficult. At the end of helium core burning, the star follows similar evolution as on the red giant branch, with

core contraction leading to a degenerate carbon and oxygen core, with helium and hydrogen burning shells above, and large envelope expansion – the star is now an asymptotic giant branch star. However, unlike with red giants, core conditions never ignite further stages of fusion for stars in the mass range we are considering ($M < 2\mathrm{M}_{\odot}$). Finally the star throws off its outer layers as a planetary nebula is a series of pulses, exposing the hot degenerate core that is now a white dwarf.

We now move on to discuss what observables are available throughout the star's life to characterise the star.

1.8 Stellar Observables

Whilst the previous section describes the evolution of a star, and its properties across time, in real life human observations are but a fleeting snapshot of a star's life. Reconstructing a single star's life from observations made on human timescales is analogous to recreating a movie from a single frame, with only the broadest outline of the plot to guide you. Fortunately there are multiple methods available to measure the properties of stars. One particular advantage over the movie analogy is the fact that there are many stars of the similar masses, but different ages observable in the sky. This allows for the testing of stellar evolution theories on all evolutionary states of stars at the same time. In this section we explore some of the different observables available through which a star may be characterised.

In this section, and throughout the thesis, we consider a stellar or planetary *parameter* to be an observable, e.g. stellar effective temperature or planetary transit depth. Stellar (and planetary) *properties* are considered to be fundamental aspects of the star or system itself, that cause the observables we see, but are not necessarily measured directly e.g. stellar radius or planet semi-major axis.

1.8.1 Parallax and Luminosity

If the position of the star is compared against distant background objects that can be considered static on the sky, then using the Earth's orbital radius as the base of

a right angled triangle, the distance to the star can be estimated directly from the angle the star moves through by,

$$\tan\theta = \frac{1\mathrm{AU}}{d}, \tag{1.12}$$

where d is the distance to the star. This measurement was possible at high precision for $\sim 10^5$ stars during the *Hipparcos* mission (Perryman et al., 1997). The current *Gaia* mission is expected to increase this number to $\sim 10^9$ stars with better than or similar precision to *Hipparcos* down to much fainter magnitudes. Parallax can be tied to the stellar luminosity, a fundamental property of the star, by the equation, (see Pijpers 2003):

$$\log_{10}\frac{L}{L_\odot} = 4.0 + 0.4M_{\mathrm{bol},\odot} - 2.0\log_{10}\pi[\mathrm{mas}] - 0.4(V - A_V + BC(V)). \tag{1.13}$$

In the above equation, parallax is given by π, visual magnitude V and interstellar extinction, the apparent reddening and dimming of stars due to interstellar dust, by A_V. The factor $BC(V)$ is the bolometric correction for the star, to account for the fact the the luminosity of a star is the integrated output over all wavelengths, whilst the measured magnitude V is over a narrow range of wavelengths.

Extinction can be difficult to measure, but there are now 3D maps of interstellar dust distributions throughout the Milky Way covering multiple wavelength bands (Schlegel et al., 1998; Schlafly & Finkbeiner, 2011; Green et al., 2015).

1.8.2 Spectroscopy

While certain classes of stars are amenable to asteroseismology (see Sec 1.9), the primary method of stellar classification remains spectroscopy. Spectroscopy draws on the work of Newton in showing white light is composed of multiple wavelengths perceived visually as white. If that light is dispersed by a grating or prism, the individual components can be separated and viewed. In the case of stars, while the

overall colour of a star can give information on the temperature, if that same light is passed through a prism, the chemical signature of a star can be measured, and through it the physical properties of the near-surface layers can be inferred.

Each constituent element present in the star will absorb and emit light at specific wavelengths, associated with the energies of the element's specific atomic transitions. If hot gas is overlaid by cooler gas (as is the case in a star's atmosphere) then the star's observed light will be interspersed with dark lines known as stellar absorption lines. The appearance of particular spectral lines and available transitions is associated with the mass, temperature, and composition of a star. The "spectral type" of a star has long been used as a means of classifying a star. Table 1.1 summarises the standard spectral types and some of their associated main sequence stellar properties. Figure 1.9 shows example model stellar spectra (Pickles, 1998) for a variety of spectral types.

Table 1.1: Table of spectral types and the typical associated masses and temperatures on the main sequence for each class.

Type[a]	Mass[b]($M_\odot$)	$T_{\rm eff}$ (K)
O	> 16	$> 30,000$
B	$2.5 - 16$	$12,000 - 30,000$
A	$1.5 - 2.5$	$7,200 - 12,000$
F	$1.05 - 1.5$	$6,000 - 7,200$
G	$0.8 - 1.05$	$5,300 - 6,000$
K	$0.5 - 0.8$	$4,000 - 5,300$
M	$0.08 - 0.5$	$2,300 - 4,000$

[a] O-M types are spectral types associated with stellar mass objects, the spectral type classification can be extended to sub-stellar mass (types L,T and Y)

[b] Note that the specific masses and temperatures that separate spectral types are not exact. Values reported here are representative values.

Table 1.1 shows that a single spectral type covers a (non-uniform) range of masses temperatures, as such the terms "early" and "late" were introduced to further classify stars. In this scenario "early" indicates a higher mass (and temperature), for stars on the main sequence. Therefore an early G type star has a higher mass than a late type G. For evolved stars, mass and temperature are decoupled, so "early" and "late" indicate only temperature within a spectral class e.g. an early K type giant is hotter, but not necessarily more massive than a late K giant. This nomenclature has mostly been surpassed by the introduction of a numeral scale of $0 - 9$ that is

attached to the spectral type instead. For example the Sun is an early G type star also classified as G2. Further to this is a star's luminosity class denoted by a Roman numeral. This is to distinguish between main sequence and subgiants or giant stars, that share the same effective temperature. Therefore the Sun is a G2V star, the V indicating it is a main sequence "dwarf" star, whereas the star HD 106270 (that will be discussed in Chapter 2) is classified as a G5IV star, the IV indicating it is a subgiant star, and the 5 indicating it is in the middle of the G type temperature range (and cooler than the Sun).

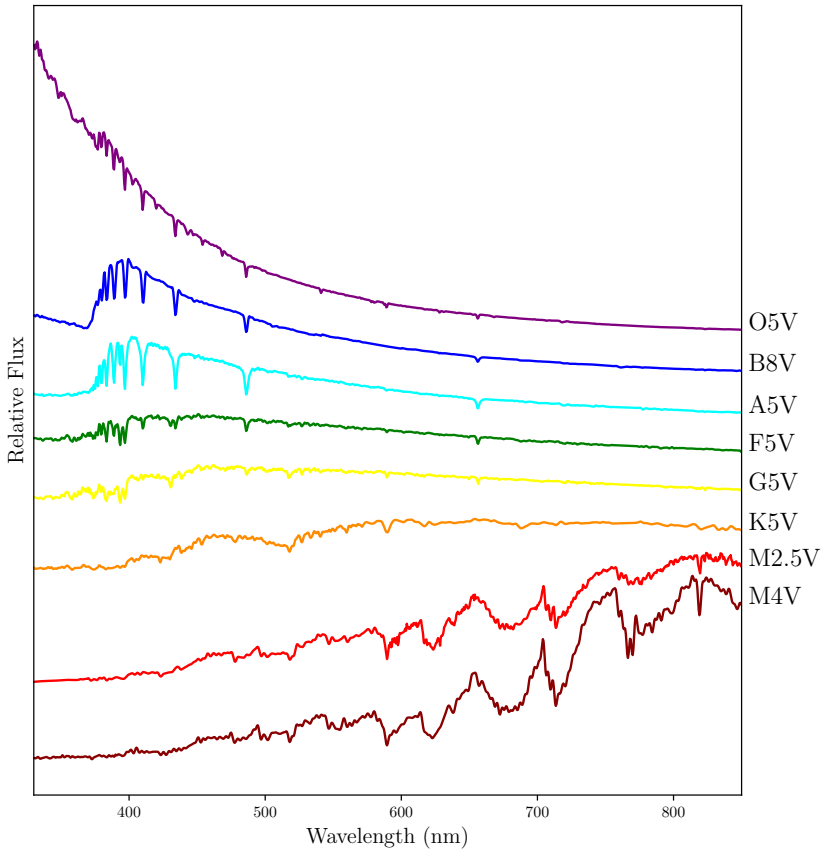

Figure 1.9: Example synthetic spectra for typical spectral types, hottest to coolest from top to bottom. The V designation indicates all these spectra are for main sequence stars. The chosen wavelength range is from near ultra-violet to near infrared. For cooler stars, the peak wavelength light is emitted at moves to longer wavelengths. The models are taken from Pickles (1998)

Figure 1.9 shows that dominant observed transitions (absorption lines) are strongly dependent on the type of star. It can also be seen that the peak wavelength of emis-

sion moves to longer wavelengths in later type/cooler stars, in line with the very good approximation that stars may be treated to first order as black-body emitters. The height/depth and shape of a spectral line are both indicative of the conditions in the stellar atmosphere.

The three stellar parameters typically considered by spectroscopy are the stellar effective temperature $T_{\rm eff}$, surface gravity $\log g$ and metallicity [Fe/H]. The metallicity of a star is the fraction of star by mass not composed of hydrogen or helium, denoted Z, such that

$$X + Y + Z = 1$$

where the X and Y are the hydrogen and helium mass fractions respectively. The iron to hydrogen abundance ratio is normally taken as a proxy for the total metal abundance of a star, and is given respective to solar values on a logarithmic scale,

$$[\mathrm{Fe/H}] = \log_{10} \frac{(\mathrm{Fe/H})_\star}{(\mathrm{Fe/H})_\odot} = \log_{10}(\mathrm{Fe/H})_\star - \log_{10}(\mathrm{Fe/H})_\odot \tag{1.14}$$

where the solar metallicity is defined to be $[\mathrm{Fe/H}]_\odot \equiv 0$. As an example this means a star with a reported metallicity of [Fe/H]$=-1$ has 1/10 the metal content of the Sun. The relation between the iron abundance and total metal abundance is normally to assume [Fe/H] $\equiv$ [M/H].

One method to extract these parameters from the spectra of a star is to fit synthetic spectra to the observed spectra, and take the best fit parameters. Figure 1.10 from Smalley (2005, Fig 2) shows what impact variations in spectroscopic parameters have on the model spectra.

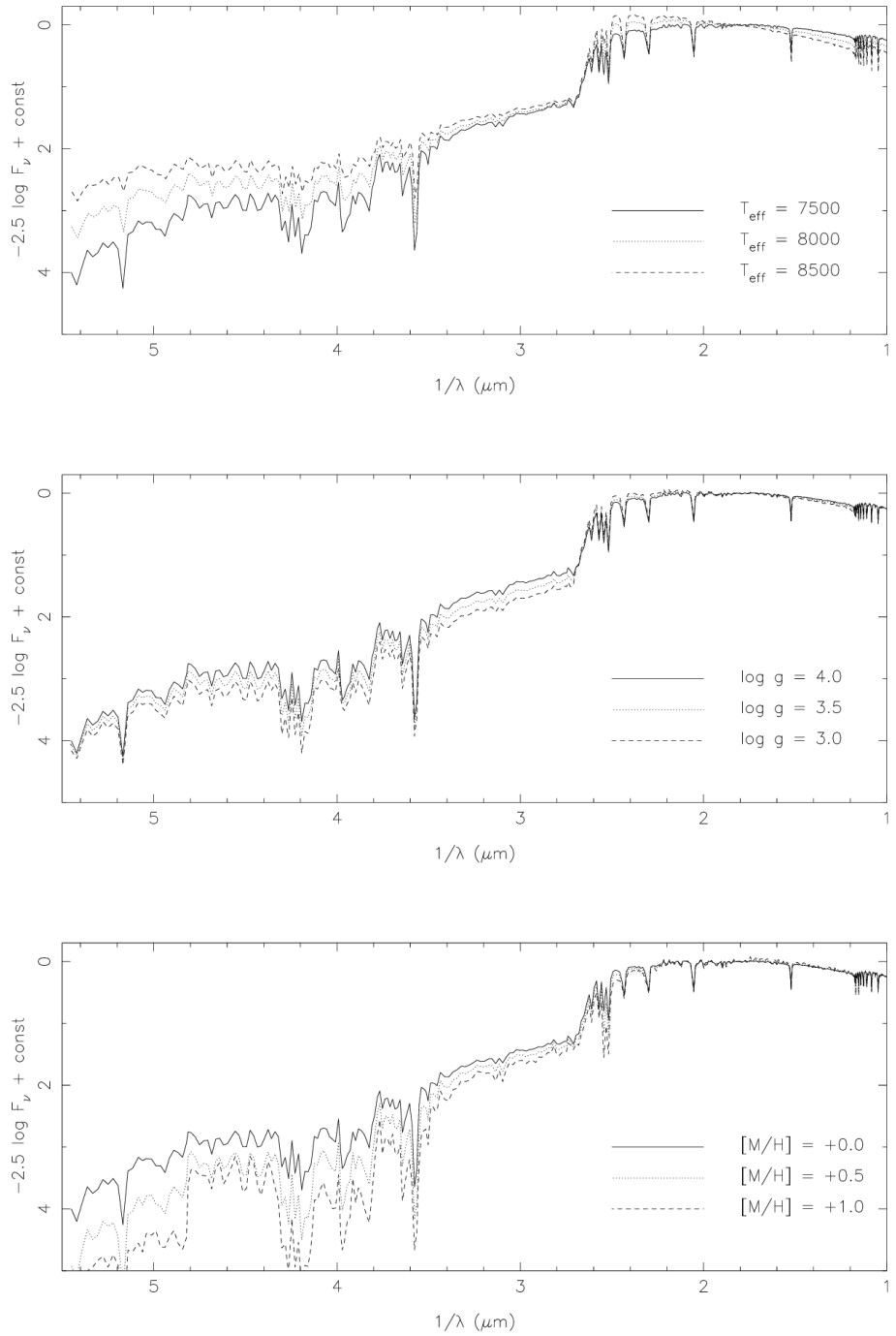

Figure 1.10: The sensitivity of a stellar spectra to variation in $T_{\rm eff}$, $\log g$ and [Fe/H] is shown here. The base model is a $T_{\rm eff}$ =7500K, $\log g$ =4.0 and [Fe/H] =0.0

Wherever spectroscopic parameters are used as inputs in analysis throughout this thesis, we have used values produced by others, using well established pipelines and techniques. Spectroscopy will primarily be used in Chapter 4. In Chapter 2 I will discuss the impact of variations in spectroscopic parameters on inferred stellar

properties.

There are several potential limitations to spectroscopy. Since spectroscopy works on matching models to data, the parameters derived are strongly model dependent, therefore the accuracy of stellar atmosphere models is paramount to the recovery of accurate stellar parameters. Stars that are rapidly rotating (such as hot main sequence stars without surface convection zones) are difficult to analyse, since the rapid rotation causes rotational broadening of observed spectral lines. This broadening can cause different spectral absorption lines to overlap or merge, making it difficult to measure the width and height accurately. Strong correlations between parameters can also be introduced in the recovery process of the stellar parameters, which can impact inferred stellar (and planetary) properties (Torres et al., 2012a).

With the stellar spectroscopic parameters recovered, these atmospheric parameters can now be used in conjunction with grids of stellar models, to recover estimates of other stellar properties. This will be covered in more detail in Sec 1.10.

1.9 Asteroseismology

Spectroscopy provides estimates of parameters that are representative of conditions in the near-surface layers of the star. What is needed is a method of probing the deep interior of the star, to understand and investigate the processes and mechanisms occurring beneath the photosphere. The answer is asteroseismology.

Asteroseismology, the study of stellar oscillations in stars other than Sun, with the related field helioseismology for the study of the Sun, has become a powerful tool in recent years.

Some of the first stellar oscillations detected were Cepheid stars. These Cepheids show a characteristic period-luminosity relationship, which has been used as part of the cosmic distance ladder to measure distances in the Universe. An excellent diagram showing stellar variability across the Hertzsprung-Russell diagram is shown in Fig 1.11. It shows there are many varieties of stellar pulsations that can be

studied. In this thesis we will only consider asteroseismology of stars termed "solar-like" oscillators. This is the region in the lower main sequence, extending up the red giant branch. For these stars, the recent CoRoT (Baglin et al., 2006), *Kepler* (Borucki et al., 2010) and *K*2 (Howell et al., 2014) missions have been instrumental in detecting solar like oscillations in thousands of stars (Bedding et al., 2010; Gilliland et al., 2010; Huber et al., 2010; Chaplin & Miglio, 2013; Huber et al., 2013b; Stello et al., 2013a; Chaplin et al., 2014; Campante et al., 2015a; Chaplin et al., 2015; Lund et al., 2016; North et al., 2017b). An important observational synergy realised during these missions was using the same data to perform complementary science. In the case of transits and asteroseismology, for a 3.5 year *Kepler* lightcurve of an individual star, once transits have been detected an exoplanet scientist might only use ∼40hours of the entire lightcurve (3 × 13hr transit for an Earth-Sun analog system) to characterise the exoplanet. Asteroseismology can use the other > 99% of the lightcurve to provide precise characterization of the star – provided the star is bright enough. This is a major synergy of exoplanet and asteroseismology fields, making use of observations that would have been made anyway without additional telescope time.

Before CoRoT and *Kepler*, solar-like oscillations had only been detected in a handful of other stars using ground-based observations (Brown et al., 1991; Kjeldsen et al., 1995; Arentoft et al., 2008).

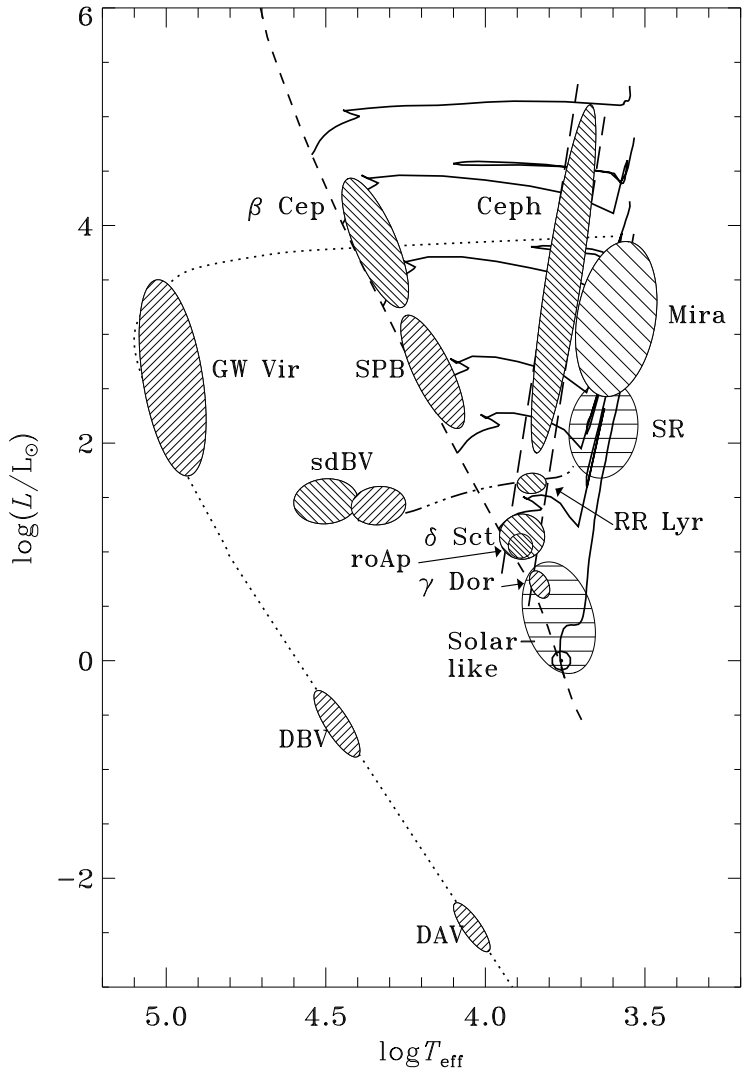

Figure 1.11: Asteroseismic Hertzsprung-Russell diagram (Christensen-Dalsgaard, 1998) showing various types of stellar pulsations that can be detected. The asteroseismology in this thesis only considers the region labelled solar-like, in the lower main sequence and red giant branch regions.

1.9.1 Generating stellar oscillations

For solar-like oscillators the outer envelope of the star is convective. It is this convection, and the turbulence associated with it in the near surface regions, that generates, and damps the stellar oscillations we detect (Chaplin & Miglio, 2013). As such, unlike Cepheid stars, the oscillations of solar-like oscillators are stochastic in nature, with relatively short lifetimes and low amplitudes. The turbulent convection

generates sound waves that propagate across the star. If an individual oscillations gives rise to a standing wave, than a global oscillation mode will be detectable. The best analogy here is with musical instruments. When guitar string is plucked, only the frequencies that set up a standing wave on the string are heard, predominantly the fundamental but also a family of overtones. The same driving force (in this case plucking) can generate tones of many frequencies by shortening the length of the string that can oscillate, meaning a single driving mechanism can produce a rich spectrum of overtones. For solar-like stars the timescale of these oscillations is of order $\sim$5 minutes, for more evolved (larger) stars the oscillations the timescale is $\sim 1-3$ hours.

An important distinction should be made here between *solar-type stars* and *solar-like oscillations*. Solar-type stars are typically main sequence stars with a similar mass, radius and temperature to the Sun, whilst solar-like oscillators are all stars where turbulent convection is driving and damping the oscillations, from the main sequence through sub and red giants to red clump stars and AGB stars.

In solar-like oscillators there are two distinct types of modes. Acoustic modes, where a pressure gradient is the restoring force, known as p modes, and oscillations where buoyancy is the restoring force which are called g modes (Bedding & Kjeldsen, 2003).

These modes probe different regions of the star. The g modes are confined to the radiative interior of solar-like oscillators, whilst p modes propagate throughout the star. However p modes are not very informative on the deep interior i.e. the core regions of the star. This is because they spend little time in this region of the star, due to higher sound speeds in the dense inner regions of the star. Additionally only radial modes will pass through the centre of the star.

Solar-like oscillations can be decomposed onto spherical harmonic functions, parameterised as the angular degree l and the azimuthal order m. In addition the radial order n is the number of nodes of the oscillation in the radial direction. As

the observations I will discuss are disk integrated over the surface of the star, due to geometrically cancellation effects only modes of low l can be observed – typically $l = 0, 1, 2$ modes.

In the Sun the dominant p mode oscillations are high overtone (high n) oscillations around $\sim$3000μHz, while the g modes are believed to exist at frequencies in the range $10 - 300\mu$Hz (Mathur et al., 2007). This means there is little interaction between solar p and g modes, due to the separation in frequency of the two oscillation cavities (the region of frequency space where the dominant oscillations exist).

As a star evolves (see Sec 1.7.1), the core contracts (raising g mode frequencies) and the envelope expands (lowering p mode frequencies). This has the effect of bringing the two oscillation cavities closer together in frequency, until the modes begin to couple. This produces additional modes called mixed modes in these evolved stars. These oscillations can have p and g like characteristics. For evolved stars these mixed modes provide diagnostic probes of the core conditions of a star, and have been used to distinguish red giant stars from red clump stars (Bedding et al., 2011), a major detection by *Kepler*, a distinction that is difficult to accomplish without asteroseismic data given the highly similar spectroscopic parameters of red giants and red clump star.

1.9.2 Characterising stellar oscillations

Fig 1.12 shows a power spectrum for KIC 6442183, a bright *Kepler* subgiant, showing the stellar oscillations. The oscillations can be seen as the series of mostly evenly spaced peaks of power around $\sim$1000μHz in black. A heavily rebinned version of the power spectrum is also shown in red. The power excess characteristic of solar-like oscillations is clearly visible above a rising background. The background below the oscillations is the signature of stellar granulation, which is the visible effect of stellar convection. Since the stellar granulation and oscillations are both driven by the turbulent convection, there are strong links between the two, and granulation

parameters (amplitudes and timescales) can be characterised using asteroseismic parameters. How the asteroseismic and granulation parameters are extracted from the power spectrum is covered in Sec 1.9.2.1.

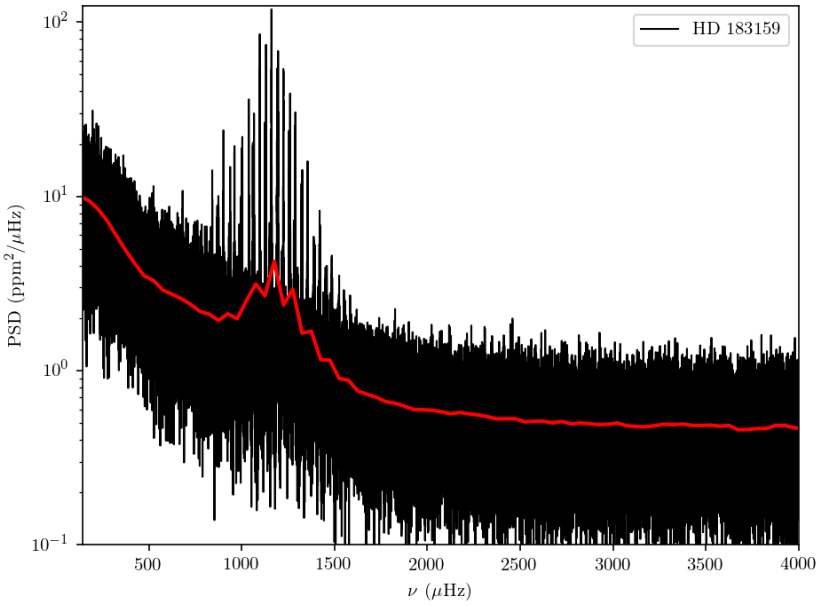

Figure 1.12: Frequency power spectrum of KIC 6442183/HD 183159, with the power spectrum in black. A heavily rebinned version of the power spectrum is shown in red, clearly showing the power excess of the oscillations above the granulation background rising at lower frequencies.

At this point we introduce the first of the "global asteroseismic parameters" that are the main asteroseismic parameters we will be considering in this thesis. Returning to Fig 1.12 the observed power of the mode peaks is modulated by an envelope that is usually taken as being a Gaussian, centered on the frequency $\nu_{\rm max}$, i.e., the frequency at which the detected oscillations show their strongest amplitudes also known as the frequency of maximum power. Its physical meaning is still debated (Belkacem et al., 2011), but it scales to very good approximation with the (isothermal) acoustic cut-off frequency in the stellar atmosphere (the frequency above which sound waves are no longer trapped), with numerous studies showing, It is possible $\nu_{\rm max}$ is therefore related to the interplay of the efficiency of generating and trapping acoustic modes, with $\nu_{\rm max}$ representing the turning point in the damping rate of

oscillations.

$$\nu_{\rm ac} \propto \nu_{\rm max} \propto \frac{c}{H}. \tag{1.15}$$

Here, the speed of sound $c \propto \sqrt{T}$, T being the mean local atmospheric temperature, and $H \propto T/g$ is the pressure scale height of the atmosphere (Brown et al., 1991; Kjeldsen & Bedding, 1995). Eq 1.15 therefore suggests the use of a relation scaled to solar values of the form

$$\frac{\nu_{\rm max}}{\nu_{\rm max,\odot}} \simeq \frac{g}{g_\odot} \left(\frac{T_{\rm eff}}{\rm T_{eff,\odot}} \right)^{-1/2}, \tag{1.16}$$

where, since oscillations are observed in the stellar photosphere, the temperature is set to $T = T_{\rm eff}$. In this work, the solar values adopted are: $g_\odot = 27400 {\rm cms}^{-2}$, $\nu_{\rm max,\odot} = 3090 \mu$Hz and $T_{\rm eff,\odot} = 5777$K (Chaplin et al., 2014). It should be noted there are potential uncertainties unaccounted for by adopting these values (e.g. uncertainty on $\nu_{\rm max,\odot}$).

The second "global asteroseismic parameter" is known as the average large frequency separation, typically also referred to as just the large frequency separation. Figure 1.13 shows zoomed in region of Fig 1.12, with the granulation background divided out.

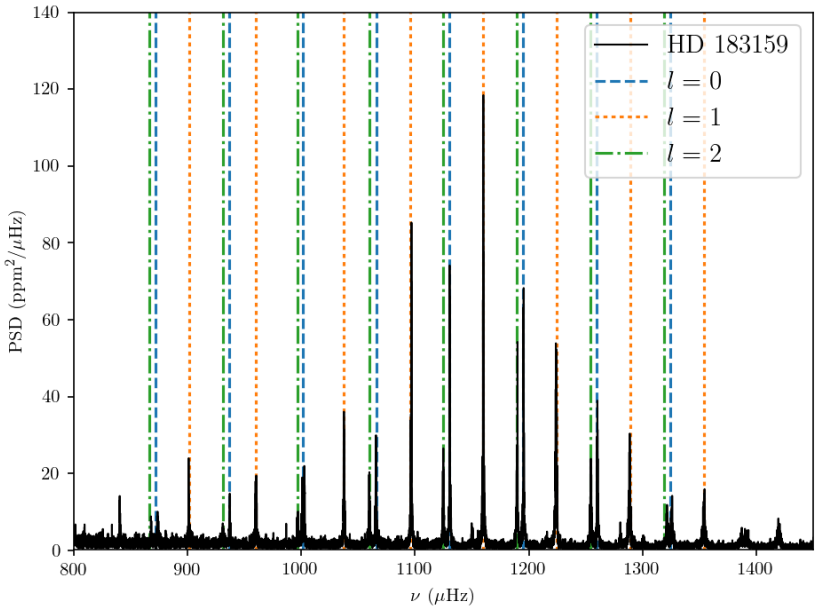

Figure 1.13: Rebinned frequency power spectrum of KIC 6442183/HD 183159, zoomed in on the region of stellar oscillations for several radial order n around $\nu_{\rm max}$, with $\nu_{\rm max} \approx 1150\mu$Hz. The granulation background has been divided out. Modes of the same degree l and subsequent radial order n are approximately evenly spaced in frequency, and are indicated with the dashed, dotted and dash-dot lines for $l = 0 - 2$. Each spacing is a large frequency separation $\Delta\nu$. The average of all $\Delta\nu$ is the average large frequency separation.

The figure shows the power spectrum for several radial orders n around $\nu_{\rm max}$. Modes of $l = 0, 1, 2$ are indicated by the coloured lines, and can be seen to be approximately equally spaced in frequency by a large frequency separation $\Delta\nu$. The average large frequency $\langle\Delta\nu\rangle$ is the mean of these individual separations.[1] In this thesis, unless otherwise specified, $\Delta\nu$ (without brackets) will refer to the average large frequency separation for a star. The average large separation, $\Delta\nu$, scales to good approximation with the square-root of mean stellar density (Tassoul, 1980; Ulrich, 1986), i.e.,

$$\frac{\Delta\nu}{\Delta\nu_\odot} \simeq \left(\frac{M}{\rm M_\odot}\right)^{0.5} \left(\frac{R}{\rm R_\odot}\right)^{-1.5} \simeq \sqrt{\frac{\rho}{\rho_\odot}}. \tag{1.17}$$

The solar reference value used is $\Delta\nu_\odot = 134.9\mu$Hz (Chaplin et al., 2014). The measurement of $\Delta\nu$ and with it the mean stellar density provides one of the first synergies with exoplanet observations, something we will return to in Sec 1.9.4.

[1]For completeness, the *small* frequency separation is the average spacing between the $l = 0$ and $l = 2$ for modes in the same order n, averaged over all orders.

Typically in this thesis when discussing asteroseismology we will be considering p or mixed mode oscillations, in an ensemble sense. We do not consider the individual oscillation frequencies and parameters, only the global asteroseismic parameters $\nu_{\rm max}$ and $\Delta\nu$.

As discussed earlier p modes are separated approximately evenly in frequency by $\Delta\nu$. Buoyancy driven, g modes, are separated approximately evenly in period, producing a final global asteroseismic parameter called the period spacing $\Delta\Pi$ (Beck et al., 2011). A difficult parameter to extract from the power spectrum, in this thesis, any place the period spacing is used, it is from a literature source. (Period spacings are only used in Chapter 3.)

With the global asteroseismic parameters and scaling relations introduced, we move on to how these parameters are recovered from data.

1.9.2.1 Extracting asteroseismic parameters

In this section we describe one approach to extracting the global asteroseismic parameters from the power spectrum of a star. There are many other methods available, including methods to recover the individual oscillation frequencies and parameters (see Huber et al. 2009; Hekker et al. 2010; Mathur et al. 2010; Handberg & Campante 2011; Verner et al. 2011). As discussed previously, the stellar oscillations, from which $\nu_{\rm max}$ and $\Delta\nu$ are extracted, are situated on top of the stellar granulation background, and that must be accounted for in any recovery process, or removed in a robust fashion. Fortunately, given the granulation-oscillation connection, this is a relatively simple process.

Harvey (1985) first formulated a model for the granulation background in the power spectrum of the Sun, as a zero-frequency-centered Lorentzian. More recent observations of the Sun, and thousands of stars observed by *Kepler*, have led to this background model being refined, with a family of "Harvey-like" or "super-Lorentzian" (where the exponent of the function does not equal 2, as in a Lorentzian) models having been invoked to explained the features of observed power spectra.

Included within this is the use of more than one granulation component. The general form is given in Eq 1.18,

$$P_{\rm gran}(\nu) = \sum \frac{\xi_i a_i^2/b_i}{1 + (\nu/b_i)^c}. \tag{1.18}$$

For *Kepler* data, Kallinger et al. (2014) explored the fitting of several models of increasing complexity, in a statistical fashion. They found that for the granulation a model with two granulation components, with super-Lorentzians of power $c = 4$, best described the data.

In Eq 1.18, $P_{\rm gran}(\nu)$ is granulation power spectral density in $\rm ppm^2 \mu Hz^{-1}$. a_i is amplitude of the granulation signal (in ppm), b_i the characteristic frequency of the super-Lorentzian. ξ_i is the normalisation constant such that a^2 is equal to the area under the super-Lorentzian (which is equivalent to the variance in the timeseries corresponding to this granulation component). With $c = 4$, $\xi_i = 2\sqrt{2}/\pi$. Both a and b can be estimated using scaling relations based upon $\nu_{\rm max}$. We will return to this in Chapter 5.

The ensemble power in the stellar oscillations is fitted as a Gaussian envelope component simultaneously with the granulation, with the central frequency of the Gaussian $\nu_{\rm max}$. To ensure robust uncertainties on parameters, the granulation and oscillation envelope are fitted using an MCMC algorithm[2].

[2]All MCMC fitting in this thesis is done in Python with the EMCEE (Foreman-Mackey et al., 2013) and CORNER (Foreman-Mackey, 2016) packages.

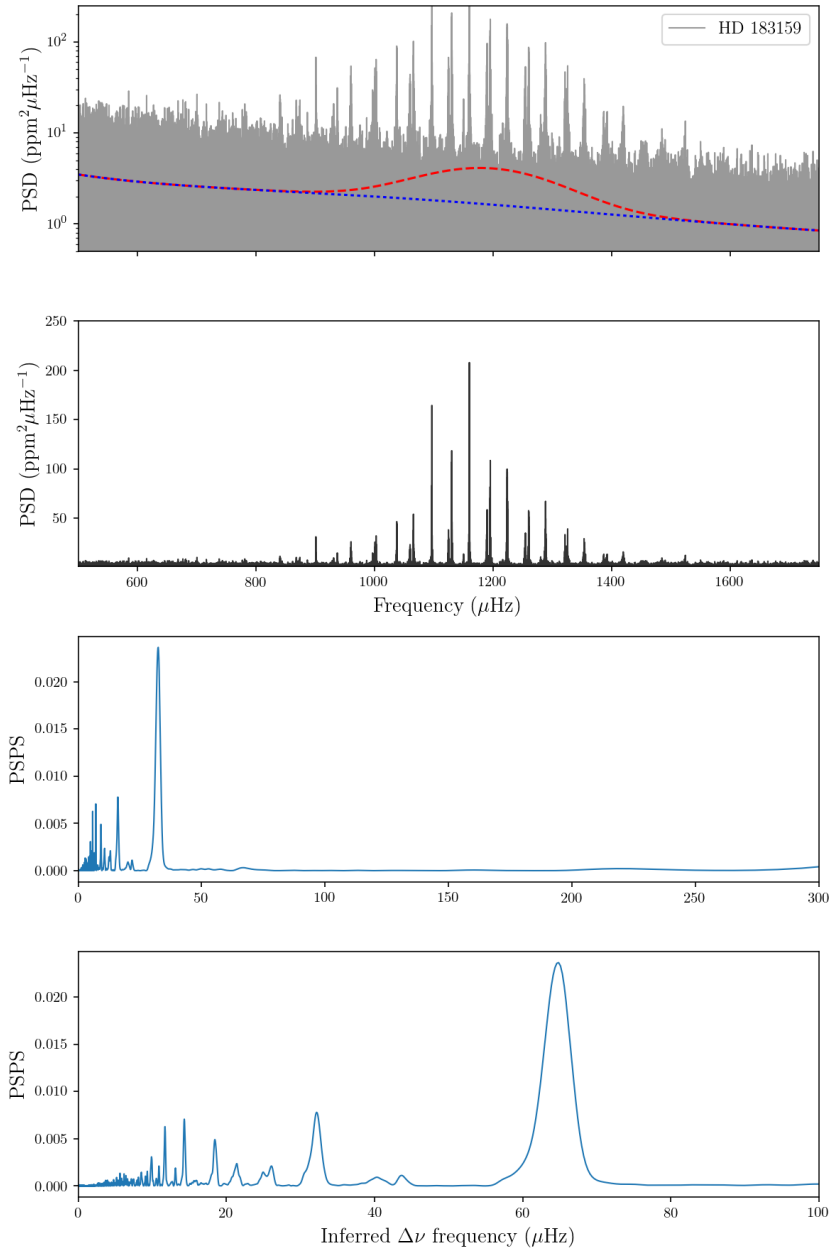

Figure 1.14: The process to extract $\Delta\nu$ from the power spectrum, the granulation background is fit simultaneously with oscillation envelope (upper panel). This is divided out to give background-corrected powerspectrum (second panel). Power spectrum of power spectrum is taken (PSPS) to identify the even spacing of modes (third panel). Strongest signal is spacing between $l_n = 0$ and $l_{n-1,n} = 1$. PSPS is rescaled by factor 2 to account for this.

The extraction of $\Delta\nu$ from the data requires an additional step to be taken, Figure 1.14 illustrates the process on KIC 6442183/HD 183159. After background (blue) and oscillation envelope (red) have been fitted to the data (black) to extract $\nu_{\rm max}$

(top panel), the background component is divided out of the data (second panel). As discussed earlier, modes of equal l, but subsequent order n are approximately equally spaced in *frequency*. If the power spectrum of the background corrected data is taken, and the resulting time axis reconverted to frequency (third panel), the frequency spacing between $l_n = 0, 1, 2$ and $l_{n\pm1} = 0, 1, 2$ across the entire power spectrum should appear as a single peak. A complication to this concept is that since $l_n = 1$ modes are located halfway between $l_n = 0$ and $l_{n\pm1} = 0$, the strongest periodicity that appears in the power spectrum of the power spectrum (PSPS) is the spacing between $l = 0$ and $l = 1$ modes which is equal to $\Delta\nu/2$. To account for this the frequency axis of the PSPS is rescaled by a factor of 2 so the largest peak corresponds to the average large frequency separation $\Delta\nu$.

With the extraction of the global asteroseismic parameters discussed, I briefly discuss further inferences that can be made from them, including mass and radius estimates.

1.9.3 Asteroseismic Mass and Radius scaling relations

If Eq 1.16 and Eq 1.17 are combined, with the additional input of an effective temperature measurement, model independent estimates for the stellar mass and radius can be provided by,

$$\frac{M}{\mathrm{M}_\odot} = \left(\frac{\nu_{\mathrm{max}}}{\nu_{\mathrm{max},\odot}}\right)^3 \left(\frac{\Delta\nu}{\Delta\nu_\odot}\right)^{-4} \left(\frac{T_{\mathrm{eff}}}{\mathrm{T}_{\mathrm{eff},\odot}}\right)^{1.5}, \tag{1.19}$$

and

$$\frac{R}{\mathrm{R}_\odot} = \left(\frac{\nu_{\mathrm{max}}}{\nu_{\mathrm{max},\odot}}\right) \left(\frac{\Delta\nu}{\Delta\nu_\odot}\right)^{-2} \left(\frac{T_{\mathrm{eff}}}{\mathrm{T}_{\mathrm{eff},\odot}}\right)^{0.5}. \tag{1.20}$$

These relations have been shown to be good to around $\approx 5\%$ in radius (Huber et al., 2012) and $\approx 10\%$ in mass (Miglio et al., 2012; Chaplin & Miglio, 2013; Guggenberger et al., 2016). The scaling relations have been tested using stellar derived from interferometry, and through comparisons of dynamical masses in non-

interacting eclipsing binary systems, where at least one component displays solar-like oscillations. Various corrections have been suggested to these relations to improve the accuracy of these relations (see Viani et al. 2017 and references therein), however these simple relations are a reasonable first estimate of the stellar properties, before more detailed modelling is undertaken (see Sec 1.10). They are useful where only a "reasonable" estimate of the stellar mass or radius are needed, or where it would be computationally expensive to perform modelling (such as for thousands of stars). In this thesis stellar masses and radii provided will be recovered from models, rather than these scaling relations. As can be seen in the above equations, a stellar effective temperature is still required to construct the mass or radius, thus the calculated values are sensitive to the adopted temperature scale (Huber et al., 2012).

With the key asteroseismic relations introduced, we will now discuss a final benefit that asteroseismology can provide to transiting exoplanet system characterisation.

1.9.4 Orbital eccentricity and stellar density

As discussed in Sec 1.5.1, the mean stellar density can be estimated from transit photometry alone (Seager & Mallén-Ornelas, 2003; Winn, 2010):

$$\rho_\star + k^3\rho_p = \frac{3\pi}{GP^2}\left(\frac{a}{R_\star}\right)^3. \qquad \text{(1.7 repeat.)}$$

In Eq 1.7, the stellar density $\rho_\star$ can be recovered using the observed period P, and the reduced semi-major axis of the orbit $a/R_\star$ (see Sec 1.5.1). For circular orbits, the above equation will directly give constraint on the stellar density. However for eccentric orbits, the observed $a/R_\star$ will be influenced by the orbital eccentricity e and observed orientation of the orbit-due to the influence of these parameters on the transit duration (see Fig 1.7).

As discussed in Sec 1.9.2 asteroseismology can also provide an independent stellar density directly through the $\Delta\nu$ scaling relation in Eq 1.17, or from the final parameters of detailed modelling (that will be discussed in the following section).

This stellar density can be compared to that inferred from the lightcurve to provide constraint on the planetary eccentricity, without the need for radial velocity observations (Van Eylen & Albrecht, 2015), and will be used in Chapter 3.

1.10 Recovering Stellar Properties from Models

At this point, all the major planetary and stellar observables have been introduced. Now how can we use them to infer stellar properties that are not directly observable? There are two methods available. The first is to use scaling relations between different stellar properties as estimates of the unknown from the known-also known as the direct method. The asteroseismic mass and radius relations discussed above in Sec 1.9.3 are an example of this, using asteroseismic observables (and an effective temperature) to produce model independent estimates. A non-asteroseismic example would be the mass-luminosity scaling relation observed on the main-sequence $L \approx M^{\alpha}$ where $\alpha \sim 3-4$. While these relations are useful for quick calculations and rough estimates, to achieve high precision measurement, it is better to use the second method of estimating stellar properties.

Detailed grids of stellar models can be produced that cover a star's entire lifetime, into which a subset, or all available observables can be fed. A stellar model is typically generating by using a stellar evolutionary code to model the time evolution of a star in regular steps in time. Each added level of complexity in the physics used inside the model should increase the accuracy of the produced model, but also increases the time to compute. A stellar model will contain both the stellar properties of the star at that point in time (mass, radius etc) but also the associated theoretical observables ($T_{\rm eff}$, $\log g$, [Fe/H], $\nu_{\rm max}$ etc). The next step is to either find the best fit model (of observed parameters to model parameters) and return the associated stellar properties for that model, or to find the best fit models and interpolate between them to recover the best fit values. The parameters typically used are the stellar effective temperature, luminosity (or parallax), surface gravity,

and metallicity. The apparent magnitude of the star in many passbands can also be an input. With the recent advances in asteroseismology, some stellar models are now using these inputs directly also. As discussed in Sec 1.9.2, the theoretical underpinning of $\nu_{\rm max}$ is still missing and so in stellar model, $\nu_{\rm max}$ is calculated according to Eq 1.16. How $\Delta\nu$ is calculated is according to the stellar models used, some use scaling relation given in Eq 1.17, whilst others use a model $\Delta\nu$ calculated from theoretical frequencies. The stellar models used in this thesis use model $\Delta\nu$ values calculated from theoretical frequencies produced alongside the rest of the stellar model (see Chap 2 for more detail).

It should be made clear that the models being discussed here are different to the stellar atmosphere models discussed in Sec 1.8.2. Stellar atmosphere models are used to recover spectroscopic parameters from the spectral observations. The resulting parameters from this are then used in conjunction with stellar evolution models to recover the stellar properties of the star.

The recovered stellar properties are naturally model dependent, and also sensitive to the constraints used during the fitting process (see Chapter 2). As such, the accuracy of the stellar models is paramount, including how complete the physics used inside the model is. Unfortunately, modelling the entire life of a star is an intrinsically difficult problem, with many competing physical processes needing accounting for. Therefore a certain level of parameterisation, approximations and assumptions are made. One such parameter is convective overshooting. In a solar-like star, whilst the convection zone of a star nominally stops at the boundary with the radiative zone, material will arrive at this "hard" boundary with a non-zero momentum. This momentum will allow convection to penetrate the radiative zone to some small degree. As we will see in Chapter 2, changing the amount of convective overshoot can significantly change the recovered stellar properties. This is just one example of where the physics underpinning stellar models is incomplete

The sensitivity of the the recovered mass is illustrated in Figure 1.15 (Campante

et al., 2017, Figure 2). Stellar model tracks (green) with the 1σ with observational constraints, in this case $\nu_{\rm max}$, $\Delta\nu$, L, $T_{\rm eff}$ and $\log g$ were available and are indicated. The yellow region in the area of intersection between the different constraints is the 68% credible intervals in mass and radius for the star, using these constraints. It can be seen that the spectroscopic and luminosity constraints find a broader region of parameter space in which to isolate the true mass than when asteroseismic constraints are also included. In this figure can also be seen the impact of poor or inaccurate constraints. Both the *Hipparcos* and *Gaia* luminosity 1σ regions are indicated (black horizontal dashed and grey horizontal line respectively). If the *Hipparcos* luminosity is to be used, in order to resolve the discrepancy between the asteroseismic and luminosity constraints, a higher mass is recovered from the models.

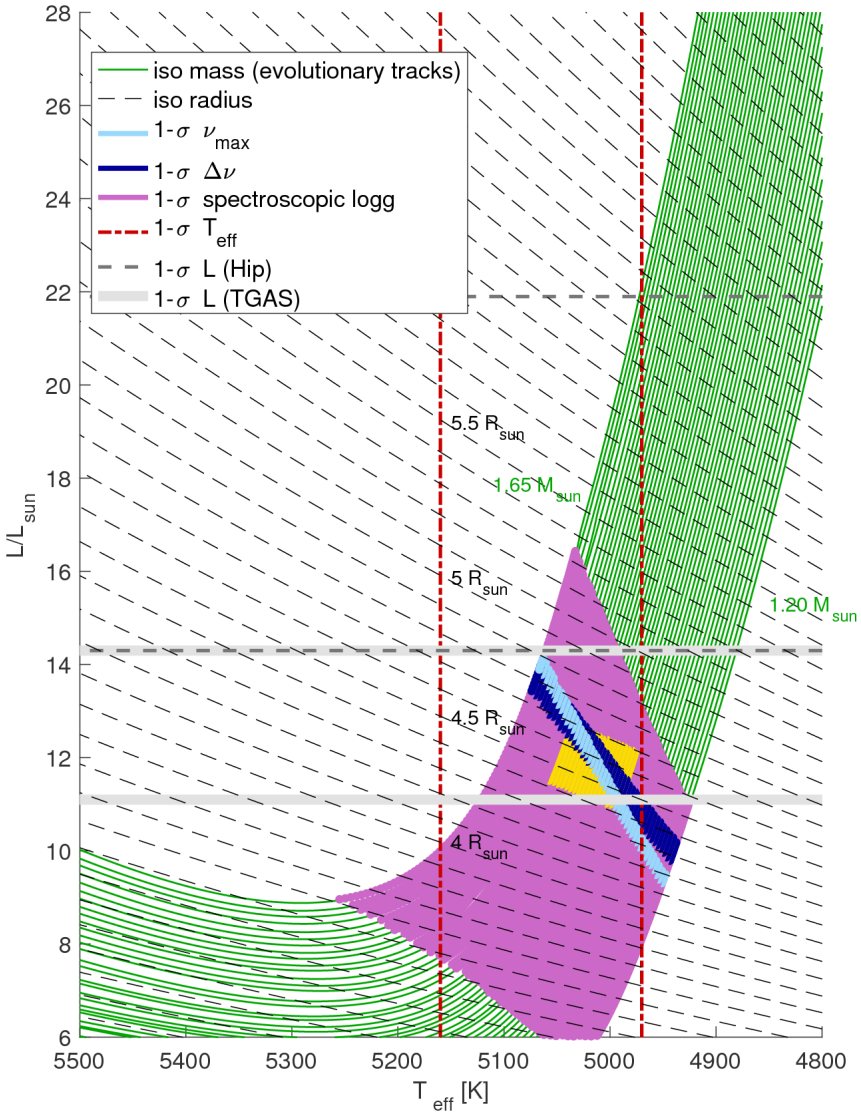

Figure 1.15: Hertzsprung-Russell diagram showing observational constraints used in the estimation of fundamental stellar properties for HD 212771. Evolutionary tracks spanning the mass range 1.20-1.65$M_{\odot}$ (in steps of 0.01 $M_{\odot}$) were computed at [Fe/H] =-0.1 (green lines). Contours of constant radius are diagonal dashed lines. Coloured bands represent the 1σ observational constraints on $\Delta\nu$, $\nu_{\rm max}$ and $\log g$. 1σ bounds on $T_{\rm eff}$ and L are also shown (vertical and horizontal lines respectively). L constraints for both *Hipparcos* and *Gaia* based L are shown. The yellow-shaded box represents the 68% Bayesian credible region for stellar mass and radius corresponding to the solution (see Table 2.2)

In this thesis, the inference of stellar properties from observable parameters and grids of stellar models was performed using the Bayesian code PARAM (da Silva et al., 2006; Rodrigues et al., 2017). Stellar observables and stellar models, in this thesis primarily MESA (Modules for Experiments in Stellar Astrophysics) models (Paxton et al., 2011, 2013). The available observables and their uncertainties ($T_{\rm eff}$,

$\nu_{\rm max}$, $\Delta\nu$, [Fe/H] etc) are used as inputs into PARAM. PARAM then derives a probability density function (PDF) for the stellar properties, by assessing the likelyhood of the provided observables within the grid of models. A benefit of PARAM is that the available contraints can be changed, depending on which are available i.e. the stellar models can be explored with or without the use of seismic parameters. The added benefit of using a Bayesian methodology is that prior information or knowledge can be included when exploring the stellar models, such as a prior on the stellar age that states the recovered stellar properties cannot correspond to a star older than the age of the Universe. A full discussion of Bayesian stellar modelling is beyond the scope of this thesis, readers are encouraged to read da Silva et al. (2006) and Rodrigues et al. (2017) for full details on PARAM.

2 Retired A Stars

The majority of the text in this chapter is taken from North et al. (2017b). I was first author on this journal article. In terms of the individual work performed, I did the majority of the work, with the exception of coding PARAM *and producing the grids of stellar models- see Sec 2.5.*

2.1 Introduction

Long term radial velocity surveys have discovered a population of giant planets on $\geq$300 day orbits around evolved stars that are more massive than the Sun (Johnson et al., 2007a; Bowler et al., 2010; Wittenmyer et al., 2011). These host stars would have been spectral type A on the main sequence. Evolved stars were targeted since A-type stars are hostile to radial velocity observations on the main sequence, due to rapid rotation broadening spectral lines (Johnson et al., 2007a). These stars show a population of planets distinct from the planets discovered via transit surveys, particularly the vast numbers of planets discovered by the NASA *Kepler* and K2 missions (Johnson et al., 2010b; Borucki et al., 2010; Fressin et al., 2013; Howell et al., 2014). It remains unclear if the different populations observed are a single population observed with strong selection effects, or if the different populations of planets truly indicate separate planet formation mechanisms (Fischer & Valenti, 2005; Howard et al., 2010; Becker et al., 2015).

Recently the masses of evolved stars have been brought into question on several grounds (Lloyd, 2011; Schlaufman & Winn, 2013), with the possibility raised that the masses of evolved hosts have been overestimated when derived from spectroscopic

observations. The mass of these stars is typically recovered by interpolating grids of stellar models to the observed $T_{\rm eff}$, $\log g$, and [Fe/H], and including additional parameters such as luminosity and colours where available (see Johnson et al. 2007a and references therein). These stellar models are then explored in a probabilistic fashion to find the best solution for the fundamental stellar properties (da Silva et al., 2006; Ghezzi & Johnson, 2015).

These evolved stars have been termed "retired A stars" in current literature (Johnson et al., 2008; Bowler et al., 2010; Lloyd, 2011), since the derived masses for these stars is typically $M \gtrsim 1.6 \mathrm{M}_{\odot}$ i.e around the boundary in stellar mass between A and F type stars on the main sequence. We follow that convention in this work, but note that the term "retired A stars" can extend to the stellar mass range more typically associated with hot F type stars on the main sequence ($\sim 1.3 - 1.6 \mathrm{M}_{\odot}$).

To try and resolve the above issues another analysis method to determine the masses of evolved stars is needed. The high quality data from the *Kepler* and K2 missions provide an opportunity to perform asteroseismology (Gilliland et al., 2010; Chaplin et al., 2015) on known evolved exoplanet hosts (Campante et al., 2017). In this paper we investigate 7 stars that have been labelled "retired A stars" in the literature, and use a homogeneous asteroseismic analysis method to provide accurate and precise masses. For the ensemble, we investigate the fundamental stellar properties estimated from differing combinations of spectroscopic and asteroseismic parameters. The stellar masses are estimated by fitting grids of stellar models to the observable constraints. With these masses we address any potential systematic bias in the masses of evolved hosts, when the masses are derived from purely spectroscopic parameters. We also investigate potential biases due to the choice of the stellar models used.

The format of the paper is as follows. Sec 2.2 describes how the targets were selected and vetted. Sec 2.3 discusses how the lightcurves were processed to allow the solar-like oscillations to be detected and how the asteroseismic parameters were

extracted from the observations, whilst Sec 2.4 details any previous mass results for each star in turn, and any subtleties required during the extraction of the asteroseismic parameters. The modelling of the stars to estimate the fundamental stellar properties is discussed in Sec 2.5. The final results are in Sec 2.6. In Sec 2.7 we explore in detail potential sources of biases in recovering the fundamental parameters, along with a detailed discussion of potential biases induced in stellar modelling due to differences in constraints and underlying physics.

2.2 Target Selection

Targets were selected from cross-referencing the K2 Ecliptic Plane Input Catalog (EPIC) (Huber et al., 2016) and the NASA Exoplanet Archive (Akeson et al., 2013a), where only confirmed planets discovered by radial velocity were retained. The resulting list was then cross-checked with the K2FOV tool (Mullally et al., 2016) to ensure the stars were observed during the K2 mission. To ensure these hosts were all selected from the correct area of parameter space, it was also checked that they all passed the target selection of Johnson et al. (2006) of, $0.5 < M_V < 3.5$, $0.55 < B - V < 1.0$ [1]. This produces 6 stars in Campaigns 1-10 (C1-10).

The lightcurve for the star identified in C1 was found to be of too low quality to observe stellar oscillations. An additional target was found in C2, through checking targets in K2 guest observer programs[2] of bright evolved stars that have been subject to long term radial velocity observations (Wittenmyer et al., 2011). This star was not identified in the initial selection as it is not a host star but it passes the color and absolute magnitude selection of Johnson et al. (2006).

HD 212771 was also subject to asteroseismic analysis in Campante et al. (2017), using the same methods presented in Sec 2.5.

[1]The selection function also contains an apparent magnitude cut of $V \leq 7.6$. We ignore this cut, as this was imposed originally to limit the required exposure time for the stellar spectra and does not influence the fundamental properties of the stars themselves.

[2]Targets found using GO programs and targets listed here, https://keplerscience.arc.nasa.gov/k2-approved-programs.html

Table 2.1: The 7 stars to be investigated in the paper, all have been observed by either the *Kepler* or K2 missions, and subject to long term radial velocity observations. The Obs column indicates what observing campaign of K2 the star was observed in (C2-10), or if it was observed in the *Kepler* mission (KIC). The GO column indicates which K2 guest observer program(s) the star was part of.

EPIC/KIC	HD	Obs	Mag (V)	RA (h:m:s)	Dec (d:m:s)	GO
203514293	145428	C2*	7.75	16:11:51.250	-25:53:00.86	2025, 2071, 2109
220548055	4313	C8	7.82	00 45 40.359	+07 50 42.07	8031, 8036, 8040, 8063
215745876	181342	C7	7.55	19:21:04.233	-23:37:10.45	7041, 7075, 7084
220222356	5319	C8*	8.05	00:55:01.400	+00:47:22.40	8002, 8036, 8040
8566020	185351	KIC*	5.169	19:36:37.975	+44:41:41.77	N/A
205924248	212771	C3*	7.60	22:27:03.071	-17:15:49.16	3025, 3095, 3110
228737206	106270	C10*	7.58	12 13 37.285	-09 30 48.17	10002, 10031, 10040, 10051, 10077

*Observed in short cadence mode

In addition the retired A star HD 185351, observed during the nominal *Kepler* mission, has been added to the sample. This star has already been subject to asteroseismic analysis in Johnson et al. (2014). However it has been added to this sample for reanalysis for completeness.

The 7 stars in our ensemble are summarised in Table 2.1, including which guest observer program(s) the stars were part of. Before we discuss the previous mass estimates for each star in Sec 2.4, we discuss the data collection and preparation required to extract the asteroseismic parameters from the K2 data.

2.3 Observations and data preparation

All targets have been subject to long term radial velocity programs attempting to detect the periodic stellar radial velocity shifts induced by orbiting planets. However for the purposes of asteroseismology high quality, uninterrupted photometry is required. This was achieved during the *Kepler* and K2 missions.

The lightcurves for the K2 targets were produced from the target pixel files using the K2P^2 pipeline, (Lund et al., 2015), and then subsequently corrected using the KASOC filter (Handberg & Lund, 2014a). Table 2.1 indicates if the stars were observed at a cadence of $\sim$1 minute (short cadence) or $\sim$30 minutes (long cadence).

The evolved stars in this paper are expected to exhibit solar-like oscillations, with near surface convection driving global oscillation modes (p and g modes) inside the star. Such oscillations have been observed in thousands of red giants by the *Kepler* and K2 missions (Huber et al., 2010; Hekker et al., 2011a; Stello et al., 2013a, 2015). Fig 2.1 shows all the power spectra produced from the corrected lightcurves for the ensemble. In all targets there are clear signatures of solar-like oscillations, above the granulation background.

Here, we make use of the so-called "global" asteroseismic parameters; $\nu_{\rm max}$, the frequency of maximum power and $\Delta\nu$, the average large frequency separation, defined as the average frequency spacing between acoustic oscillation modes of the same angular degree l and consecutive radial order n. Table 2.1 is ordered by increasing $\nu_{\rm max}$, as are Tables 2.2 and 2.4.

These seismic parameters were extracted from each power spectrum using a variety of well established, and thoroughly tested automated methods (Huber et al., 2009; Verner et al., 2011; Lund et al., 2016; Davies & Miglio, 2016). The values used in subsequent analysis are those returned by the method described in Huber et al. (2009). Since multiple pipelines were used to extract the parameters, the uncertainties used in the modelling are the formal errors returned by the Huber et al. (2009) pipeline with the standard deviation of the errors returned from the other methods added in quadrature. This additional uncertainty should account for any unknown systematics in each of the recovery methods. When compared to the seismic values returned by the Huber et al. (2009) pipeline, none of the methods differ by more than 1.3σ in $\Delta\nu$, and less than 1σ in $\nu_{\rm max}$. Line-of-sight velocity effects are negligible and do not affect the seismic results (Davies et al., 2014).

An additional asteroseismic parameter, where available, is the average g-mode period spacing, accessed through $l = 1$ "mixed" modes (Beck et al., 2011; Mosser et al., 2011). Mixed modes can be highly informative in constraining stellar models, and the core conditions of evolved stars (Bedding et al., 2011; Lagarde et al., 2016).

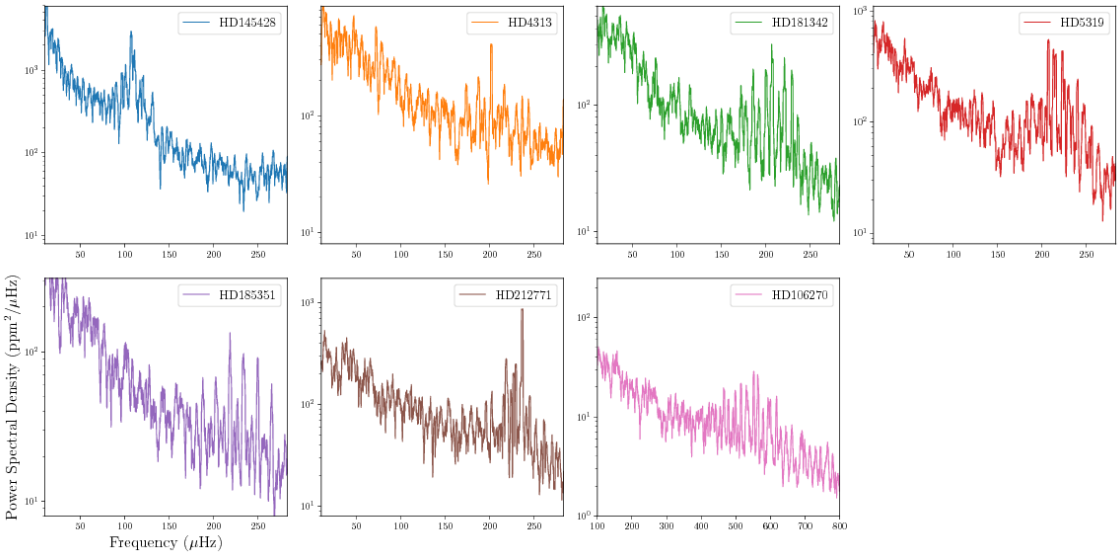

Figure 2.1: The power spectra for each star in our sample, smoothed by a 2μHz uniform filter (4μHz in case of HD 106270), from which we extract the asteroseismic parameters. The stellar oscillations are clearly visible above the granulation background. Note the change in scale for the Campaign 10 star, HD 106270. The stars are presented in order of increasing $\nu_{\rm max}$.

Unfortunately due to the shorter length of K2 datasets and hence limited frequency resolution, the period spacing is inaccessible for the 6 K2 targets in our ensemble.

2.4 Star-by-Star vetting

In this section we discuss any individual peculiarities of each star separately. Particular focus is placed on HD 185351, which has been subjected to a suite of investigations throughout and after the nominal *Kepler* mission (Johnson et al., 2014; Ghezzi et al., 2015; Hjørringgaard et al., 2016). All available literature masses for the stars in our ensemble are summarised in Table 2.5 in the appendix. The final seismic and spectroscopic values used in the stellar modelling are summarised in Table 2.2.

2.4.1 HD 145428

The most evolved star in our sample, HD 145428, it is not currently known to host planets, but was a target of the Pan-Pacific Planet Search (PPPS Wittenmyer et al. 2011) conducted on the Southern sky from the 3.9m Anglo-Australian Telescope. Here we use updated spectroscopic parameters from Wittenmyer et al. 2016. The

target selection for the PPPS is very similar to the target selection used in the Lick & Keck Doppler survey (Johnson et al., 2006, 2007a,b). This star passes the absolute magnitude selection criteria of Johnson et al. (2006), however $B-V=1.02$ for this star, slightly over the $B-V \leq 1$ selection cut. It was decided to retain this star in the sample despite this, since it is close to the boundary. Additionally the PPPS survey was also designed to search for star around "retired A stars", and so retaining this star is justified. Whilst most of the stars in our sample have multiple mass values quoted in the literature, this star appears to have been subject to minimal study, limiting the scope of comparison between asteroseismic and spectroscopic mass estimates.

2.4.2 HD 4313

HD 4313, an exoplanet host announced in Johnson et al. (2010b), shows evidence for suppressed $l=1$ modes, first identified as a feature in red giant power-spectra in Mosser et al. (2012a). The cause for such suppression is currently under discussion (see Fuller et al. 2015; Stello et al. 2016; Mosser et al. 2016), though in this case we assume that it is not a planet-based interaction, since the planet HD 4313b has an orbital period of approximately 1 year. The limited number of observable oscillation modes also has an impact on the precision of the seismic values, as reflected in the uncertainty on $\nu_{\rm max}$ in Table 2.2.

2.4.3 HD 181342

HD 181342, an exoplanet host reported in Johnson et al. (2010a), has the largest spread in reported masses, with estimates from $1.20-1.89\mathrm{M}_{\odot}$ (Huber et al., 2016; Jones et al., 2016).

2.4.4 HD 5319

HD 5319, is the only known multiple planet system in our sample. Both discovery papers list stellar masses in excess of $M>1.5\mathrm{M}_{\odot}$ (Robinson et al., 2007; Giguere

et al., 2015).

2.4.5 HD 185351

HD 185351 (KIC 8566020), one of the brightest stars in the *Kepler* field, has been monitored as part of a Doppler velocity survey to detect exoplanets (Johnson et al., 2006), though no planet has been found. Additionally in Johnson et al. (2014) (hereafter J14) the star was studied using asteroseismology, comparing the stellar properties determined from various complementary methods, including an interferometric determination of the stellar radius. Several mass values are given, in the range $1.6 - 1.99\mathrm{M}_{\odot}$. As mentioned above, the observed period spacing between mixed modes can be an important constraint on core properties and so global stellar properties. In J14, a period spacing $\Delta\Pi = 104.7 \pm 0.2$s is given. Since we wish to perform a homogeneous analysis for the ensemble, we do not include a period spacing for the star during the recovery of the stellar properties in Sec 2.5.

2.4.6 HD 212771

This is an exoplanet host detected in Johnson et al. (2010a). The mass reported in the discovery paper, $M = 1.15\mathrm{M}_{\odot}$, is consistent with a retired F or G type star. However, the recent work by Campante et al. (2017) provides an asteroseismic mass of $M = 1.45\mathrm{M}_{\odot}$, promoting this star to being a retired A star. This mass was recovered using the same methodology as used in this work (see Section 2.5). We present an updated mass in this work, though the shift is negligible.

2.4.7 HD 106270

The final star in our ensemble, this exoplanet host reported in Johnson et al. (2011) is significantly less evolved than the rest of the ensemble.

2.5 Modelling

2.5.1 Stellar Models

With the asteroseismic parameters determined for each star, the modelling of the ensemble to extract fundamental stellar properties could now take place. We use MESA models (Paxton et al., 2011, 2013) in conjunction with the Bayesian code PARAM (da Silva et al., 2006; Rodrigues et al., 2017). A summary of our selected "benchmark" options is as follows;

- Heavy element partitioning from Grevesse & Noels (1993).
- OPAL equation of state (Rogers & Nayfonov, 2002) along with OPAL opacities (Iglesias & Rogers, 1996), with complementary values at low temperatures from Ferguson et al. (2005).
- Nuclear reaction rates from NACRE (Angulo et al., 1999).
- The atmosphere model is taken according to Krishna Swamy (1966).
- The mixing length theory was used to describe convection (a solar-calibrated parameter $\alpha_{\rm MLT} = 1.9657$ was adopted).
- Convective overshooting on the main sequence is set to $\alpha_{\rm ov} = 0.2H_p$, with H_p the pressure scale height at the border of the convective core (more on this in Sec 2.7.2). Overshooting was applied according to the Maeder (1975) step function scheme.
- No rotational mixing or diffusion is included.
- When using asteroseismic constraints, the large frequency separation $\Delta\nu$ within the MESA model is calculated from theoretical radial mode frequencies, rather than based on asteroseismic scaling relations.

Below we discuss the additional inputs required for the modelling, such as $T_{\rm eff}$, [Fe/H] and luminosity.

In Sec 2.7.2 we test the robustness of the asteroseismic masses by varying the underlying model physics, and explore the effects of unaccounted for biases in the stellar observations.

2.5.2 Additional modelling inputs

In addition to the asteroseismic parameters, a temperature and metallicity value are needed for each star. Since multiple literature values exist for the chosen targets, we had to choose a source for each. To ensure the values are self-consistent, when a literature value was chosen for temperature, we took the stellar metallicity from the same source i.e. matched pairs of temperature and metallicity. To account for unknown systematics additional uncertainties of 59K and 0.062 dex were added in quadrature to the effective temperature and metallicity respectively, as recommeneded in Torres et al. (2012b), to the chosen literature values. Several of the stars have smaller reported [FeH] error bars than the systematic correction of Torres et al. (2012b), for these stars an error bar of 0.1dex was adopted.

The stellar luminosity also provides a strong constraint on the modelling. The luminosity may be estimated as follows (e.g. see Pijpers 2003):

$$\log_{10}\frac{L}{L_\odot} = 4.0 + 0.4M_{\rm bol,\odot} - 2.0\log_{10}\pi[\rm mas] - 0.4(V - A_V + BC(V)). \quad (2.1)$$

Johnson V magnitudes and uncertainties were taken from the EPIC catalog (Huber et al., 2016), the solar bolometric magnitude $M_{\rm bol,\odot} = 4.73$ is taken from Torres (2010), from which we also take the polynomial expression for the bolometric correction[3] $BC(V)$. Finally, the extinction A_V is calculated using MWDUST (Bovy et al., 2016)[4], using the 3D dust maps from Green et al. (2015).

[3]The polynomial bolometric corrections presented in Torres (2010), are reprints of values presented in Flower (1996), having been corrected for typographical errors in the original

[4]github.com/jobovy/mwdust

2.5.3 Parallaxes

Parallaxes π were taken from *Hipparcos* (van Leeuwen, 2007), and the recent Tycho-Gaia Astrometric Solution (TGAS) data release, part of the *Gaia* Data Release 1 (Lindegren et al., 2016). The *Gaia* parallax is generally preferred, due to the higher precision. HD 185351 and HD 106270 are both missing *Gaia* TGAS parallaxes due to their bright apparent magnitudes, with *Gaia* DR1 missing many stars with *Gaia* magnitude $G \leq 7$. For stars with a TGAS parallax an additional uncertainty of 0.3mas has been added to the formal parallax uncertainty as suggested by Lindegren et al. (2016), to account for any unknown systematic in the DR1 parallax. Campante et al. (2017) previously found that the *Hipparcos* solution for the distance to HD 212771 is in tension with the asteroseismic solution, whilst the *Gaia* solution is entirely consistent.

Conversely, the luminosity constructed using Eq 2.1 for HD 145428 was severely discrepant due to the large difference between the *Gaia* and *Hipparcos* parallaxes (5.39 ± 0.73mas and 7.62 ± 0.81mas respectively). When the final stellar radius from the modelling is used along with the input temperature, the constructed luminosity is found to be consistent with the *Hipparcos* luminosity, but not the *Gaia* luminosity. As such the *Gaia* luminosity was also ignored in this case, and all modelling results for this star are reported using a *Hipparcos* parallax based luminosity. There has been discussion in the literature of possible offsets in the *Gaia* parallaxes when compared to distances derived from eclipsing binaries (Stassun & Torres, 2016) and asteroseismology (De Ridder et al., 2016; Davies et al., 2017; Huber et al., 2017).

2.6 Results

Table 2.2 summarises the asteroseismic and spectroscopic inputs used in the analysis, and the estimated stellar properties returned by PARAM for our benchmark set of chosen input physics. Additional modelling using different constraints and model grids is discussed in Sec 2.7.

Table 2.2: The final asteroseismic and spectroscopic inputs and output stellar parameters from the modelling. The effective temperature and metallicity used for each source are taken as matched pairs from the same source.

EPIC/KIC	HD	$\Delta\nu$ (μHz)	$\nu_{\rm max}$ (μHz)	$T_{\rm eff}$ (K)	[Fe/H]	Mass ($M_\odot$)	Radius ($R_\odot$)	Age (Gyr)
203514293*	145428	10.1 ± 0.3	107 ± 2	4818 ± 100[a]	-0.32 ± 0.12[a]	$0.99^{+0.10}_{-0.07}$	$5.51^{+0.26}_{-0.19}$	$9.03^{+2.79}_{-2.72}$
220548055	4313	14.1 ± 0.3	201 ± 8	4966 ± 70[b]	0.05 ± 0.1[b]	$1.61^{+0.13}_{-0.12}$	$5.15^{+0.18}_{-0.17}$	$2.03^{+0.64}_{-0.45}$
215745876	181342	14.4 ± 0.3	209 ± 6	4965 ± 80[b]	0.15 ± 0.1[b]	$1.73^{+0.18}_{-0.13}$	$5.23^{+0.25}_{-0.18}$	$1.69^{+0.47}_{-0.41}$
220222356	5319	15.9 ± 0.5	216 ± 3	4869 ± 80[b]	0.02 ± 0.1[b]	$1.25^{+0.11}_{-0.10}$	$4.37^{+0.17}_{0.17}$	$5.04^{+1.78}_{-1.30}$
8566020*	185351	15.6±0.2	230± 7	5035 ± 80[c]	0.1 ± 0.1[c]	$1.77^{+0.08}_{-0.08}$	$5.02^{+0.12}_{-0.11}$	$1.51^{+0.17}_{-0.14}$
205924248	212771	16.5± 0.3	231 ± 3	5065 ± 95[d]	-0.1 ± 0.12[d]	$1.46^{+0.09}_{-0.09}$	$4.53^{+0.13}_{-0.13}$	$2.46^{+0.67}_{-0.50}$
228737206*	106270	32.6 ± 0.5	539 ± 13	5601 ± 65[b]	0.06 ± 0.1[b]	$1.52^{+0.04}_{-0.05}$	$2.95^{+0.04}_{-0.04}$	$2.26^{+0.06}_{-0.05}$

PARAM uses [M/H], which we take to equal [Fe/H] for all stars
Quoted errors on mass, radius and age are the 68% credible interval from PARAM

* Gaia TGAS parallaxes were unavailable, or believed unreliable (see Sec 2.5.2), and so the *Hipparcos* parallax is used instead in the construction of the stellar luminosity.
[a] Wittenmyer et al. (2016).
[b] Mortier et al. (2013).
[c] Ghezzi et al. (2015).
[d] Campante et al. (2017).

With the results from PARAM we can now compare the stellar masses derived from asteroseismology with the other literature values. Fig 2.2 shows the different mass estimates from available literature sources (see Table 2.5), with the masses reported in the planet discovery or survey paper, our primary comparison mass, as black stars. The asteroseismic masses (red diamonds) are shown alongside other literature values (points).

For the survey mass of HD 185351 no error was provided with the value in Bowler et al. (2010). We adopt the $\sigma_M = 0.07$ from Johnson et al. (2014), who in their interpolation of spectroscopic parameters onto isochrones recovered a similar mass to Bowler et al. (2010).

The survey mass of HD 145428 in Wittenmyer et al. (2016) also has no reported formal error bar, although the work quotes "typical uncertainties 0.15-0.25$M_\odot$". As such we take $0.2M_\odot$ as the uncertainty.

A striking feature of Fig 2.2 is the size of the error bars on each literature mass value, compared to the scatter on the mass values. Several stars have literature mass values with reported error bars of $\approx 0.1M_\odot$ i.e. quite precise estimates, but with individual mass estimates scattered across a $\geq 0.5M_\odot$ region. HD 4313, HD 181342 and HD 212771 all show this level of scatter on literature mass values.

Fig 2.3 shows the difference in mass estimates, taking the asteroseismic mass as the reference value. Values below zero indicate the literature mass is lower than the seismic mass. The lower panel in the figure shows the difference in standard deviations between the mass estimates, where the literature mass and asteroseismic mass have had their errors added in quadrature. As can be seen, 5 of the 7 stars display asteroseismic masses below the masses reported in the planet discovery/survey paper, however at a $\leq 2\sigma$ level. HD 212771 and HD 106270 show the opposite behaviour. We caution against taking this difference in asteroseismic masses to be evidence for a systematic shift in stellar mass, due to the small sample size. The average mass offset of the seismic to survey mass is $\Delta \mathrm{M} = 0.07 \pm 0.09 \mathrm{M}_{\odot}$.

A simple Monte-Carlo test was performed to investigate the probability that 5 out of 7 proxy spectroscopic masses would exceed 5 proxy seismic masses for our quoted uncertainties, assuming both of the masses are drawn from normal distributions with a mean of the seismic mass. We found that for a million independent realisations, 16% of the time 5 of the proxy spectroscopic masses exceed the proxy seismic masses. As such, we see that there is no clear bias between asteroseismic masses and other methods. If we instead derive model independent asteroseismic masses- using the well known asteroseismic scaling relations (e.g. see discussion in Chaplin & Miglio 2013)- we find no difference to this result, or other results in the paper.

In Sec 2.1 we discuss that the term "retired A star" can be used to describe masses associated with hot F stars as well as A type stars. However, if we consider the masses in Table 2.2, neither HD 145428 ($0.99 \mathrm{M}_{\odot}$) or HD 5319 ($1.25 \mathrm{M}_{\odot}$) can be categorized as such. If we therefore discard these stars, then only 3 of the 5 remaining stars have seismic masses below the survey mass, with the average offset $\Delta \mathrm{M} = 0.02 \pm 0.09 \mathrm{M}_{\odot}$.

Since the survey masses are a heterogeneous sample of masses, we also compare the seismic masses to several other literature sources (see Table 2.5). Unfortunately,

Table 2.3: The mean fractional offset of various sets of homogeneous literature mass sources compared to the seismic mass.

Reference	N Stars	Offset
Discovery/Survey	7	1.07 ± 0.07
Mortier et al. (2013)[a]	5	0.97 ± 0.03
Mortier et al. (2013)[b]	5	0.88 ± 0.03
Jofré et al. (2015a)	4	1.06 ± 0.01
Bonfanti et al. (2015)	5	0.97 ± 0.05
Bonfanti et al. (2016)	5	0.91 ± 0.03

[a] Tsantaki et al. (2013) line list.
[b] Hekker & Meléndez (2007) line list.

no single source has masses for all of our stars, and so each homogeneous set of reference masses is a subset of the ensemble. The average ratios are shown in Table 2.3. This choice of reference literature mass has a strong impact on the size (and sign) of any observed mass offset. Fig 2.8 shows the distribution of mass ratios for each literature reference mass.

2.7 Discussion

In order to investigate the robustness of recovering single star masses from stellar models, with or without the inclusion of asteroseismic parameters, we now explore the potential biases from the use of different stellar models, inputs, and error bars on the recovered stellar mass.

2.7.1 Use of different constraints

Throughout this work we have considered the asteroseismic mass to be the mass returned by PARAM using all available asteroseismic, spectroscopic and parallax/luminosity constraints. To see how much the non-asteroseismic constraints are influencing the final stellar mass, we also ran PARAM using only $T_{\rm eff}$, [Fe/H] and luminosity, i.e. without seismology. This was done in an effort to emulate the procedure used in Johnson et al. (2010a), using the same constraints, but differing model grids. Ghezzi & Johnson (2015) previously found that stellar masses can be recovered to good precision using PARSEC stellar models and only spectroscopic

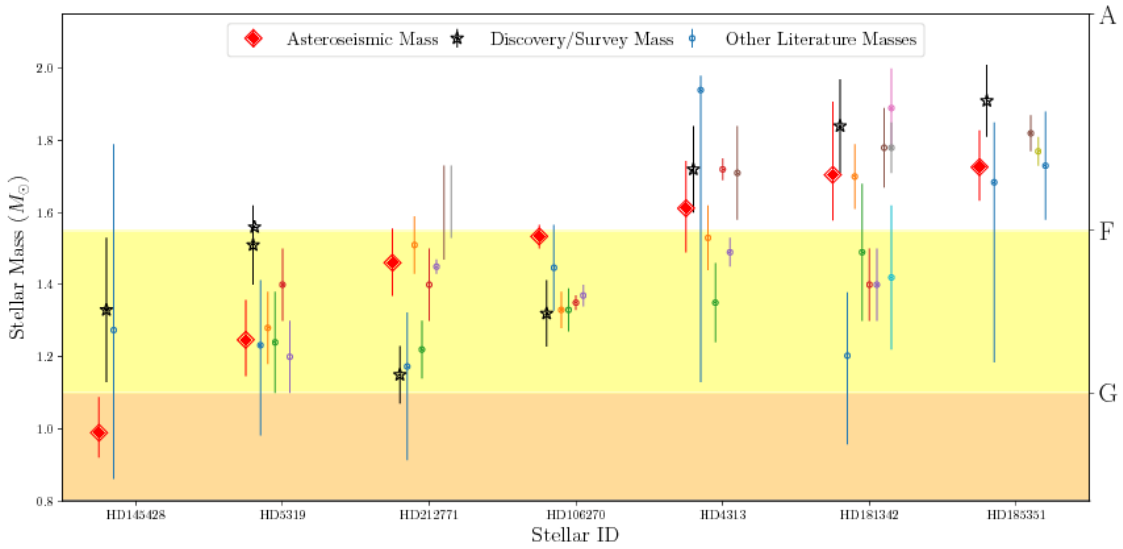

Figure 2.2: Mass vs ID, the horizontal bars indicate approximate spectral type on the main sequence, (AFG corresponding to white, yellow and orange respectively). Black stars indicate the mass of the star as reported in the planet survey or planet detection paper. Red diamonds indicate the PARAM stellar mass from Table 2.2, whilst dots indicate other literature values for each star. As can be seen for several of the stars (HD 5319, HD 145428, HD 181342 and HD 212771), the different mass estimates can cover the entire spectral range of G to A type.

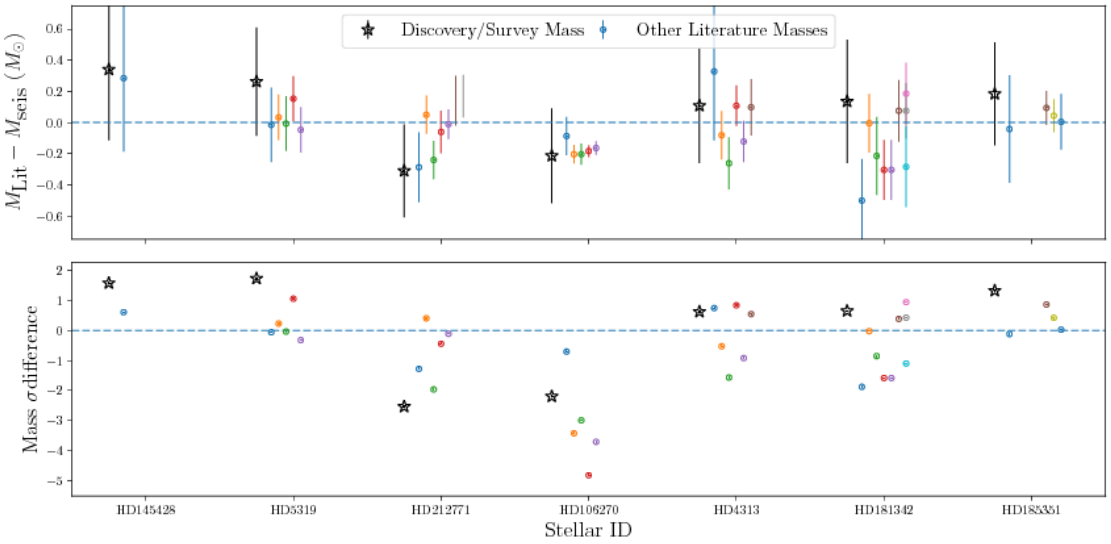

Figure 2.3: Difference between literature and asteroseismic masses, against stellar ID, arranged by increasing stellar mass. Negative values indicate the asteroseismic mass is greater than the literature mass. Again we plot the mass difference with the planet survey mass as a black star. The error bars are the mean seismic error added in quadrature to the literature error bar. The lower panel shows the σ difference between the seismic mass and literature mass, where the errors have been added in quadrature.

constraints. The different mass results for each star are shown in Fig 2.4 and are summarised in Table 2.4.

Before we discuss the results, we introduce the additional modelling performed using different underlying physics in the stellar models chosen.

2.7.2 Use of different model grids

To test the sensitivity of the derived stellar masses to the models used, extra grids of MESA models were created. The models described in Sec 2.5 include a convective-overshooting parameter $\alpha_{\rm ov}$ during the main sequence, which changes the size of the helium core during the red giant branch phase. This was set to $\alpha_{\rm ov} = 0.2H_p$ where H_p is the pressure scale height, and is a typical value adopted in the literature (Deheuvels et al., 2016). To investigate the impact of changing the underlying model physics on the final stellar mass result, new grids of models with the overshooting parameter adjusted to $\alpha_{\rm ov} = 0.1H_p$ or 0 were generated and PARAM run using these new models. This parameter was chosen to be varied, since stars in the mass range of retired A stars have convective core during the main sequence. Two further grids of models were used. First, we adopted PARSEC stellar models, which parameterise overshooting as a mass dependent parameter (see Bressan et al. 2012; Bossini et al. 2015). Second, a grid of MIST (MESA Isochrones and Stellar Tracks, Choi et al. 2016) models was used in conjunction with the code ISOCLASSIFY.[5]

Isolating any stellar mass difference between MESA and PARSEC to a single parameter is not possible, since multiple model parameters are different between the models. Additionally there are multiple differences between the MESA tracks used in Sec 2.5 and the MIST tracks. The use here of these different tracks is to explore overall mass differences between the different grids, and not to define the precise cause of such a difference.

If we consider first the lower mass stars (HD 5319, HD 145428 and HD 212771), there is no clear trend with overshooting, nor does the inclusion of seismology pro-

[5]see and https://github.com/danxhuber/isoclassify for full details of the code

duce a noticeable shift in mass, with the exception of the PARSEC tracks. The inclusion of luminosity alongside seismic constraints provides the smallest uncertainties.

For the higher mass stars (HD 4313, HD 181342 and HD 185351), there is a clear trend in increasing mass with decreasing overshooting parameter. The recovered masses using seismic constraints are also in general above the mass estimates without seismic constraints. Whilst for HD 4313 the shift in mass is fairly minor, for HD 181342 and HD 185351 the mass offset is $\Delta M \sim 0.2 M_{\odot}$. The greatest disparity is between PARSEC results with and without seismic constraints. Again we note that for 5 of the 7 stars in the ensemble, all of the recovered mass estimates are below the masses reported in the planet discovery papers.

Finally we look at the subgiant HD 106270. There appears to be no strong mass-overshooting parameter dependence, however the MESA models produce significantly different masses to the PARSEC and MIST models that should be investigated more closely. Additionally, the mass estimates recovered from the MESA models without seismic constraints are significantly lower with $\Delta M \sim 0.2 M_{\odot}$.

When we consider the masses returned without the use of the seismology (blue points in Fig 2.4) emulating Johnson et al. (2010a), using the same underlying models as was used with the seismic constraints in Sec 2.5, we fail to recover the same mass as is reported in the discovery paper in most cases. This disparity is presumably due to differences in the underlying stellar models. This highlights that stellar modelling is far from completed, with individuals trusting one set of models over another by personal choice alone.

When comparing the MIST masses (purple crosses) to the benchmark seismic masses (blue stars), the MIST results typically recover a higher mass. If we include HD 106270, for which the MIST mass is $\sim 0.1 M_{\odot}$ lower than the benchmark mass, then the average mass offset of the MIST masses is $\Delta M = 0.03 \pm 0.06 M_{\odot}$. However if we remove HD 106270 the MIST average mass shift is $\Delta M = 0.05 \pm 0.04 M_{\odot}$.

Table 2.4: Comparing stellar masses estimated using differing physics and constraints. All in Solar masses $M_\odot$

EPIC/KIC	HD	MESA[a]	MESA[b]($\alpha_{ov} = 0.0H_p$)	PARSEC[c]	Isoclassify[d]
203514293	145428	$1.05^{+0.23}_{-0.12}$	$0.97^{+0.09}_{-0.06}$	$0.99^{+0.10}_{-0.07}$	$1.17^{+0.14}_{-0.12}$
220548055	4313	$1.56^{+0.14}_{-0.16}$	$1.67^{+0.14}_{-0.14}$	$1.55^{+0.15}_{-0.16}$	$1.67^{+0.18}_{-0.15}$
215745876	181342	$1.50^{+0.19}_{-0.23}$	$1.75^{+0.14}_{-0.13}$	$1.74^{+0.14}_{-0.15}$	$1.82^{+0.20}_{-0.20}$
220222356	5319	$1.22^{+0.19}_{-0.17}$	$1.24^{+0.11}_{-0.10}$	$1.23^{+0.09}_{-0.10}$	$1.35^{+0.11}_{-0.11}$
8566020	185351	$1.50^{+0.17}_{-0.22}$	$1.74^{0.08}_{-0.08}$	$1.80^{+0.09}_{-0.09}$	$1.83^{+0.12}_{-0.10}$
205924248	212771	$1.41^{+0.17}_{-0.21}$	$1.45^{+0.10}_{-0.10}$	$1.38^{+0.10}_{-0.07}$	$1.47^{+0.09}_{-0.08}$
228737206	106270	$1.37^{+0.07}_{-0.07}$	$1.56^{+0.04}_{-0.04}$	$1.42^{+0.02}_{-0.02}$	$1.41^{+0.03}_{-0.06}$

[a] MESA models ($\alpha_{ov} = 0.2H_p$) with [Fe/H], T_{eff} and luminosity
[b] MESA models ran with $\alpha_{ov} = 0.0H_p$
[c] PARSEC models
[d] MIST models ran with ISOCLASSIFY

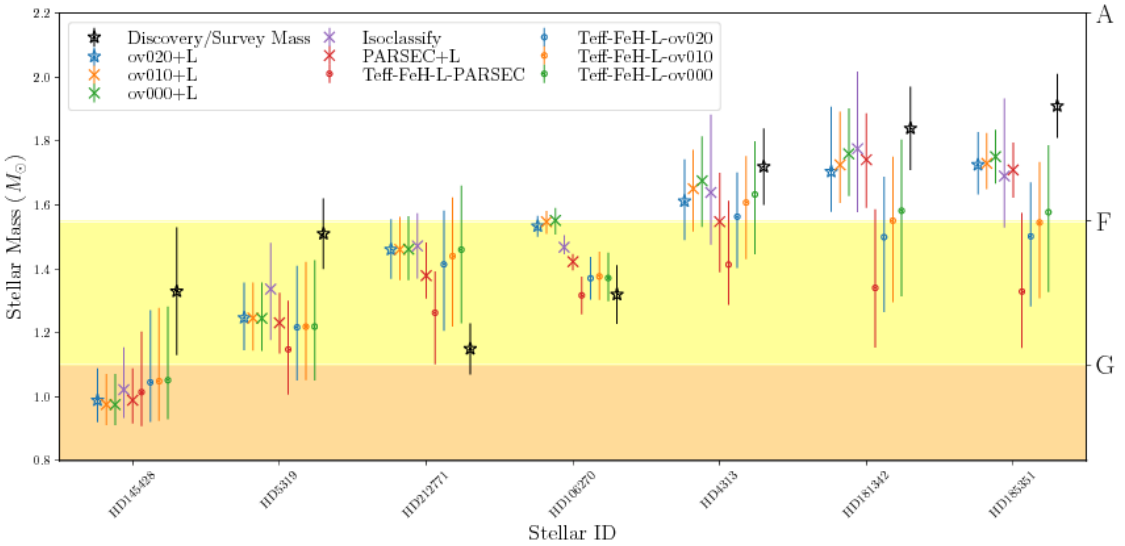

Figure 2.4: All the different mass estimates using MESA, PARSEC and MIST grids (labelled ISOCLASSIFY), the MESA and PARSEC grids were ran with and without seismic constraints. Blue stars are the results in Table 2.2. Crosses are masses with seismic and luminosity constraints, points are non-seismic constraints only (T_{eff}, [Fe/H], L). The overshooting parameter used in the models is indicated by the "ov0*" label. PARSEC tracks show significant shifts, as do non-seismic results at higher masses. Subgiant HD 106270 shows unique behaviour most likely due to being a subgiant, rather than red giant.

2.7.3 Potential biases in spectroscopic parameters

An additional discrepancy to highlight is that not only are the final mass values derived from spectroscopic parameters in disagreement with each other, possibly caused by differing physics in the models used in each paper during the recovery of the stellar mass, but also the underlying spectroscopic values ($T_{\rm eff}$, $\log g$, and [Fe/H]) can be discrepant at a significant level. Fig 2.5 highlights this problem. For two of the stars in the sample, HD 106270 and HD 181342, literature $T_{\rm eff}$ and $\log g$ values are plotted over a grid of MESA tracks, using the same physics as in Sec 2.5. In particular HD 106270 highlights that reported spectroscopic values may be highly precise, but show significant disagreement to other literature values (see Blanco-Cuaresma et al. 2016 for more discussion on the impact of different spectroscopic pipelines and assumed atmospheric physics on derived parameters). The reported values are highly scattered across the subgiant branch in the Kiel diagram in Fig 2.5. HD 181342, shown in black, highlights the additional problem with targeting red giant branch stars for planet surveys. As the star evolves off the subgiant branch, and begins the ascent of the giant branch, the stellar evolutionary tracks across a wide range of masses converge into a narrow region of parameter space, with tracks of differing mass and metallicity crossing. In the case of HD 181342, taking only the [Fe/H] =0.0 tracks, masses from $1.2 - 1.8 M_{\odot}$ are crossed.

In this highly degenerate parameter space it is naturally difficult to search for and isolate the true stellar mass, requiring highly precise and accurate temperatures to help alleviate the degeneracy. It is in this area that the benefits of asteroseismology become clear, as the additional constraint, provided by the asteroseismic observations allow us to break the degeneracy between the spectroscopic parameters to recover a better estimate of the stellar mass.

Whilst the temperature and metallicity uncertainties presented in Table 2.1 are around 0.1 dex and ∼80K respectively, several of the planet discovery papers for the stars in the ensemble present much smaller uncertainties, e.g., HD 4313, HD

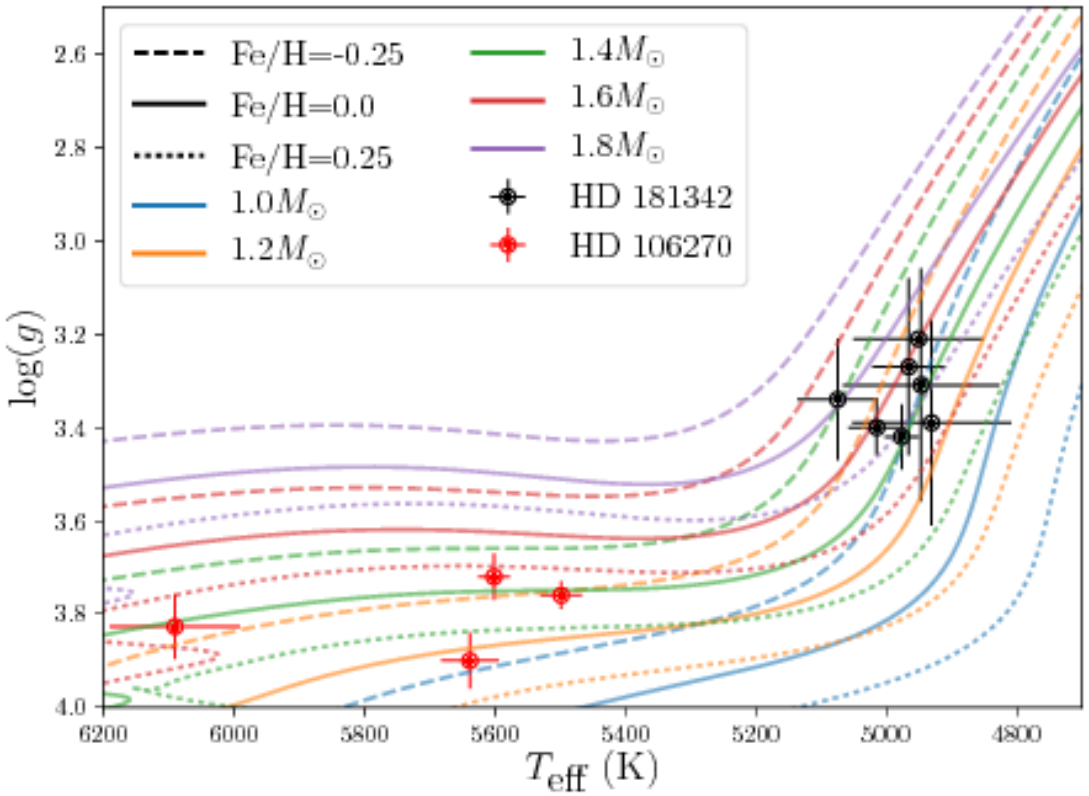

Figure 2.5: Literature spectroscopic parameters for two of the stars in the sample, showing multiple stellar tracks crossed within the uncertainty region. HD 106270 (red) shows that whilst highly precise spectroscopic values are reported in the literature, this limits the parameter space that isochrone fitting can explore, which can lead to disagreement in recovered masses at a significant level. HD 181342 near the base of the red giant branch shows the convergence of the stellar tracks in that region, increasing the difficultly of recovering the stellar parameters.

181342, HD 212771 all presented in Johnson et al. (2010a) have reported errors $\sigma_{\rm [Fe/H]} = 0.03$dex, $\sigma_{\rm Teff} = 44K$ and $\sigma_L = 0.5 L_\odot$, as does HD 106270 in Johnson et al. (2011). Giguere et al. (2015) quote the same $\sigma_{\rm [Fe/H]}$ and $\sigma_{\rm Teff}$ for HD 5319. These spectroscopic parameters and uncertainties were recovered using the package Spectroscopy Made Easy (SME, Valenti & Piskunov 1996). These uncertainties appear to represent modelling uncertainties, rather than true uncertainties on the parameters.

To explore what impact such tight error bars might have on inferred stellar masses, PARAM was run once more, using the MESA models with overshooting set to $\alpha_{\rm ov} = 0.2 H_p$ (i.e. identical physics and constraints to the masses in Table 2.2), with the inclusion of the asteroseismic constraints in the fitting. The one change here was a systematic reduction of the error bars on [Fe/H], $T_{\rm eff}$ and L. In theory, since the same input values and physics are being used, the same values for the stellar mass should be recovered, however this is not what we find. We have effectively shrunk the available parameter space for PARAM to explore. This parameter space is smaller since the error bars on the input parameters define the width of prior used in the Bayesian methodology. With smaller uncertainties the prior is narrower, and so influences the final results more strongly if the underlying value lies away from the mean of the prior (see da Silva et al. 2006 for more details). To investigate how strongly the seismic values were influencing the recovered parameters, we also ran PARAM using the smaller error bars, without seismic constraints being used, and these results are shown as orange points in Fig 2.6. The blue points in Fig 2.6 are the results from PARAM using the reduced uncertainties, but including seismic constraints. These mass estimates should agree with the blue stars (the benchmark asteroseismic mass from Table 2.2) given the same underlying physics and physical parameters. The only change is a reduction in the size of the error bars on temperature, metallicity and luminosity. What we instead see are significant departures from parity, with generally increasing disagreement as a function of

increasing mass (though HD 185351 is an exception). This suggests that potentially inaccurate effective temperatures quoted at high precision can prevent the recovery of the true stellar mass. The orange points on Fig 2.6 are the results of just using the non-seismic constraints with the deflated error bars discussed above. The recovered mass should be the same as the blue points in Fig 2.4 (see Table 2.4 for masses). Instead we see an average offset of ΔM $\sim$0.1M$_\odot$ below the mass in Fig 2.4. This is most likely due to the limited parameter space preventing a full exploration of solutions, and so suggestive that the deflated uncertainties are unreliable.

As further tests of the impact of bias in the spectroscopic parameters, PARAM was also run using only the spectroscopic parameters, with artificial biases of 1σ included on $T_{\rm eff}$ and [Fe/H]. As Fig 2.6 shows, the inclusion of 1σ shifts in $T_{\rm eff}$ (triangles) or [Fe/H] (crosses) induces shifts of $\sim$0.2M$_\odot$ in stellar mass for the giant stars.

The subgiant, HD 106270, shows quite separate behaviour and appears more resistant to biases, though it does display a strong disparity in stellar mass estimates with or without asteroseismic constraints. This may be due to the wider separation between tracks of differing mass and metallicity at this point in the HR diagram (as seen in Fig 2.5). Additionally, since most of the evolution is "sideways" on the subgiant branch, as the star retains a similar luminosity across a range of temperatures, a single mass track can recover the observed spectroscopic parameters (and luminosity) with an adjustment in stellar age.

One potential issue that has not yet been addressed is the systematic offset in $\log g$ between seismology and spectroscopy. We compared the $\log_{\rm seis} g$ recovered with the benchmark seismic mass, to the $\log_{\rm spec} g$ reported in the literature source from which we take the $T_{\rm eff}$ and [Fe/H]. We find the spectroscopic gravities to be overestimated by an average of 0.1dex. Since the spectroscopic parameters are correlated, this may have introduced biases in the temperature and metallicity we have used in the modelling. To test the impact of any bias, we correct the $T_{\rm eff}$

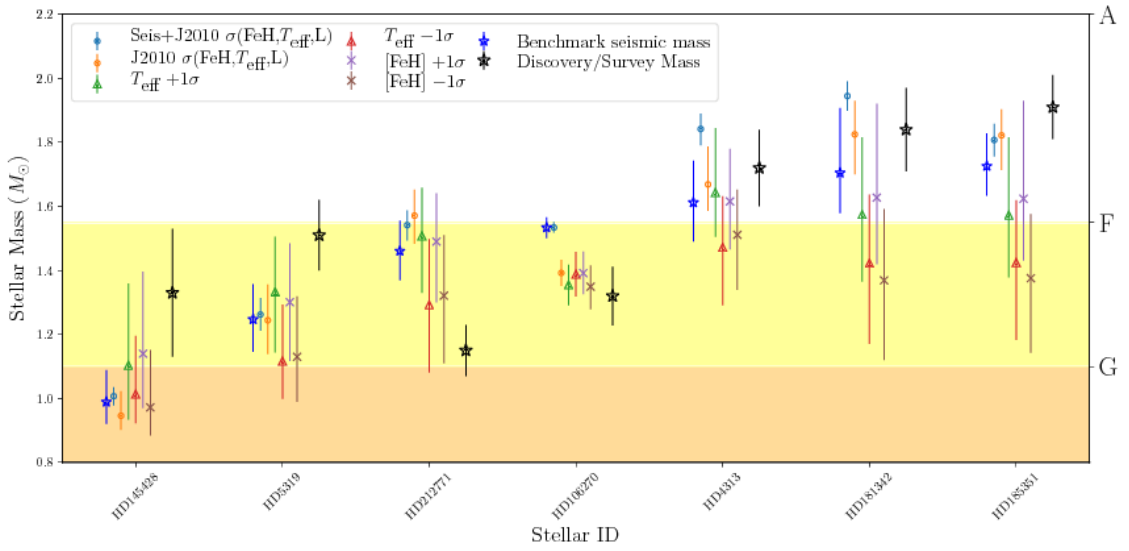

Figure 2.6: Investigating the effect of biases in the spectroscopic parameters, and underestimated error bars. Black stars are the discovery masses, blue stars are the benchmark asteroseismic masses in Table 2.2. Blue and orange dots are the same inputs as Table 2.2 with deflated errors to $\sigma_{[\mathrm{Fe/H}]} = 0.03$dex, $\sigma_{T\mathrm{eff}} = 44$K and $\sigma_L = 0.5\mathrm{L}_\odot$, with and without seismic constraint respectively. Remaining markers are the inclusion of 1σ biases in T_{eff} (triangles) and [Fe/H] (crosses), using the error values in Table 2.2

and [Fe/H] by $\Delta T_{\mathrm{eff}} = 500\Delta \log g$[dex], and Δ[Fe/H] $=0.3\Delta \log g$[dex] (Huber et al. 2013b, see Figure 2 and surrounding text therein). PARAM was re-run using the MESA models described in Sec 2.5, with the inclusion of the seismic parameters. The mean shift in mass with respect to the benchmark seismic mass was $\Delta M = -0.0097 \pm 0.010\mathrm{M}_\odot$. As such, we do not see any evidence for a significant shift in the estimated masses.

2.7.4 Potential biases in asteroseismic parameters

To ensure a thorough test of potential biases, the input ν_{max}, $\Delta\nu$ values were also separately perturbed by 1σ and PARAM was re-run. We note that in Table 2.2 both seismic parameters are given to a similar level of precision as the temperatures (average precision on $\nu_{\mathrm{max}} = 2.4\%$, $\Delta\nu = 2.2\%$ and $T_{\mathrm{eff}} = 1.6\%$). Each 1σ perturbation produced an mean absolute shift in mass of $\lesssim 0.04 \pm 0.009\mathrm{M}_\odot$. These mass shifts are approximately five times smaller than those given by the 1σ perturbations to the spectroscopic parameters.

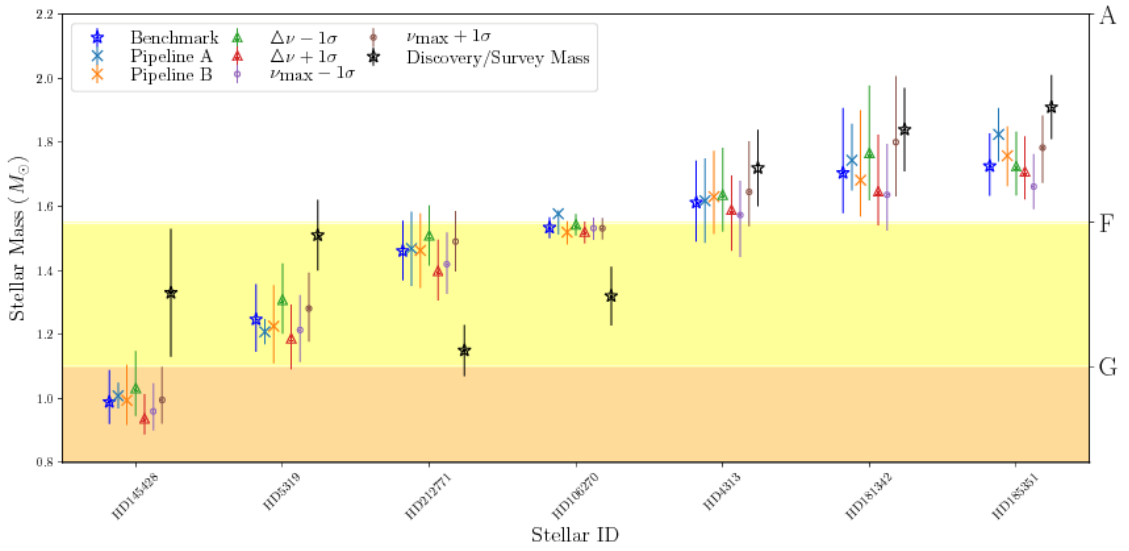

Figure 2.7: Investigating the effect of biases in the seismic parameters, and potentially underestimated error bars. Black stars are the discovery masses, blue stars are the benchmark asteroseismic masses in Table 2.2. Pipeline A and B (crosses) are two of the pipeline used to recover the asteroseismic parameters. Triangles are the $\Delta\nu$ values in Table 2.2 perturbed by 1σ. Dots are the $\nu_{\rm max}$ values in Table 2.2 perturbed by 1σ.

In Sec 2.3 we added additional uncertainties to the error bars on the seismic quantities returned by the Huber et al. (2009) pipeline to account for scatter between pipelines. Here, for completeness, we also tested using as inputs the seismic parameters and formal uncertainties from the other two pipelines. Again, we found very small changes in mass (at the level of or smaller than the uncertainties on the data). These results are shown in Fig 2.7.

2.8 Conclusions

This work has explored the masses of so-called "retired A Stars" and the impact of differing stellar models and the individual constraints used on the recovery of the stellar mass for single stars. In our ensemble of 7 stars, we find for 5 of the stars a mild shift to lower mass, when the asteroseismic mass is compared to the mass reported in the planet discovery paper. This mass shift is not significant. Additionally, the scale and sign of this mass offset is highly dependent on the chosen reference masses, as different literature masses for the ensemble cover the mass range

$1-2M_{\odot}$, with optimistic error bars on literature masses resulting in significant offsets between different reference masses. We note that Stello et al. (in prep) find a similar, non-significant offset for stars of comparable mass to ours (from analysis of ground-based asteroseismic data collected on a sample of very bright A-type hosts), with evidence for an offset in a higher range of mass not explored in our sample. Stello et al. also find that the scatter on the literature values is of comparable size to the observed mass offset.

We also find that the mass difference can be explained through use of differing constraints during the recovery process. We also find that $\approx 0.2M_{\odot}$ shifts in mass can be produced by only 1σ changes in temperature or metallicity, if only using spectroscopic and luminosity constraints. Additionally we find that even with the inclusion of asteroseismology, potentially inaccurate effective temperatures quoted with high precision makes the recovery of the true (model dependent) mass impossible. To solve this effective spectroscopic temperatures need calibrating to results from interferometry or eclipsing binaries. Finally, we find that the use of optimistic uncertainties on input parameters has the potential to significantly bias the recovered stellar masses, as does inaccurate stellar model physics. The consequence of such an action would be to bias inferred planet occurrence rates, an argument broadly in agreement with the space-motion based argument of Schlaufman & Winn (2013), i.e., that the masses of evolved exoplanet hosts must be overestimated to explain the observed space motions of the same stars.

Additionally an exploration of differences in recovered mass using differing stellar grids needs to be applied to a far larger number of stars, along with a full exploration of which underlying physical parameters are the cause of systematic shifts in mass. This will be the product of future work. Asteroseismic observations of more evolved exoplanet hosts will also be provided by data from later K2 campaigns and from the upcoming NASA TESS Mission (e.g. see Campante et al. 2016).

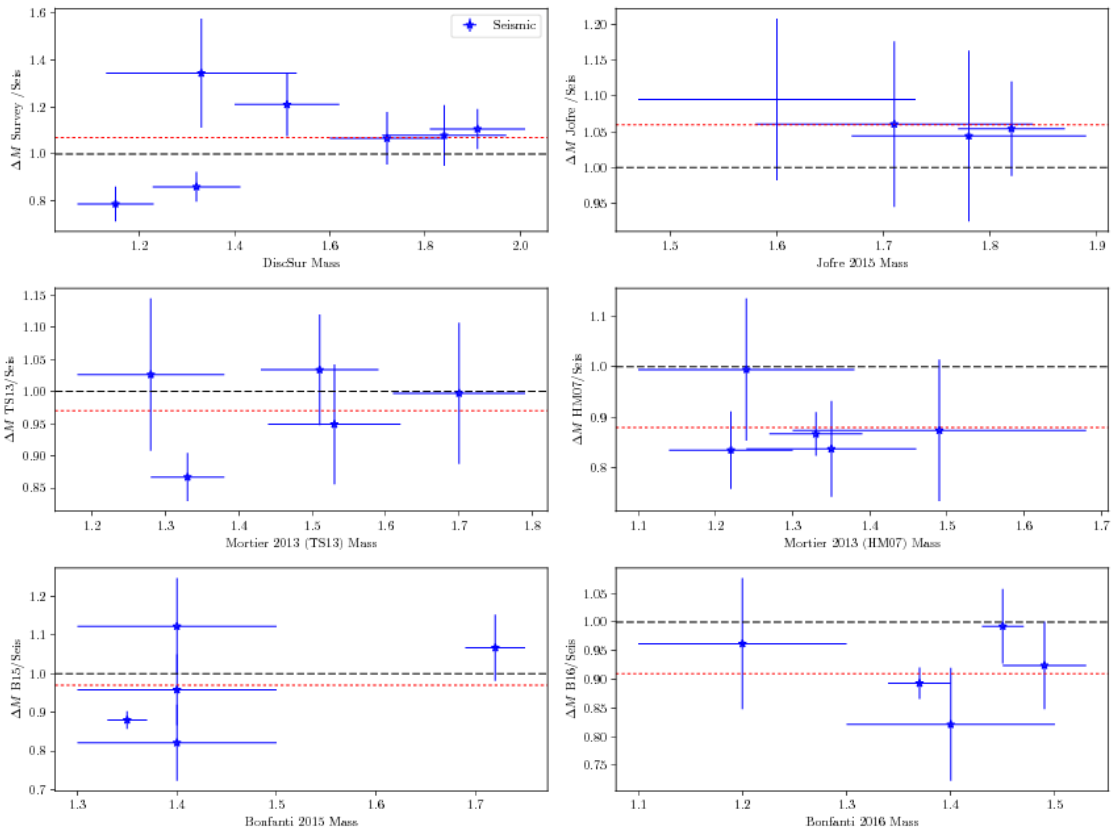

Figure 2.8: For stars with several available literature masses, the ratio of seismic to literature mass is shown, against the literature mass value. The red dotted line in each subplot is the average ratio of Table 2.3. Black dashed line is parity

2.9 Available literature masses

Table 2.5: All available literature masses for each star in the ensemble. The values are primarily estimated from the observed spectroscopic parameters. The mass values from Huber et al. (2014) are estimated from the *Hipparcos* parallax.

EPIC/KIC	HD	Huber[1]	Johnson[2]	Mortier[3,a]	Mortier[3,b]
203514293	145428	$1.274^{+0.516}_{-0.413}$			
220548055	4313	$1.94^{+0.039}_{-0.849}$	1.72 ± 0.12	1.53 ± 0.09	1.35 ± 0.11
215745876	181342	$1.203^{+0.176}_{-0.246}$	1.84 ± 0.13	1.7 ± 0.09	1.49 ± 0.19
220222356	5319	$1.232^{+0.178}_{-0.250}$		1.28 ± 0.1	1.24 ± 0.14
8566020	185351				
205924248	212771	$1.173^{+0.154}_{-0.263}$	1.15 ± 0.08	1.51 ± 0.08	1.22 ± 0.08
228737206	106270	$1.447^{+0.119}_{-0.119}$	1.32 ± 0.092[2a]	1.33 ± 0.05	1.33 ± 0.06
EPIC/KIC	HD	Bofanti[4]	Bofanti[3,b]	Jofré[6]	Maldonado[7]
203514293	145428				
220548055	4313	1.72 ± 0.03	1.49 ± 0.04	1.71 ± 0.13	
215745876	181342	1.40 ± 0.1	1.40 ± 0.1	1.78 ± 0.11	1.78 ± 0.07
220222356	5319	1.40 ± 0.1	1.2 ± 0.1		
8566020	185351			1.82 ± 0.05	
205924248	212771	1.40 ± 0.1	1.45 ± 0.02	1.60 ± 0.13	1.63 ± 0.1
228737206	106270	1.35 ± 0.02	1.37 ± 0.03		
EPIC/KIC	HD	Wittenmyer[8]	Huber[9]	Jones[10]	Robinson[11]
203514293	145428	1.33 ± 0.2			
220548055	4313				
215745876	181342	1.42 ± 0.2		1.89 ± 0.11	
220222356	5319				1.56 ± 0.18
8566020	185351		$1.684^{+0.166}_{-0.499}$		
205924248	212771				
228737206	106270				
EPIC/KIC	HD	Giguere[12]	Reffert[13]	Johnson[14]	Ghezzi[15]
203514293	145428				
220548055	4313				
215745876	181342				
220222356	5319	1.51 ± 0.11			
8566020	185351		1.73 ± 0.15	1.60 ± 0.08[c] 1.99 ± 0.23[d] 1.90 ± 0.15[e] 1.87 ± 0.07[f]	1.77 ± 0.04
205924248	212771				
228737206	106270				

[a] Tsantaki et al. (2013) line list for the stars cooler than 5200 K, and the Sousa et al. (2008) line list for the hotter stars.
[b] Hekker & Meléndez (2007) line list

[1] Huber et al. (2016).
[2] Johnson et al. (2010a).
[2a] Johnson et al. (2011)
[3] Mortier et al. (2013).
[4] Bonfanti et al. (2015).
[5] Bonfanti et al. (2016).
[6] Jofré et al. (2015a).
[7] Maldonado et al. (2013).
[8] Wittenmyer et al. (2016).
[9] Huber et al. (2014).
[10] Jones et al. (2016).
[11] Robinson et al. (2007).
[12] Giguere et al. (2015).
[13] Reffert et al. (2015).
[14] Johnson et al. (2014).
[c] Interferometric radius, combined with asteroseismology.
[d] Scaling relation, based on $\Delta\nu = 15.4 \pm 0.2\mu$Hz, $\nu_{\rm max} = 229.8 \pm 6.0\mu$Hz.
[e] BaSTI Grid fitting with asteroseismology and SME spectroscopy.
[f] Grid fitting with only SME spectroscopy, iterated with Y^2 grids to a converged $\log_{10} g$.
[15] Ghezzi et al. (2015).

3 Evolved Exoplanet Hosts and Binaries

The work in this chapter related to Kepler Object of Interest (KOI) 6194 is presented in a format similar to a manuscript currently in preparation. I will be first author on this work. Radial velocity measurements for KOI-6194 were provided by Dan Huber (Keck observations), and Allyson Bieryla and David Latham (TRES). Work on the binary system KOI-3890 (Sec 3.7) will appear in Kuszlewicz et al. (in prep), in which I am second author and performed the orbital fitting, along with the secondary asteroseismic background fitting and global asteroseismic parameter extraction. I also performed the stellar modelling, to recover the stellar properties, again using PARAM. *The asteroseismic analysis performed to extract the inclination angle for both systems is described in Kuszlewicz (2017) and is included here for completeness. The spectroscopic parameters and radial velocities derived from TRES observations were provided by Allyson Bieryla and David Latham. The asteroseismic period spacing for KOI 3890 was provided by Saskia Hekker*

3.1 Introduction

The *Kepler* mission has been fundamental in redefining our knowledge of exoplanets and exoplanetary systems. One key area that *Kepler* (Borucki et al., 2010), and its continuation mission K2 (Howell et al., 2014) have identified is the discovery of short period giant planets around low luminosity red giant stars (Huber et al., 2013a; Barclay et al., 2015; Ciceri et al., 2015; Van Eylen et al., 2016). Kepler-56 (Huber et al., 2013a; Otor et al., 2016) is the archetype of this class of systems. Prior to the *Kepler* mission radial velocity surveys had typically failed to identify

short period Jupiter sized planets around giant stars. This lack of detections has two possible explanations. The most obvious is noise; red giants are intrinsically noisy stars, with large scale surface convection of significant amplitude. This noise signature, typically called "jitter" can be of comparable amplitude to the induced periodic radial velocity shift caused by an orbiting companion (Wright, 2005; Hatzes et al., 2018). The second reason is observation bias. Such systems are believed to be intrinsically rare (Fressin et al., 2013; Schlaufman & Winn, 2013), and so large surveys requiring significant telescope time are not designed to search for such systems.

For both Kepler-56 and Kepler-91, the transit analysis was benefited greatly by the asteroseismic analysis of the lightcurves. Thousands of red giant stars displaying solar-like oscillations have been detected by the *Kepler* (Stello et al., 2013a) and K2 missions (Stello et al., 2015). The detection and characterisation of stellar oscillations not only allows inferences to be made on the internal processes of stars (Mosser et al., 2012c; Montalbán et al., 2013; Eggenberger et al., 2017), they also allow access to the stellar inclination angle with respect to our line of sight (Huber et al., 2013a). In the case of Kepler-56 this lead to the first detection of a misaligned giant planet system.

The asteroseismic analysis is also of benefit to any follow-up spectroscopic observations, since it provides a strong constraint on the surface gravity of the star (Hekker et al., 2013), helping to lift the degeneracy between parameters typically recovered by spectroscopy; $\log g$, $T_{\rm eff}$ and [Fe/H] (Torres et al., 2012a) (see Chapter 1 for more information).

Further to this, to avoid biasing the transit parameters, the properties of the noise signature in the lightcurve can be accounted for. In giant stars, lightcurves show significant levels of correlated noise (Barclay et al., 2015), due to granulation and the stellar oscillations themselves. Several works have now used the inclusion of correlated noise during the transit fitting procedure to mitigate this (Grunblatt

et al., 2016, 2015; Barclay et al., 2015), however the calculations required are computational expensive.

The structure of the chapter is laid out below. Sec 3.2 discusses the *Kepler* transit observations and the on-going radial velocity follow-up observations undertaken to confirm the planetary nature of KOI 6194. Sec 3.3 details the asteroseismic characterization of the star, including the recovery of the stellar inclination angle. Sec 3.4 covers the recovery of the fundamental stellar and planet properties, including the system obliquity. Section 3.7 covers the equivalent observations of the binary star system KOI-3890, including the detection of tidally induced deformation of the primary star, and discussion on the possible future evolution of this system. First I discuss how these targets were selected for follow up observations.

3.1.1 Target Selection

Both KOI-6194 and KOI-3890 were identified as systems of interest using the NASA Exoplanet Archive (Akeson et al., 2013a), after selecting KOIs listed as candidates with $\log g < 4.0$. This left around $\sim$10 systems that required further vetting before using telescope observations. This vetting procedure used constraints on parameters listed in the Exoplanet Archive, such as the impact parameter $b < 1$. Additionally the period of the orbit was considered, with long period targets being rejected due to required telescope time.

Another useful constraint was considering feasible transit durations (of order $\sim$1 day when considering a short period planet around a low luminosity red giant star). At this point asteroseismic interest in each system was considered. Using the asteroseismic global parameters $\nu_{\rm max}$ and $\Delta\nu$, listed in Stello et al. (2013b), scaling relation masses and radii were produced using Eqs 1.19 and 1.20. Combined with the transit depth in the Exoplanet Archive, the estimated radii of the planet candidates can be calculated. Using these radii, rough guideline masses were estimated using simplistic relations, and the estimated amplitude of any radial velocity signature was

produced. This was done to consider the viability of detecting such signals around intrinsically noisy stars.

From these assessments KOI-6194 was retained due to it filling an evolutionary gap between previously detected hosts Kepler-91 and Kepler-56. KOI-3890 was retained due to the possible binary nature of the system, indicated by the large transit depth, as known binary star systems with an asteroseismic component are rare.

3.2 Observations

3.2.1 Transits

KOI-6194 (KIC 9145861, Brown et al. 2011) was observed for the 4 year duration of the *Kepler* mission at a ∼30 minute cadence. A 42 day periodic transit-shaped feature was detected by the *Kepler* pipeline and it was given the designation KOI-6194.01. An additional signal was flagged at 215 days, but this has since been determined to be a false positive, and will not be discussed further.

The long cadence (∼30 min) *Kepler* lightcurve was downloaded from the Mikulski Archive for Space Telescopes (MAST)[1], and detrended with a moving median filter, with a width of 30 days to ensure the transits are unaffected. A box least-square (BLS) search algorithm was to used to detect the transits. Fig 3.1 shows the detrended lightcurve, and the lightcurve folded on the period from the BLS, which is still the 42 day periodic signal.

3.2.2 Radial Velocity

KOI-6194 was initially observed using the TRES spectrograph (Szentgyorgyi & Furész, 2007) to measure radial velocities for the system, however these measurements were inconclusive, with no evidence of a periodic signal. However it was decided that the system required higher precision measurements. Additional obser-

[1]https://archive.stsci.edu/index.html

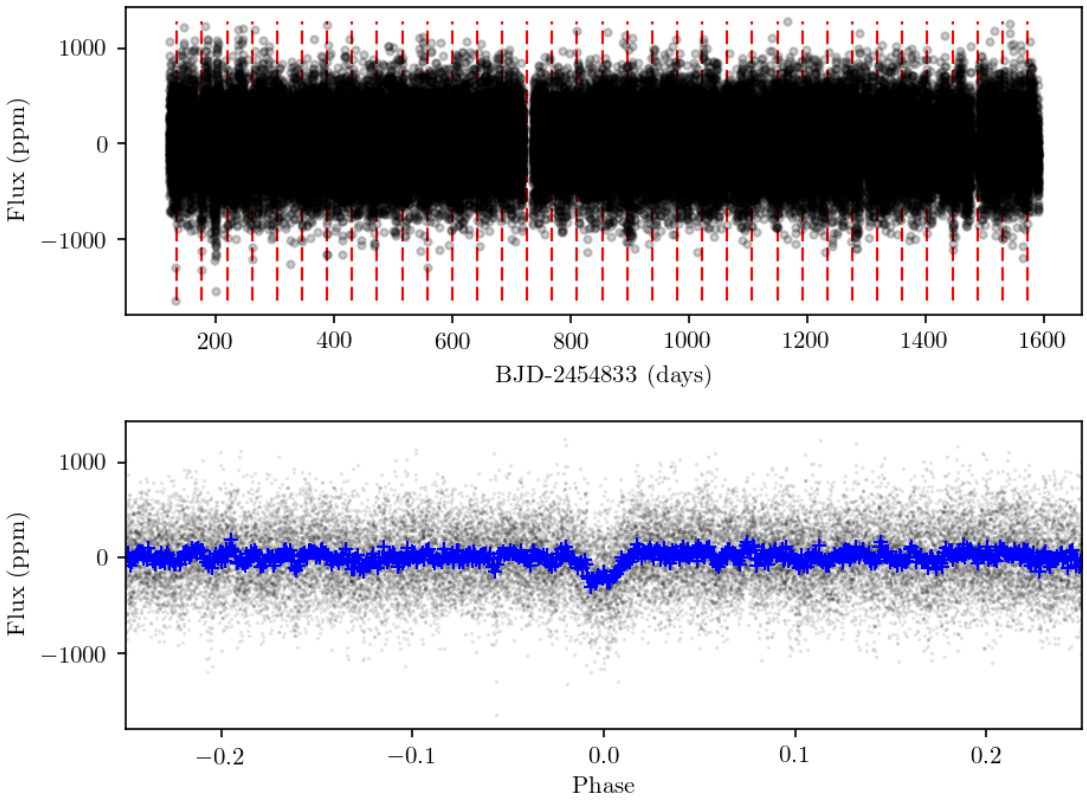

Figure 3.1: Detrended lightcurve of KOI-6194, with the location of the transits marked in the upper panel with red dashed lines. The transits are not easily distinguishable. In the lower panel, the detrended lightcurve is phase folded on the best period of the BLS search algorithm (black points). Also shown is a version averaged across 25 bins (blue), where the transit is more visible.

vations were undertaken using HIRES at the Keck observatory (Vogt et al., 1994). A total of 9 radial velocity observations have been taken presently, with more scheduled for 2018. The discussion of fitting a model to the radial velocities in Section 3.5 considers the shortcomings of so few measurements.

3.3 Asteroseismic Analysis

As a red giant host star, the star exhibits solar-like oscillations, the turbulent convection in the near surface layers driving oscillation modes inside the star. We can use these oscillations to constrain the internal and global properties of the star. In this work we used the so-called "global" asteroseismic parameters, $\nu_{\rm max}$, the frequency of maximum power, and $\Delta\nu$, the average frequency spacing between modes the same angular degree l but of subsequent radial order n. These properties were extracted from the frequency power spectrum using the method described below (see also Kallinger et al. 2014; Lund et al. 2016 for additional details). For the extraction of the asteroseismic parameters we used the KASOC power spectrum Handberg & Lund (2014a). The KASOC power spectra have any known transits filtered from the lightcurve before the power spectrum is produced. This ensured that no planetary signals should interfere with the asteroseismic analysis. It should be noted that a 42 day signal would not unduly affect the seismic analysis if the transit signal was left in the data. However shorter period planets with stronger transits can hamper seismic analysis (Handberg & Lund, 2014a).

3.3.1 Global seismic parameters

Fig 3.2 shows the fit to the granulation background using the formulation of Kallinger et al. (2014), where the granulation background is modelled as a series of zero-frequency-centered "super-Lorentzians", where the Lorentzian is raised to the power 4 rather than the standard power of 2. Also included in the background fit a Gaussian component to fit the stellar oscillations around the frequency of maximum power, $\nu_{\rm max}$. The inset in the figure shows the power spectrum of the power spectrum

(PSPS), used to identify the average large frequency separation $\Delta\nu$. For more details on the recovery of seismic parameters and fitting the background see Chapter 1.

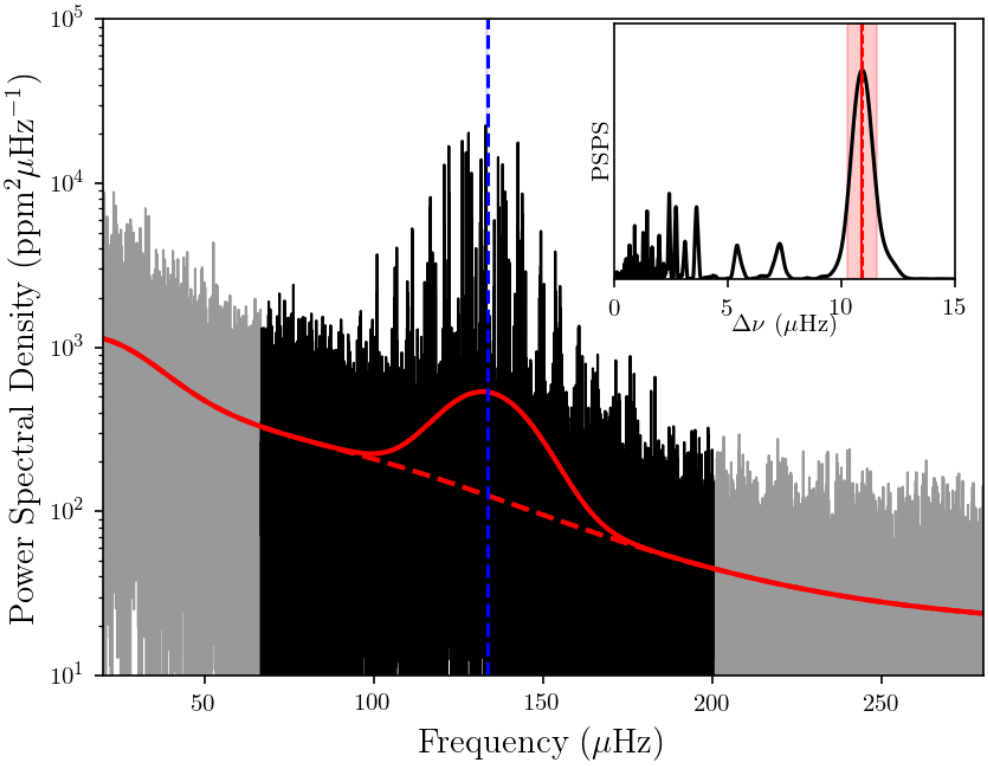

Figure 3.2: KASOC power spectrum of KOI-6194. This data was used in the asteroseismic analysis, the transits have been removed from the data, though would have had minimal affect on the data. Black is the power spectrum, red is the fit to the background, including Gaussian component around $\nu_{\rm max}$ (blue dashed), blue shaded region is 1σ region for $\nu_{\rm max}$. Inset is PSPS showing clear peak around $\Delta\nu$. Red shaded region is 1σ errorbars for $\Delta\nu$.

3.3.2 Stellar inclination angle

The derivation of the stellar inclination angle (the angle between the rotation axis of the star and our line of sight) using asteroseismology adopts the formalism derived in Gizon & Solanki (2003). Since real stars rotate, modes of the same n and l but different m are not degenerate with one another. In the case of non-radial ($l > 0$ modes) the relative amplitude of each component provides information about the inclination angle of the star. For red giants the inclination angle can be measured using $l = 1$ mixed modes (see Chapter 1 for more detail). The inclination angle

was extracted from each mixed mode by fitting the model described in Handberg & Campante (2011), which involved fitting a combination of three Lorentzians to account for any rotational splitting using the Python package EMCEE (Foreman-Mackey et al., 2013) using the likelihood function given in Anderson et al. (1990). The priors on the parameters were all taken to be uniform with the exception of the inclination angle which was taken to be isotropic ($p(i) \propto \sin i$). The inclination angle of the star was inferred from the individual mode estimates using the hierarchical method described in Kuszlewicz et al. (2018) whereby the stellar inclination angle is treated as a population distribution given noisy individual estimates from each mode. This resulted in an inclination angle of $i = 86.7^{\circ +3.3}_{-1.7}$. From this measurement the obliquity (the angle between stellar inclination and the plane of the orbit) of the system could also be estimated using a Monte-Carlo approach using Eq 5 of Morton & Winn (2014) assuming that the azimuthal angle is distributed uniformly between 0 and 2π. As a result the obliquity of the system was found to be $\phi(^{\circ}) = 6.1^{+3.2}_{-6.1}$ which is consistent with alignment. Alignment here would indicate the the stellar rotation axis is perpendicular the plane of the orbit (e.g. the Earth has an obliquity of $\sim 23^{\circ}$ to its orbital plane).

3.4 Recovery of Stellar Properties

The global asteroseismic parameters, and the spectroscopic parameters ($T_{\rm eff}$ and [Fe/H] were taken from Pinsonneault et al. (2014)) are summarised in Table 3.1. The period spacing of the star was also used in the recovery of the stellar parameters, taken from Vrard et al. (2016). These parameters will be taken forwards as inputs to stellar models to recover the estimated stellar properties (see Chapter 1 for more details on recovering stellar properties from models).

Table 3.1: Asteroseismic and spectroscopic parameters

KOI-6194	
$\nu_{\rm max}$ (μHz)	133.6± 0.3
$\Delta\nu$ (μHz)	10.9±0.7
$\Delta\Pi$ (s)	77.3 ± 0.8
$T_{\rm eff}$ (K)	4645 ± 72
[Fe/H] (dex)	0.39 ± 0.04

We use these input parameters along with a grid of MESA (Paxton et al., 2011, 2013) models to recover the fundamental stellar properties, using the Bayesian code PARAM (da Silva et al., 2006; Rodrigues et al., 2014). For full details of the input physics see Rodrigues et al. (2017). A summary of our selected "benchmark" options is as follows;

- Heavy element partition from Grevesse & Noels (1993).
- OPAL equation of state (Rogers & Nayfonov, 2002) along with OPAL opacities (Iglesias & Rogers, 1996), with complementary values at low temperatures from Ferguson et al. (2005).
- Nuclear reaction rates from NACRE (Angulo et al., 1999).
- The atmosphere model is that according to Krishna Swamy (1966).
- Mixing length theory was used to describe convection (a solar-calibrated parameter $\alpha_{\rm MLT} = 1.9657$ was adopted).
- Convective overshooting on the main sequence was set to $\alpha_{\rm ov} = 0.2H_p$, with H_p the pressure scale height. Overshooting was applied according to the Maeder (1975) step function scheme.
- No rotational mixing or diffusion was included.

Table 3.2: Fundamental stellar properties from PARAM, quoted uncertainties are the 68% credible interval.

KOI-6194	
$M_\star$ ($M_\odot$)	$1.35^{+0.06}_{-0.05}$
$R_\star$ ($R_\odot$)	$5.83^{+0.14}_{-0.11}$
Age (Gyr)	$4.96^{+0.78}_{-0.77}$

- In the stellar models $\Delta\nu$ was calculated from theoretical radial mode frequencies, not asteroseismic scaling relations.

Using the above physics, we recover the fundamental stellar properties, given in Table 3.2, using the stellar metallicity and temperature, along with the asteroseismic constraints given in Table 3.1. Luminosity was not available as a constraint for this star, due to a lack of a precise parallax measurement by *Gaia* at this time.

With the recovery of the stellar properties done, we move on to recovering the planetary parameters.

3.5 Fitting orbital model

The orbital and planetary parameters were intended to be recovered using a simultaneous MCMC[2] fit to the radial velocity and transit data (see Sec 3.5.1 for why this was not possible). The Python BATMAN package (Kreidberg, 2015) was used to model the transit, based upon the transit model of Mandel & Agol (2002). The radial velocity data were modelled as,

$$V(t) = \gamma + K\left(\cos(f(t) + \omega) + e\cos\omega\right), \tag{3.1}$$

with $f(t)$ the true anomaly, e the orbital eccentricity, ω the argument of periastron, K the radial velocity semi-amplitude and γ is the zero point offset of the Doppler velocities. The initial guess for the period was taken from a box least squares transit detection routine (Kovács et al., 2002b). No strong out of transit features are seen

[2]Using Python package EMCEE (Foreman-Mackey et al., 2013)

in the lightcurve. The star does exhibit significant levels of noise, believed to be correlated that should be accounted for and fitted simultaneously with transit to avoid biasing the transit fit. At present that is to be the focus of future work, and results presented here do no account for the correlated noise.

Limb darkening parameters were taken from Sing (2010), and were fixed in the transit model, using a quadratic formulation for the limb darkening law. Additional parameters $\sigma_{\rm LC}$ and $\sigma_{\rm RV}$ are including to account for unaccounted uncertainties. Since the *Kepler* observations are integrated over 30 minutes, the transit model is supersampled by a factor 5. If this is not done, the transit duration can be underestimated (Kreidberg, 2015).

3.5.1 Radial Velocity Fit

Preliminary fitting of just the radial velocity data highlights that the there is insufficient data to fully constrain the system parameters. Figure 3.3 shows the resulting fits of an enforced circular orbit ($e = 0, \omega = 0^\circ$), and a fit in which e and ω are free. During the fitting of the radial velocity data the period of the signal was constrained using the detected period from the *Kepler* pipeline as a Gaussian prior. To statistically compare the two models we use the Bayesian Information Criteria (BIC,Schwarz 1978);

$$\mathrm{BIC} = -2 \log L_{\rm max} + k \log N, \tag{3.2}$$

where $L_{\rm max}$ is maximised likelyhood of the particular model, k is the number of free free parameters in the model, and N the number of datapoints. In general models of lower BIC value are preferred, with the BIC penalising overly complex models. However the difference in the BIC values for two models determines how favoured one is over the other. The BIC values are given in Table 3.3. Values of ΔBIC> 6 are taken as strong evidence against the more complex model.

In this case ΔBIC$= 6.3$. This suggests the model with fixed eccentricity is preferred at a strong level. To further clarify if the orbit is eccentric additional

Table 3.3: BIC values of the two radial velocity fits

Model	BIC
Free e	78.3
Fixed $e = 0$	72.0

radial velocities observations will be needed. In the likelyhood calculation in Eq 3.2, an additional noise term has been added in quadrature to the formal uncertainties returned by the Keck pipeline, to reflect any additional stellar noise not accounted for. This additional noise, known as "jitter", is caused by the presence of the stellar oscillations themselves (along with stellar granulation). Using the scaling relation of oscillation amplitude in Kjeldsen & Bedding (1995, Eq 7),

$$v_{\rm osc} = \frac{L/{\rm L}_\odot}{M/{\rm M}_\odot}(23.4 \pm 1.4){\rm cms}^{-1}. \tag{3.3}$$

Using Eq 3.3, and the asteroseismic mass and radius of Table 3.2, along with temperature, the predicted amplitude of solar-like oscillations is $\sim$2.5ms^{-1}. To account for this an additional noise term $\sigma_{\rm RV}$ was included. Whilst the expected value of velocity jitter due to stellar oscillations is $\sim$2.5ms^{-1}, the prior on $\sigma_{\rm RV}$ has been extended beyond this to capture any additional jitter beyond this, including the imapct of both stellar granulation and any instrumental effects. The priors used in the free e and ω fit are shown in Table 3.4.

Table 3.4: Model parameters and priors for the radial velocity fit. Gaussian priors indicated by$N$(mean,standard deviation, and uniform priors by U(lower bound, upper bound). All logarithmic priors are in base 10.

Parameter	Prior
P	$N(42.295, 0.002)$ (days)
γ	$U(-100, 100)$ (m/s)
$\log K$	$U(-2, 2)$ (m/s)
$e \cos \omega$	$U(-1, 1)$
$e \sin \omega$	$U(-1, 1)$
T_R (BJD)	$U(58000, 58045)$
σ_{RV}	$U(0, 10)$ (m/s)

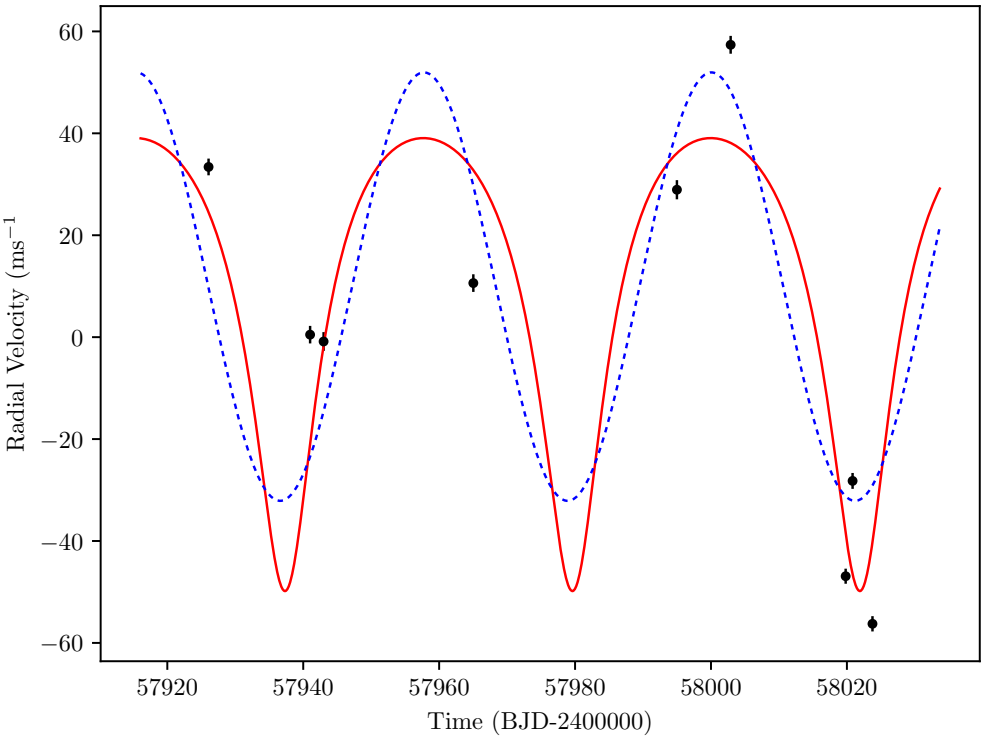

Figure 3.3: Current Keck radial velocity measurements for KOI-6194 with two models fitted to observations. Both a highly eccentric and circular model can describe the data. Additional measurements required to constrain e and ω.

While unable to strongly constrain e and w an upper limit can be placed on K.

In both fits this is constrained to $K < 45\mathrm{ms}^{-1}$. To estimate the planetary mass from K, we use,

$$K = \left(\frac{2\pi G}{P}\right)^{1/3} \frac{M_P \sin i}{(M_\star + M_P)^{2/3}} \frac{1}{(1-e^2)^{1/2}}, \tag{3.4}$$

where we can assume $\sin i \sim 1$ and $M_P \ll M_\star$. We also assume $e = 0$, to produce an upper mass limit of $M_P < 0.9^{+0.1}_{-0.1}\mathrm{M_J}$. This planet mass would place it slightly more massive (though in agreement within uncertainties) than Kepler-91, $M_P = 0.76 \pm 0.13\mathrm{M_J}$ (Barclay et al., 2015).

Given the inconclusive constraint on e and ω, and the BIC favouring a non-eccentric orbit, we decided to fit the transit model separately, and assume a circular orbit.

3.5.2 Transit Fit

The prior values for the transit model parameters are given in Table 3.5. To account for potentially underestimated noise from this star as noted earlier an additional noise term σ_{LC} is added in quadrature to the formal uncertainties. Given the lack of information on eccentricity from the radial velocity fit at this time, we assumed a circular orbit ($e = 0$) for the transit fitting.

An additional prior that can be applied due to the asteroseismic nature of the host star is a prior on stellar density (see Chapter 1 for more detail on such synergies). The average large frequency separation $\Delta\nu$ scales to good approximation with the square-root of mean stellar density (Tassoul, 1980; Ulrich, 1986), i.e.,

$$\frac{\Delta\nu}{\Delta\nu_\odot} \simeq \left(\frac{M}{\mathrm{M}_\odot}\right)^{0.5} \left(\frac{R}{\mathrm{R}_\odot}\right)^{-1.5} \simeq \sqrt{\frac{\rho}{\rho_\odot}}. \tag{3.5}$$

The mean stellar density can also be estimated from the lightcurve using Eq 30 of Winn (2010),

$$\rho_\star \approx \frac{3\pi}{GP^2}\left(\frac{a}{R_\star}\right). \tag{3.6}$$

Table 3.5: Model parameters and priors for the transit fit. Gaussian priors indicated by$N$(mean,standard deviation, and uniform priors by U(lower bound, upper bound). All logarithmic priors are in base 10.

Parameter	Prior
P	$U(42.2, 42.4)$ (days)
$\log R_{\rm p}/R_\star$	$U(-3, -1)$
$\log a/R_\star$	$U(0, 2)$
T_0	$U(133.5, 134.5)$ (BKJD)
b	$U(0, 1)$
$\rho_\star$	$N(9.19, 1.04)$ (kg/m^3)
σ_{lc}	$U(0, 500)$ (ppm)

Table 3.6: Value values for the transit fit, taking the median value as parameter, and 68% credible interval as uncertainties. In the fit e has been fixed to 0. The large value of σ_{lc} indicates the formal flux uncertainties are underestimated, most likely due to correlated noise.

Parameter	Result
P (days)	$42.296^{+0.001}_{-0.002}$
$R_{\rm p}/R_\star$	$0.0156^{+0.0006}_{-0.0007}$
$a/R_\star$	$9.51^{+0.36}_{-0.39}$
T_0 (BKJD)	$133.89^{+0.02}_{-0.02}$
i°	$85.1^{+0.4}_{-0.3}$
σ_{lc} (ppm)	316^{+1}_{-1}

During the fitting, the stellar density at each iteration was constructed using Eq 3.6, and the asteroseismic density used as a Gaussian prior.

The final values for the transit fit are given in Table 3.6. The large value of σ_{lc} reflects that KOI-6194 is a noisy star, due to it's evolved nature. Figure 3.4 shows the correlations between the different model parameters, with only i and $a/R_\star$ showing significant correlation. This is expected as either a change in i or $a/R_\star$ can change the transit duration (see Eq 1.4).

Using the fractional depth and the asteroseismic stellar radius, the radius of the planet can inferred to be $R_P = 0.88 \pm 0.04 {\rm R_J}$. In the next section we discuss the implications for this system.

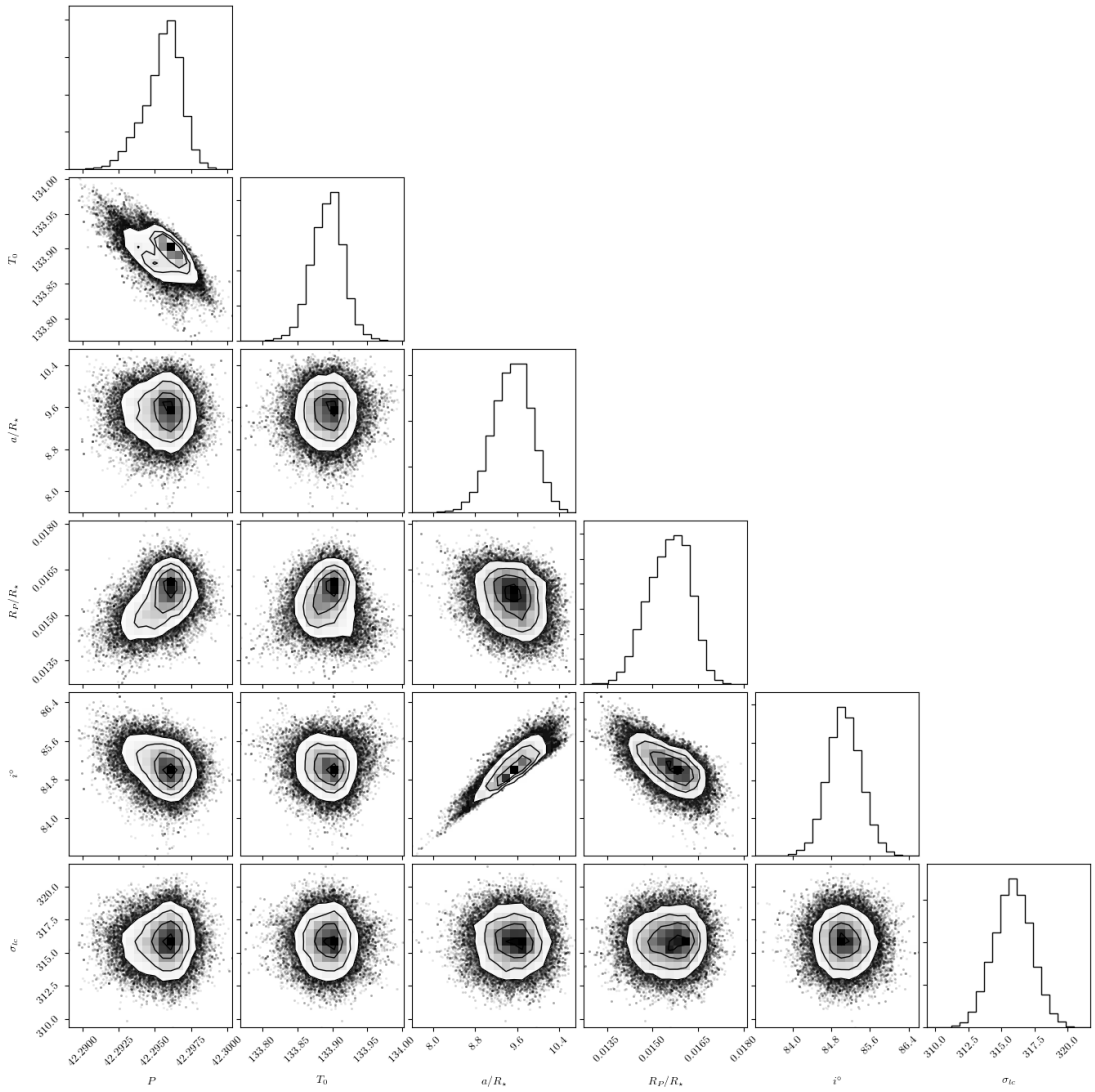

Figure 3.4: 2D histograms of samples from the MCMC transit fit, showing correlations between parameters. Only $a/R_\star$ and i° show significant correlation. This is due to relation between impact parameter b and $a/R_\star$

.

3.6 Discussion

KOI-6194 potentially represents another evolved system with few contemporaries, Kepler-56 (Huber et al., 2013a; Otor et al., 2016) being the poster-child of the class. Another well studied system is Kepler-91 (Barclay et al., 2015; Lillo-Box et al., 2014a). Fig 3.5 shows the distribution in stellar $\log g$ and orbital period P space, of planets around evolved hosts ($\log g \leq 3.5$). KOI-6194 is indicated as a blue star,

with the other transiting systems shown as red crosses. The plot shows that most planets detected around evolved stars are on long period orbits were detected by radial velocity surveys (black crosses). However there are several factors involved in this, one is the radial velocity surveys sample stars infrequently, allowing short period planets to slip through the gaps. A second factor is that, as noted above, that giant stars are subject to jiiter. If the size of this jitter signal is comparable to the size of the induced radial velocity amplitude, then the planet signal could be lost in the noise. A final factor is shown in the figure, the diagonal lines indicating the semi major axis a of a hypothetical planet as a factor of the stellar radius $R_\star$ for an assumed stellar mass of $M = 1.2\mathrm{M}_\odot$. Short period planets can only exist around relatively unevolved giants for the simple reason they would be inside the star further up the giant branch. This is without the additional incorporation of tidal effects increasing as the star expands, which may cause the planet to spiral inwards to the star (Schlaufman & Winn, 2013; Veras, 2016).

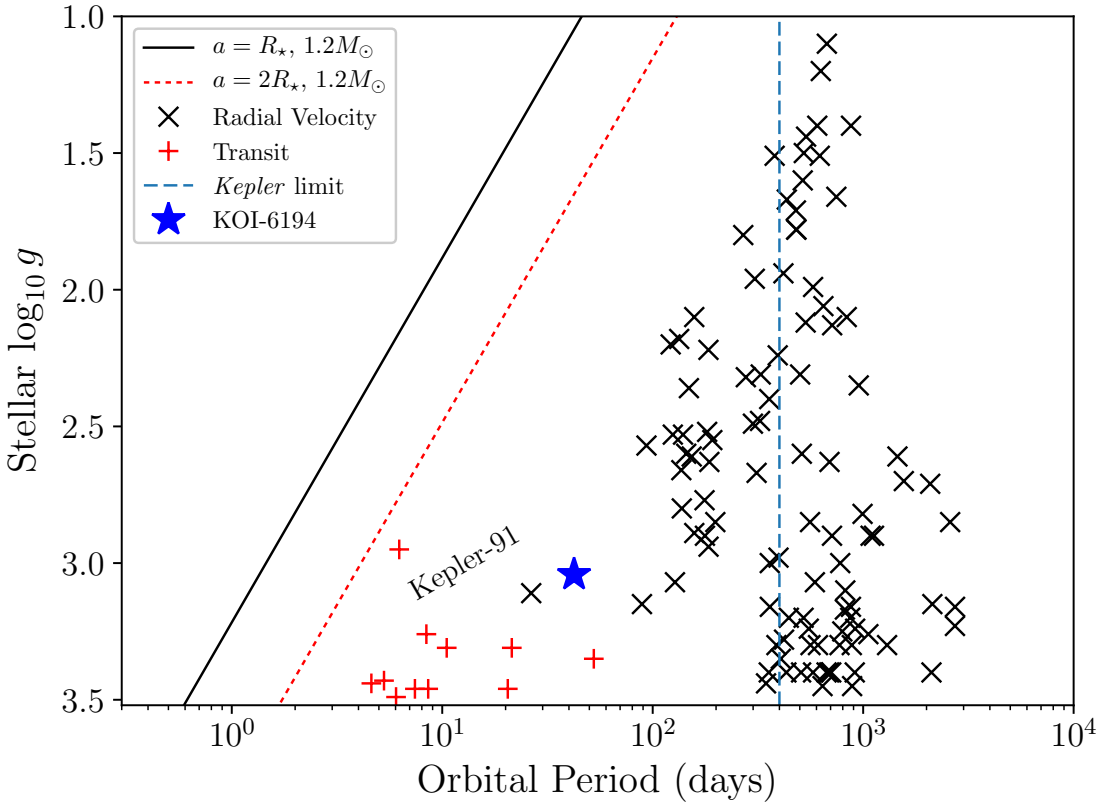

Figure 3.5: From the NASA Exoplanet Catalog (Akeson et al., 2013a), the reported planet period, against the stellar $\log g$, showing the paucity of short period planets detected by radial velocity observations around evolved stars. The diagonal lines represent the orbital radius a and a fraction of stellar radius $R_\star$, for $a = R_\star$ and $a = 2R_\star$. Only Kepler-91 is a more evolved transiting host.

3.6.1 Orbital solution

KOI-6194 is still a planet candidate, rather than a confirmed planet. Additional radial velocity observations are required to fully constrain the orbital eccentricity, along with a correlated noise model being implemented during the transit fit to fully account for the true noise levels. The large value of $\sigma_{\rm LC}$ Table 3.6 show that the uncertainties reported underestimate the true noise level.

3.6.1.1 Potential (re)-inflation?

Since the first detection of transiting planets (Charbonneau et al., 2000), giant planets in close proximity to their hosts have been shown to possess anomalously high radii. It has been shown that a planetary mass object, acting only under self-

gravitation, should not exceed $1.2R_J$ (Fortney et al., 2007) at an age of several billion years. To account for the inflated radii of these giant planets, additional energy has to be deposited inside the gaseous envelope of these planets. The energy source is presumed to be host star, and there does appear to be a correlation between current incident flux and measured planetary radius.

Recent discoveries of hot Jupiters in orbiting evolved stars (Lopez & Fortney, 2016; Grunblatt et al., 2016, 2017) has introduced the concept of "re-inflating" planets when the star evolves off the main sequence and the incident flux on the planet increases significantly. Many theories have been proposed to explain planetary inflation, one theory is that if a significant fraction of the incident energy can be transported into the deep layers of planets atmosphere and then deposited, the associated heating would produce radial inflation. The modest radius of KOI 6194 ($R_P = 0.88 \pm 0.04 R_J$) suggests that at this time, there is no significant inflation occurring for this system.

3.6.1.2 Future of the system

Assuming the detected signals are indicative of a bona fide planet, we can explore the potential future evolution of the system. In a similar vein to Chapter 2, KOI-6194 can be considered a "retired F star", at $M \approx 1.35 M_\odot$. At the current orbital separation of 0.26 ± 0.01AU, the planet will be ingested during the ascent of the star up the RGB. If no tidal decay of the orbit occurs before ingestion, the models used in Sec 3.4 suggest the star will reach a radius of 0.26AU in ∼140Myrs. Such a timescale is relatively short, when compared the lifetime of the host star ($10 \times 10^9 - 10 \times 10^{10}$yrs). As the star continues to expand, and ascend the RGB, the incident flux on the planet will rise rapidly, raising the temperature of the planet significantly. This may trigger mass loss from the planet, as the atmosphere is slowly stripped from it. Should the planet survive plunging into the star, the future of this system may resemble Kepler-70, an sdB star orbited by two transiting planets (Charpinet et al., 2011). The two orbiting sub-Earth mass planets are believed to be the remnants of

the giant planet cores, with the rest of the planetary mass being removed during the ingestion of the planet. The ingestion of giant planets has also been suggested as the source of lithium for giant stars exhibiting high lithium abundances (Adamów et al., 2012b; Jofré et al., 2015b).

At this point we move on to discuss another interesting system, KOI-3890.

3.7 Eclipsing binary system KOI-3890

During the initial identification of KOI-6194 (discussed in Sec 3.1.1) as a potentially interesting system, the planet candidate KOI-3890 was also identified, and scheduled for observations with TRES. The potential binary star nature of this system was first suggested in Lillo-Box et al. (2015), who collected 22 radial velocities using the CAFE spectrograph (Aceituno et al., 2013). While the phase coverage in Lillo-Box et al. (2015) is limited, the authors place constraints on the minimum eccentricity $e \geq 0.33$ and minimum radial velocity amplitude $K \geq 2.5\mathrm{kms}^{-1}$, which is equivalent to a required minimum companion mass of $M > 0.0097 \pm 0.0014\mathrm{M}_{\odot}$. This minimum mass is equivalent to $M > 10.2\mathrm{M}_{\mathrm{J}}$, and whilst this theoretically allows for a planet mass object ($M \lesssim 13\mathrm{M}_{\mathrm{J}}$), it does make the system more likely to be a binary star system.

Since the primary star is a red giant, it can be expected to display solar-like oscillations, as indeed it does. Binary stars of which one component is an asteroseismic star are relatively rare (Gaulme et al., 2013; Miglio et al., 2014; Gaulme et al., 2016). Such systems, with either one or two seismic components are excellent testbeds for asteroseismic scaling relations, such as Eq 1.19 and 1.20. If the system has observed radial velocity measurements for each component (a double-lined binary) and eclipses are observed, then the masses and radii can be measured independent of asteroseismology (and then compared to asteroseismic estimates). In the case of KOI-3890, it is a single line binary, therefore the dynamical mass cannot be estimated independent of the asteroseismic mass (see Sec 3.8.2).

3.8 Observations

KOI-3890 (KIC 8564976) was observed near-continuously for the 4 year duration of the *Kepler* mission in long cadence (∼30 minutes) mode. *Kepler* detected a transit-like feature at a period of 152.8 days, and the system was flagged as a KOI. No additional signals were detected.

3.8.1 Transits

Due to safe events, or gaps between quarters of data, some transits are missing. In Figure 3.6 two of the 10 potentially visible transits during the *Kepler* mission are shown to be missing or only partially observed due to falling in data gaps between quarters. The lightcurve was detrended in the same fashion as KOI-6194, using a 30 day moving median.

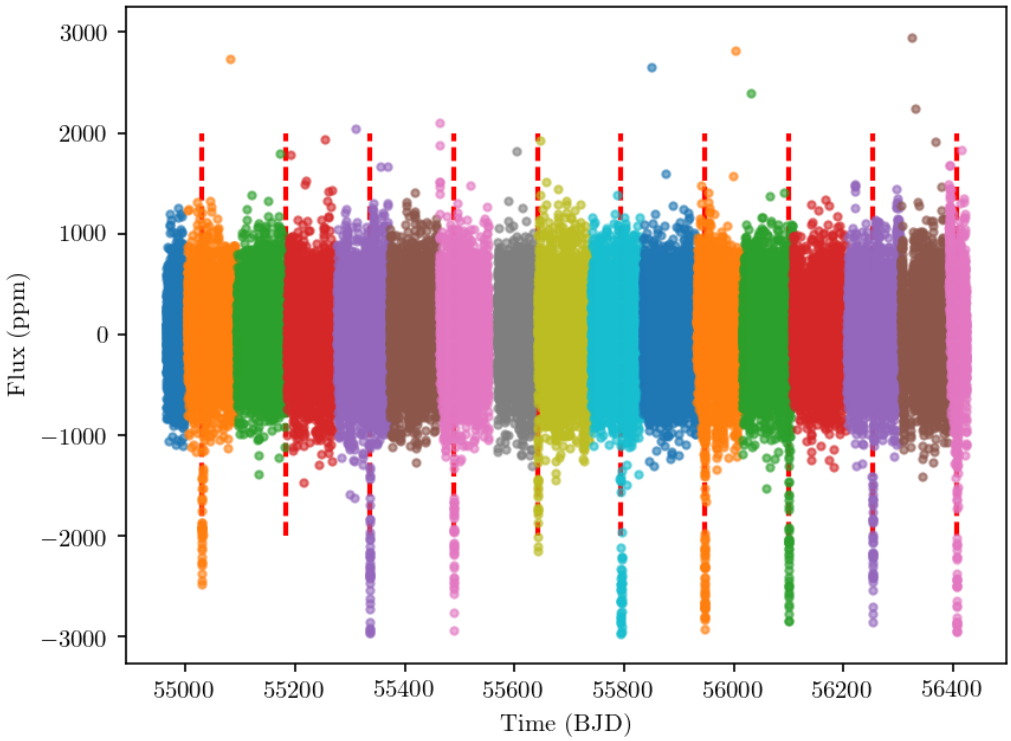

Figure 3.6: Detrended lightcurve of KOI-3890, showing strong transits. Different colours indicate different quarters of data. The vertical red dashed lines indicate the period of the orbit, and as such the location of expected transits. The second transit that should have been observed falls in the gap between Q3 (green) and Q4 (red). The transit at the start of Q9 (yellow) is only partially observed.

If the lightcurve is folded on the period found by the BLS algorithm, it is clear there is additional out of transit variability near to the time of transit. This will be discussed in more detail in Sec 3.10. Figure 3.7 shows this. For the subsequent fitting to the transit in Section 3.10, only phases in the folded lightcurve of $0.2 < \phi < 0.2$ were retained. The partially observed transits and surrounding data were removed from the lightcurve. No secondary transits are detected due to reasons detailed in Sec 3.12.

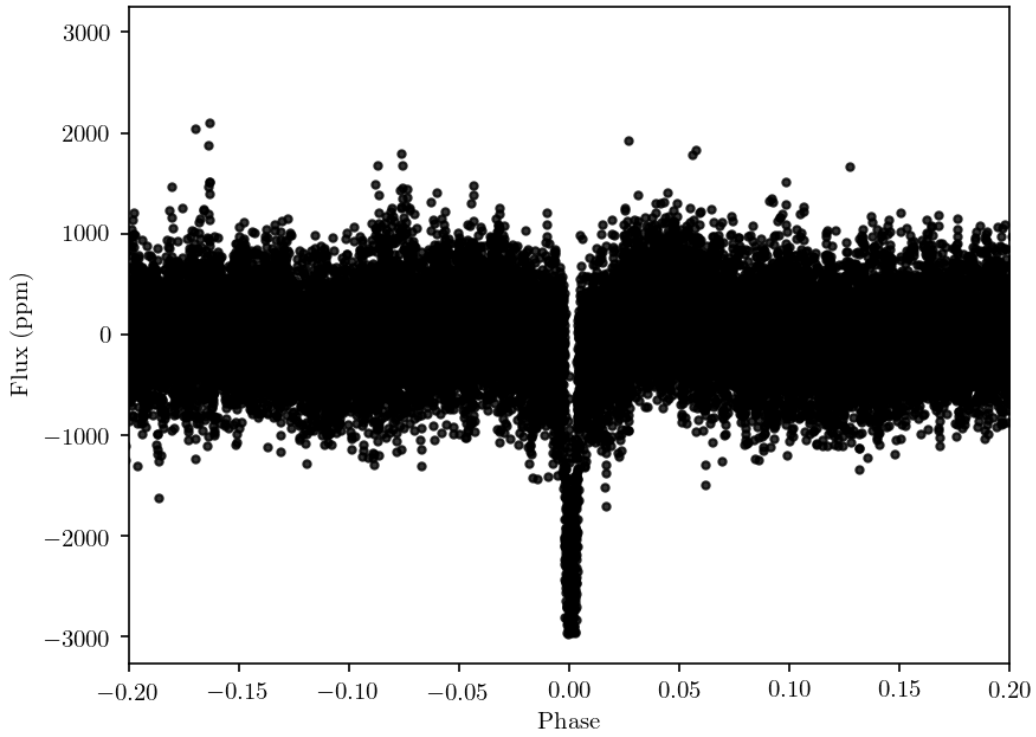

Figure 3.7: KOI-3890 lightcurve phase-folded on the orbital period determined from the BLS search, where to aid viewing the transit, I have limited the plot in phase to ±0.2. Near the transit, there is some form of additional variability.

3.8.2 Radial Velocity

KOI-3890 was observed using the TRES spectrograph (Szentgyorgyi & Furész, 2007) with 10 measurementsbeing taken. The CAFE radial velocity data of Lillo-Box et al. (2015) were also incorporated during the fitting of a model to the data.

3.9 Recovery of Stellar Properties

The collected spectra from which the radial velocities were calculated were also used to derive updated spectroscopic parameters for the system. Since the star has detectable solar-like oscillations, the asteroseismic $\log g$ was included as a constraint in the fit for the spectroscopic parameters.

Using the same methodology as described above for KOI-6194, the asteroseis-

Table 3.7: Stellar asteroseismic and spectroscopic parameters and the recovered fundamental stellar properties from PARAM, quoted uncertainties are the 68% credible interval for mass, radius and age.

KOI-3890A	
$\nu_{\rm max}$ (μHz)	104.3± 0.3
$\Delta\nu$ (μHz)	9.57±0.21
$\Delta\Pi$ (s)	77.6 ± 0.8
$T_{\rm eff}$ (K)	4726 ± 79
[Fe/H] (dex)	-0.13 ± 0.1
$M_\star$ ($M_\odot$)	$1.03^{+0.06}_{-0.06}$
$R_\star$ ($R_\odot$)	$5.75^{+0.15}_{-0.17}$
Age (Gyr)	$9.05^{+2.35}_{-1.66}$

mic global parameters $\nu_{\rm max}$ and $\Delta\nu$ were extracted from the power spectrum (see Chapter 1 for more detail). These results are provided in Table 3.7 along with the spectroscopic parameters and final stellar properties, again using PARAM.

In addition to $\nu_{\rm max}$ and $\Delta\nu$, the period spacing of the star was also used in the recovery of the stellar parameters. This was provided using the method of Hekker et al. (2017).

3.9.1 Stellar inclination angle and obliquity

Using the same methodology as described in Sec 3.3.2, the stellar inclination angle and the obliquity were recovered. For KOI-3890 $i = 87.6^{\circ+2.4}_{-1.2}$, and the obliquity $\phi(^\circ) = 3.9^{+2.1}_{-3.9}$, again consistent with alignment.

3.10 Lightcurve and Radial Velocity Modelling

As with KOI-6194, the transit and radial velocity data for KOI-3890 need to be modelled simultaneously. Using the asteroseismic mass from Table 3.7 and a preliminary fit to only the TRES radial velocity data indicated that the system was comprised of two stars in an eclipsing binary, with the primary a red giant of approximately solar mass, and the secondary an M dwarf of approximate mass $M = 0.25 M_\odot$. Whilst this suggests that the secondary is a self-luminous body, the relative flux contribution

is minimal. The luminosity of the primary is $L \approx 15\mathrm{L}_{\odot}$ using the values in Table 3.7, while the secondary has $L \lesssim 0.05\mathrm{L}_{\odot}$ (assuming $R = 0.25\mathrm{R}_{\odot}, T_{\mathrm{eff}} = 3000\mathrm{K}$ see Kaltenegger & Traub 2009), a factor of ∼3000 less in brightness. This means that the eclipses can be considered as transits, in terms of modelling. The initial fit to the TRES radial velocity data also indicated the orbit was highly eccentric, with the eclipses being observed near periastron. For the final fitting, the TRES data were combined with the CAFE radial velocities from Lillo-Box et al. (2015), with an additional parameter included in the fit to account for zero-point offset between the data sets. The CAFE data were included to increase phase coverage of the orbit, as well as trebling the available radial velocity measurements (32 total, 22 CAFE, 10 TRES).

3.10.1 Tidal distortion of primary

Figure 3.7 shows the phase folded lightcurve around the time of mid-transit. it also shows that just outside of transit, there is additional flux variation. As discussed above, the flux contribution from the secondary component is negligible. It can therefore be assumed that the flux variation is originating from the primary (giant) star.

This additional flux variation is believed to be indicative of a heartbeat star, a rare type of tidally induced variation (Welsh et al., 2011; Thompson et al., 2012; Beck et al., 2014; Shporer et al., 2016). For circular orbits ($e = 0$), this tidal effect is constant, raising a bulge on the primary star. In this case, it is known as ellipsoidal variation. For eccentric orbits, the term "heartbeat" reflects the passing visual similarity of the tidally induced variation to an echocardiogram.

The heartbeat is induced as the tidal effects (and so distortions) are greatest near periastron. Whilst most heartbeat stars are at relatively modest periods ($P \leq$ 100days), the evolved nature of the primary star means that at periastron passage, the separation between the stars is only a few times the primary radius, and so the

secondary is able to raise a tidal bulge on the star.

The heartbeat flux modulation was modelled following the prescription given in Kumar et al. (1995),

$$\frac{\delta F}{F} = S \cdot \frac{1 - 3\sin^2(i)\cos^2(f(t) - \omega)}{(R(t)/a)^3}. \tag{3.7}$$

In Eq 3.7, S is the amplitude of the fractional flux variation, i the system inclination angle (known to be $i \sim 90^\circ$ since eclipse is observed), $f(t)$ is the true anomaly, ω the argument of periastron, and $R(t)/a$ the distance between the two stars as a fraction of the semi-major axis a, as a function of time. $R(t)/a$ can also be expressed as (Eq 1 Winn 2010),

$$\frac{R(t)}{a} = \frac{1 - e^2}{1 + e\cos(f(t))}. \tag{3.8}$$

Eq 3.7 and 3.8 combined introduce only one new parameter S, the fractional amplitude of the heartbeat modulation, with all other parameters already included within the transit or radial velocity models.

While the model appears relatively simple, it can produce a wide variety of possible lightcurve modulation, due to the possible orientations of the system in i and ω. See Figure 8 of Thompson et al. (2012) for a range of possible heartbeat signals. This flexibility is ideal for systems of unknown inclination. In the case of KOI-3890, the presence of eclipses indicates the system is close to edge-on orientation already ($i^\circ \sim 90$). The tidal model was added to the transit model during the simultaneous fit. The results are discussed below.

As with KOI-6194, the mean stellar density from asteroseismology was also used as a prior during the fitting procedure.

3.11 Results

The priors used during the fit are given in Table 3.8. The results of the combined transit, tidal and radial velocity fit are given in Table 3.9. Figure 3.8 shows the final

Table 3.8: Model parameters and priors for the simultaneous fit. Gaussian priors indicated by$N$(mean,standard deviation, and uniform priors by U(lower bound, upper bound). All logarithmic priors are in base 10.

Parameter	Prior
P	$U(151, 153)$ (days)
$\log(R_2/R_\star)$	$U(-3, -1)$
$\log(a/R_\star)$	$U(0, 2)$
T_0	$U(55025, 55035)$ (BJD)
b	$U(0, 1)$
$e\cos\omega$	$U(-1, 1)$
$e\sin\omega$	$U(-1, 1)$
$\gamma_{\rm TRES}$	$U(-100, 100)$ (km/s)
$\gamma_{\rm CAFE}$	$U(-100, 100)$ (km/s)
$\log(K)$	$U(-1, 2)$ (km/s)
$\sigma_{\rm RV,TRES}$	$U(0, 10)$ (km/s)
$\sigma_{\rm RV,CAFE}$	$U(0, 10)$ (km/s)
S	$U(-100, -100)$ (ppm)
$\rho_\star$	$N(7.09, 0.31)$ (kg/m^3)

fit of the model to the data, phase folded on the period of the orbit and centred around time of mid transit, with the transit and tidal models shown. The lower panel shows the radial velocity model with the TRES and CAFE data plotted in separate colours. Typical errors on the radial velocity measurements are $\sim$40ms^{-1} for TRES and $\sim$80ms^{-1} for CAFE.

Table 3.9: Model parameters median values from the fit, and associated uncertainties.

Parameter	Median Value
P	152.826 ± 0.0002 (days)
$R_2/R_\star$	0.0444 ± 0.0002
$a/R_\star$	20.44 ± 0.28
T_0	55030.411 ± 0.001 (BJD)
i°	85.3 ± 0.2 (deg)
e	0.645 ± 0.001
ω°	108.7 ± 0.02 (deg)
$\gamma_{\rm TRES}$	3.96 ± 0.20 (km/s)
$\gamma_{\rm CAFE}$	-30.6 ± 0.13 (km/s)
K	10.1 ± 0.3 (km/s)
$\sigma_{\rm RV,TRES}$	0.53 ± 0.16 (km/s)
$\sigma_{\rm RV,CAFE}$	0.14 ± 0.03 (km/s)
S	-12.0 ± 0.1 (ppm)

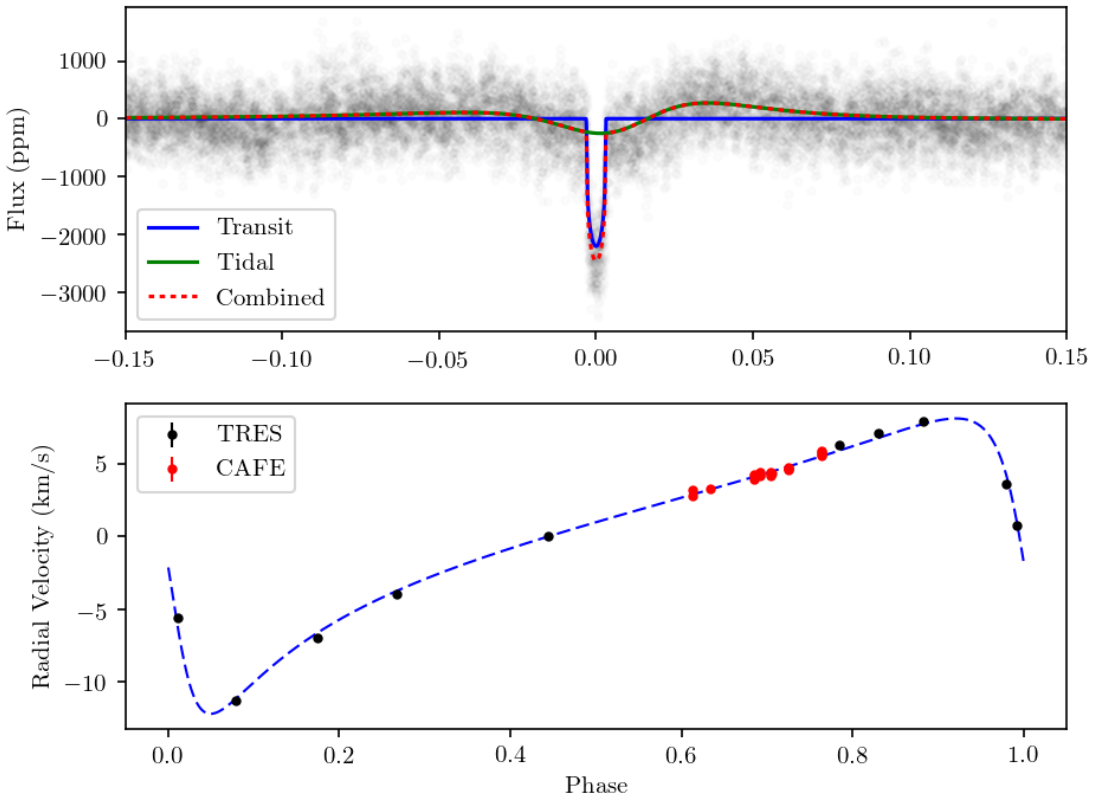

Figure 3.8: Phase folded final fit centred around time of mid transit. In the upper panel, the lightcurve is in black, with the final model shown in red. The two components of the lightcurve model are also shown, the transit in blue, and the tidal model in green. In the lower panel the TRES radial velocity data (black) and CAFE data (red) are shown phase folded and also centred around mid transit, with the final model shown as dashed blue.

Table 3.10: Derived mass and radius for the secondary from the fit and the asteroseismic mass and radius of the primary. Both mass and radius of the secondary are consistent with an M dwarf.

KOI-3890B	
M_2 ($M_\odot$)	0.228 ± 0.011
R_2 ($R_\odot$)	0.256 ± 0.007

As the upper panel of Fig 3.8 shows the tidal distortion of the primary boosts the transit depth of the secondary if not accounted for. This would indicate a larger radius than otherwise expected if the calculated radius was compared to a predicted radius from the calculated secondary mass. The secondary mass was calculated by numerically solving Eq 3.4, and the derived mass and radius of the secondary are given in Table 3.10.

3.12 Discussion

KOI-3890 represents an intriguing system captured during a period of rapid evolution. As the primary star continues to ascend the red giant branch, the tidal forces between the two components will continue to grow and the heartbeat signal will grow.

The lack of secondary eclipses (secondary behind primary from observer perspective) is due to the inclination and eccentric nature of the system. The impact parameter b for transiting or occulting objects is given in Winn (2010, Eq 7,8),

$$b = \frac{a\cos(i)}{R_\star}\left(\frac{(1-e^2}{1 \pm e\sin\omega}\right), \tag{3.9}$$

where transits are (+) and occultations (-). For KOI-3890, the transit impact parameter $b_{\rm tran} = 0.602 \pm 0.015$, however for the occultation $b_{\rm occ} = 2.49 \pm 0.06$. As such the M dwarf does not pass behind the primary during its orbit, and so no secondary is observed, since $b \leq 1$ is required for a transit or occultation to occur.

3.12.1 Potential future evolution of system

As an eccentric binary around an expanding red giant, it is interesting to explore the potential future evolution of the system. As the primary continues to evolve up the red giant branch, the models used above in Sec 3.4 predict a $\sim$1M$_\odot$ star reaches a radius of $\sim$160R$_\odot$ (0.75AU) at the tip of the red giant branch. The current separation of the two stars at periastron is $R_{\rm peri} = 7.25 \pm 0.10 {\rm R}_\star$, or 0.19 ± 0.01AU, and as such the two stars will meet during the ascent of the giant branch, rapidly evolving into a common envelope phase.

What configuration the orbit of the secondary will be in is determined by the rate of tidal circularization for the system. If the rate is high, then the orbital energy (and momentum) of the M dwarf will be dissipated in the deep convective zone of the primary, and the orbital eccentricity will be dissipated. To estimate the tidal circularization timescale, we used Eq 16 of Claret et al. (1995), which estimates the circularization timescale for stars with a convective envelope i.e.,

$$\tau_{\rm circ} = (1.99 \times 10^3 {\rm yr}) M^3 \frac{(1+q)^{5/3}}{q} L^{-1/3} \lambda_2^{-1} \frac{P^{16/3}({\rm days})}{R^{22/3}} \tag{3.10}$$

In the above equation M, R and L are the total stellar mass, radius and luminosity in solar units, q is the mass ratio of the components ($M_\star/M_2$). λ is known as the tidal constant and is related to the internal structure of the star. We take representative values from Claret et al. (1995) (see Fig 3) of $\lambda_2 = 0.006$. Here we are also ignoring additional effects on the tidal evolution of the system.

Assuming P has remained constant throughout the history of the system, (a reasonable assumption due to the orbital period- the two stars have only recently begun interacting), $\tau_{\rm circ}$ during the main sequence lifetime would have been far greater than the expected main sequence lifetime ($\tau_{\rm circ} \approx 2 \times 10^{17}$yr), where we have estimated the main sequence luminosity and radius using the relations $L \propto M^{3.9}$ and $R \propto M^{0.8}$, taking M from Table 3.7, thus neglecting any mass loss throughout

the star's lifetime thus far.

As the primary ascends the red giant branch, $\tau_{\rm circ}$ will dramatically decrease, due to the strong dependence on R (and to a less extent, the dependence on L). At the present epoch $\tau_{\rm circ} \sim 900$Gyr. Only when the system is significantly more evolved does the radius dependence overcome the period dependence of Eq 3.10. For instance, assuming P does not vary before $R_\star = R_{\rm peri}$ then $\tau_{\rm circ} \sim 2 \times 10^5$yr when the stars come into contact.

The further evolution of the system is unknown but speculative further evolution is detailed here. As the primary continues to evolve the M dwarf may become embedded in the expanding envelope, leading to mass transfer between the stars, in a common envelope phase. Additionally the strong drag forces on the secondary in such a configuration may lead to the ejection of the common envelope, and a significant decrease in the orbital period of the secondary. Since the M dwarf will encounter the expanding envelope before the primary has reached the tip of the RGB, the primary will not have gone through the helium flash (see Chapter 1). In the event that the common envelope is ejected, the helium core may be exposed as a sdB star, and the binary left in a close orbit, thus providing a mechanism for the formation of sdB stars. If the drag on the M dwarf is sufficient before the ejection of the envelope, the red giant core and the M dwarf could collide or merge inside the common envelope.

3.13 Conclusion

In this chapter we have discussed two systems of interest with asteroseismic primary stars. KOI-6194, a potential giant planet orbiting a red giant star, a particularly rare class of planet. Whilst the current radial velocity observations are unable to fully constrain the shape of the orbit, both an eccentric and circular orbital model are consistent with a signal $K < 45$ms^{-1}, which when combined with the stellar mass determined through the use of asteroseismology indicates a planetary mass of

$M_P < 0.9^{+0.1}_{-0.1}\mathrm{M_J}$. Combined with a radius of $R_P = 0.88 \pm 0.04\mathrm{R_J}$, this suggests this planet is not significantly influenced by re-inflation at this time. Additional radial velocity observations are planned to fully parameterise this system.

The other discussed system, KOI-3890 is an eclipsing binary system composed of a red giant primary and a M dwarf secondary that is inducing tidal distortions in the primary star. This system will ultimately undergo a common envelope phase, before the primary reaches the tip of the RGB or the helium flash. In the event that the two stars do not fully merge, the common envelope may be ejected to reveal an sdB orbited by the M-dwarf on a much shorter orbital period.

4 Comparative Spectroscopic Analysis

The text in this chapter is presented in a format similar to a manuscript currently in preparation. I will be first author on this work. The data were collected by the Stellar Observations Network Group (SONG) telescope, first results presented in Grundahl et al. (2017). Further information on SONG is presented in Grundahl et al. (2011). The telescope time was awarded after application and assessment by the SONG TAC. The results presented here are based on observations made with the Hertzsprung SONG telescope operated on the island of Tenerife by the Aarhus and Copenhagen Universities in the Spanish Observatorio del Teide of the Instituto de Astrofsica de Canarias. The spectral analysis with the ARES and MOOG codes was performed by Sérgio Sousa, and the SONG observations and calibration provided by Frank Grundahl..

4.1 Introduction

The accurate and precise measurement of stellar and planetary parameters is critical to understanding a vast range of astrophysical problems, from star and planet formation (Gaudi et al., 2005), through the co-evolution of a planetary system, until its final demise (Huber et al., 2013a; Schröder & Connon Smith, 2008). With thousands of exoplanets (Borucki et al., 2010; Fischer et al., 2014) now discovered, several key features have been found in the distribution of exoplanets and exoplanet hosts. A key discovery is the apparent positive correlation of giant planet occurrence rate with stellar metallicity for planets around dwarf stars (Fischer & Valenti, 2005). Additionally there is evidence of the same correlation for subgiant stars (Johnson

et al., 2010b). There is also evidence of correlation with stellar mass (Johnson et al., 2007b) for dwarf stars. This correlation is believed to indicate that giant planets form via core accretion, rather than direct collapse. This is because core accretion requires the formation of dust grains etc that can aggregate to form the initial planetesimal-this in turn requires elements heavier than hydrogen and helium to achieve. Direct collapse does not require this step. If direct collapse was the primary formation pathway for giant planets, there would be no observed correlation with stellar metallicity.

The existence of such correlations between giant plant occurrence and stellar mass or metallicity for giant stars is more contentious. Reffert et al. (2015) find an increase in occurrence rate for giant planets around giant stars, to a peak in stellar mass at $\sim 1.9\mathrm{M}_{\odot}$ and positive metallicity correlation. Maldonado et al. (2013) do not see a preferential metallicity enhancement in giant star planet hosts, however they do find a correlation of stellar mass and metallicity. Mortier et al. (2013) find no metallicity enhancement for red giant hosts ($\log g < 3$) compared to non-hosts. There are several possibilities to explain a lack of metallicity correlation for evolved stars. It is possible that any pre-existing planetary system has been consumed during the post main sequence evolution of the star. During the subgiant evolution of a star, as the star migrates towards the giant branch, surface convection zones develop in stars $M \lesssim 1.5\mathrm{M}_{\odot}$. Stars below this mass already possess surface convection. Significant convection zones allow for the angular momentum of the orbit to dissipate inside the star, causing the planet to inspiral and subsequently be disrupted (Schlaufman & Winn, 2013). The impact of such engulfment would be two fold. Firstly any radial velocity survey would fail to detect a planet around such a star and so would be identified as a non host. Thus any underlying true metallicity enhancement in planet hosts (or former hosts) would be smeared out due to former hosts now being identified as non hosts, and contributing to the metallcity distribution of non hosts. Second, during the ingestion of the planet,

metal rich material will be accreted by the star, the exact details dependent on the planet ingested. During the accretion phase this material would temporarily boost the observed stellar metallicity until it is significantly redistributed inside the star. In doing so it will change the observed metallicity of the star from the main sequence metallicity. Such effects have been seen in white dwarfs (Klein et al., 2010). Enhanced lithium content in the photospheres of giant stars has been taken by some as evidence of planet ingestion (Carlberg et al., 2010; Alcalá et al., 2011; Adamów et al., 2012a).

An additional reason for a different relation to metallicity is the impact of stellar mass. If we consider the masses of planet hosts detected by radial velocity measurements for giants and for dwarfs, we see that the giant sample is not simply the evolved counterpart of the dwarf sample. Figure 4.1 shows this. Using available stellar gravities and masses in the NASA Exoplanet Archive, histograms are plotted of the observed masses for 3 different populations: dwarfs ($\log g \geq 3.7$), subgiants ($3 < \log g < 3.8$) and giants ($\log g \leq 3$). The dwarf sample is centred around a solar mass star, while the more evolved samples are centred around higher masses.

One potential shortcoming of these results is that the data were collected from multiple spectrographs, each with different reduction pipelines. This was done for practical considerations, such as target observability and securing telescope time on a single telescope over multiple years. However we note that each sample will be subject to different systematics, making a direct like for like comparison difficult and potentially inaccurate.

In this paper we detail the results of a homogeneous spectroscopic survey of bright exoplanet hosts and field stars, undertaken using the Danish SONG (Stellar Observations Network Group) telescope. All observations were made from the first node of the network, at Observatorio del Teide, on Tenerife. We outline the structure of the paper below. In Section 4.2 we discuss the target selection utilised for the planet hosts and suitable comparison stars, while Section 4.3 details the

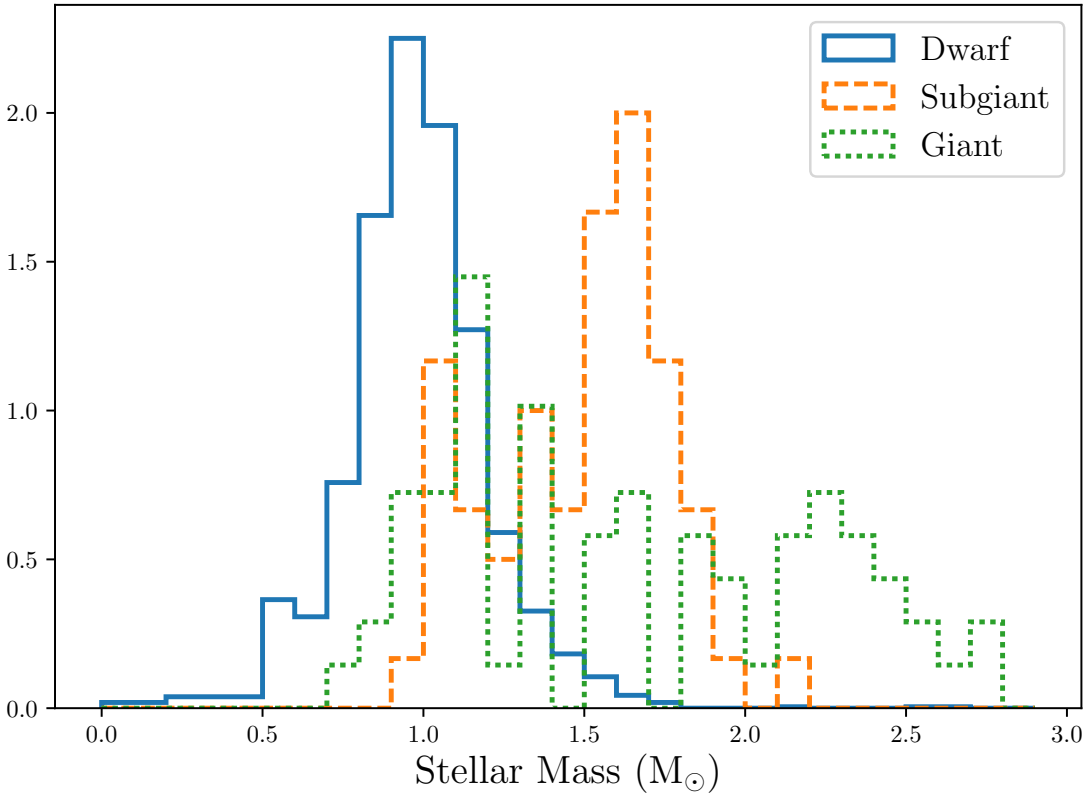

Figure 4.1: Using data from NASA Exoplanet Archive, distribution of observed masses for dwarf, subgiant, and giant star samples. The dwarf star sample is clearly centred around lower stellar mass, than the giant or subgiant populations.

observations made and how the spectra were analysed to yield the spectroscopic parameters. Section 4.5 discusses the results, and the derived stellar properties from these parameters, where we compare to other literature values, before we conclude in Section 4.6, and discuss the future application of asteroseismology to these targets.

4.2 Target selection

The SONG telescope location on Teide, Tenerife limits observations to declinations $\delta \gtrsim -38°$, however all right ascensions were accessible during the observing run (March 2016 to October 2017). Additionally, prior to March 2017, SONG spectroscopic targets were limited to magnitude $V < 6$. Exoplanet host targets were selected from the NASA Exoplanet Archive (Akeson et al., 2013a) subject to these constraints, where we retained the $V < 6$ constraint for all observing runs due to the long exposure lengths required at fainter magnitudes. Additionally we ensured only targets observed by radial velocity surveys were selected. The Exoplanet Archive also lists some brown dwarf systems as confirmed exoplanets, therefore systems with planetary masses above $13\mathrm{M_J}$ were also removed. Since sub giant and giant stars are of interest, only stars with $R_\star > 2\mathrm{R}_\odot$, and $T_{\rm eff} < 6500\mathrm{K}$ were retained, using stellar parameters derived from *Hipparcos* observations-see below for parameter estimation. This left 36 host stars (with planets in mass range $0.48 - 11\mathrm{M_J} \sin i$ for which to find suitable comparison stars.

For a valid sample of comparison stars, for each host, at least two independent comparison stars were selected from a consolidated list of many targets observed during longterm radial velocity surveys to ensure these stars did not host any known planets down to the detection limit of the survey they are drawn from. The field stars were drawn from various radial velocity surveys (Setiawan et al., 2004; Valenti & Fischer, 2005; Reffert et al., 2006; Johnson et al., 2007a; Takeda et al., 2008; Wittenmyer et al., 2011; Jones et al., 2011; Döllinger et al., 2011; Fischer et al., 2014). These stars were assumed to have been observed by the surveys they are

Table 4.1: Stars from each literature source for the 109 stars in the sample discussed in this work

Survey	N
Lick Giant Stars (Hekker & Meléndez, 2007; Reffert et al., 2015)	51
Okayama Planet Search Program (Takeda et al., 2008)	29
Tautenburg Observatory Planet Search Programme (Döllinger et al., 2007)	7
Jofré et al. (2015a)*	5
Bohyunsan Observatory Echelle Spectrograph (Lee et al., 2012, 2014)	5
ESO-FEROS (Setiawan et al., 2004)	3
EXPRESS (Jones et al., 2011)	3
Pan-Pacific Planet Search (Wittenmyer et al., 2011)	1
Lick Planet Survey (Fischer et al., 2014)⋆	5

* This work analyses 223 evolved stars with and without planets, drawing targets from Okayama Planet Search Program, (Takeda et al., 2008), Retired A Stars Program (Johnson et al., 2007a) and ESO FEROS planet program (Setiawan et al., 2004), not all of which have complete target lists publicly available.

⋆ Distinct from the giant star survey.

part of, with no planets detected around them. Table 4.1 presents the number of stars drawn from each survey.

To estimate the stellar parameters in a homogeneous fashion the parallax and photometry values of van Leeuwen (2007), along with the bolometric corrections of Torres (2010), were used to estimate stellar luminosities, temperatures and radii for all the survey stars and host stars. Comparison stars C were selected according to the following selection function based upon the host (subscript $X_{\rm H}$) color $(B-V)_{\rm H}$ and radius $R_{\rm H}$,

$$C = \begin{cases} (B-V)_{\rm H} \pm 0.4, R_{\rm H} \pm 3.5 & \text{if } R_{\rm H} > 20{\rm R}_{\odot} \\ (B-V)_{\rm H} \pm 0.25, R_{\rm H} \pm 0.8 & \text{otherwise.} \end{cases} \tag{4.1}$$

The larger $(B-V)$ selection for the stars higher up the RGB was required due to a lack of sufficiently bright survey stars. We assume the observed $(B-V)$ is intrinsic to the star, i.e. reddening is insignificant for these stars.

4.3 Observations and Spectral Analysis

All stars were observed using the 1m SONG telescope, at SNR$\sim$ 300, and resolution $\sim$90000, with wavelength calibration provided by ThAr spectra observed before and after the stellar spectra.

The spectroscopic stellar parameters ($T_{\rm eff}$, $\log g$ and [Fe/H]) were derived using a well established Equivalent Width (EW) method (Sousa et al., 2011) where the spectroscopic analysis is based on the EW measurements of FeI and FeII lines performed automatically with the ARES code (Sousa et al., 2007, 2015) and computing the individual iron abundances assuming LTE using the MOOG code (Sneden, 1973) in conjunction with a set of plane-parallel ATLAS9 model atmospheres (Kurucz, 1993). This methodology automates spectral analysis. A summary of the ARES process is included here, for full details on the ARES+MOOG method see Sousa (2014). Figure 4.2 (Fig 1 of Sousa 2014) summarises the entire ARES+MOOG workflow required.

- For an individual spectral absorption line at a known wavelength, the continuum level is estimated in the surrounding region in an automatic fashion.
- The spectral line of interest is fitted with a Gaussian and the area of the line below the defined continuum level is calculated.
- An Equivalent Width is the wavelength range required to produce the same area as the area of the Gaussian, centred around the central wavelength of the spectral line.
- This process is repeated for all the lines in the chosen line list. Since we are dealing with the analysis of cool stars meaning that we have spectra with stronger line blending, here we have used a specific list of iron lines proven to be more precise in cool stars (see. Tsantaki et al. 2013).

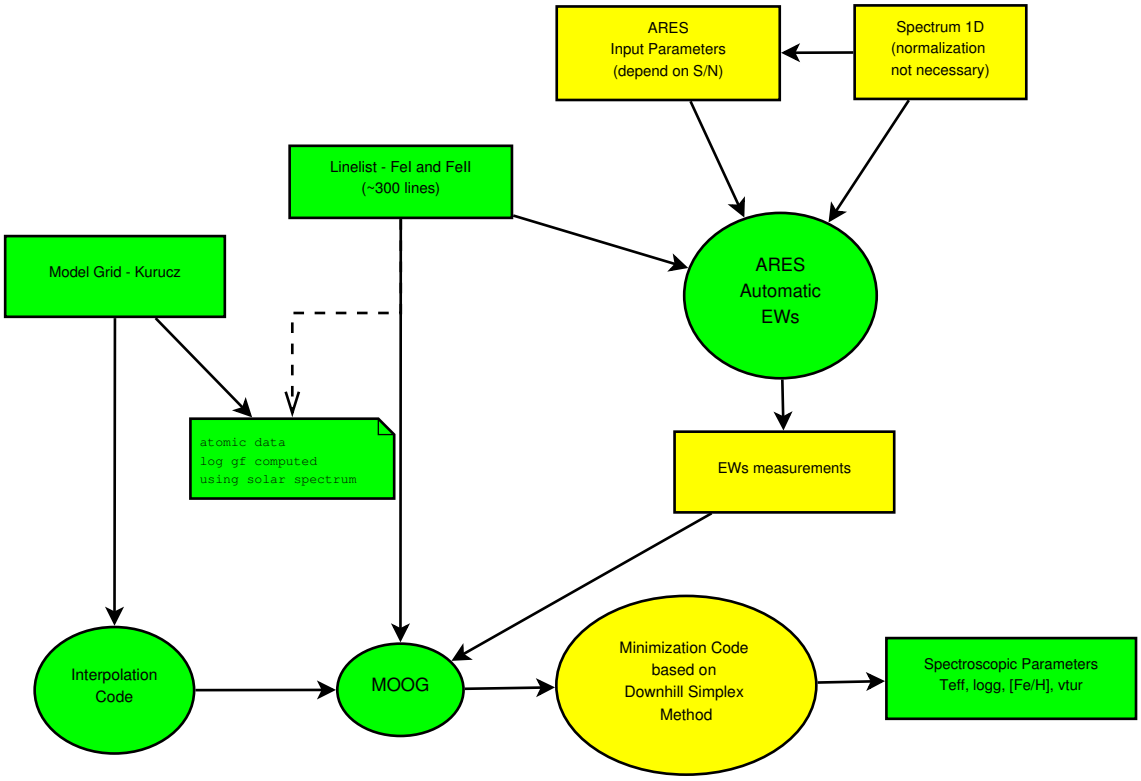

Figure 4.2: The entire ARES+MOOG workflow

Figure 4.3 (Fig 1 of Stetson & Pancino 2008) illustrates what an equivalent width is. The automation of the spectral analysis process decreases computation time, and removes the human element of determining the location of the continuum flux. Thus results from automated pipelines should be more reliable. At this point the the list of central wavelengths and EWs is input into MOOG, along with the chosen stellar model atmosphere. On a line by line basis, the individual iron abundances are calculated for the observed spectra and model spectra under the assumption of local thermodynamic equilibrium (LTE). This process is iterated varying the stellar atmosphere model parameters until each observed line provides the same abundance measurement, and the spectroscopic parameters of the final stellar model taken as the parameters for the observed star.

During this analysis, several spectroscopic binaries were identified as having been part of the field star target list, which were subsequently removed. There were also several M giant stars that are too cool for ARES+MOOG spectral analysis (as they

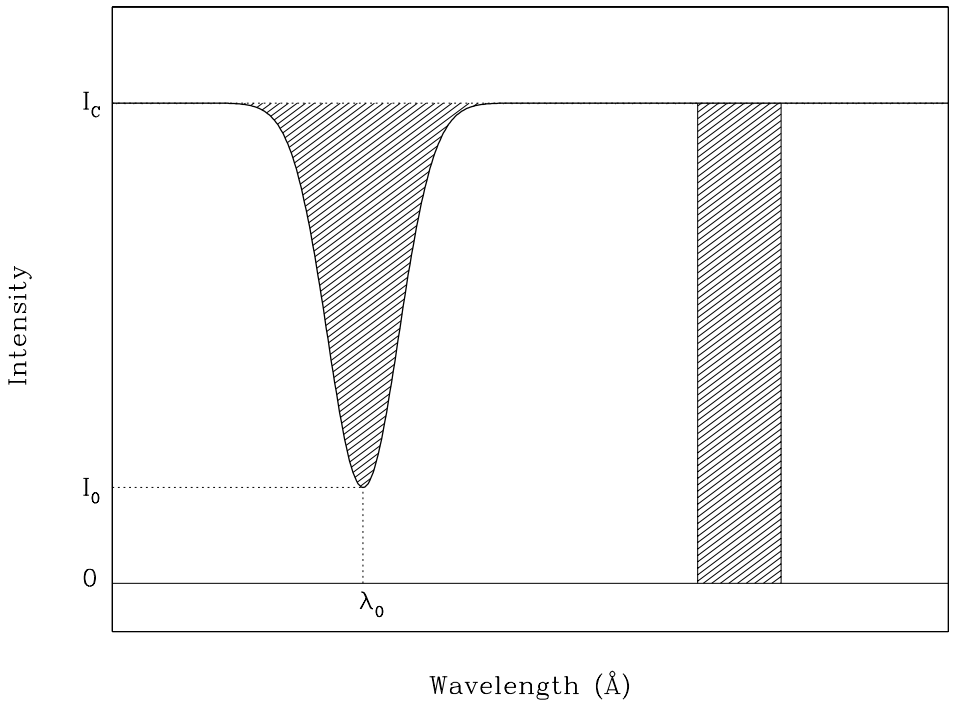

Figure 4.3: Graphical representation of an equivalent width. As can be seen, an EW will be sensitive to the placement of the continuum intensity I_c

no longer satisfy the assumption of LTE). These M giants were also removed from the sample. A stable spectroscopic solution was not recovered for a handful of stars. This left 73 field stars, together with 36 host stars.

4.4 Fundamental Stellar Properties

In addition to the updated spectroscopic parameters for these stars, we estimated the fundamental stellar properties using stellar models, in this case MESA models (Paxton et al., 2011, 2013) in conjunction with the Bayesian code PARAM (da Silva et al., 2006; Rodrigues et al., 2017). A summary of our selected "benchmark" options is as follows;

- Heavy element partition from Grevesse & Noels (1993).
- OPAL equation of state (Rogers & Nayfonov, 2002) along with OPAL opacities (Iglesias & Rogers, 1996), with complementary values at low temperatures

from Ferguson et al. (2005).

- Nuclear reaction rates from NACRE (Angulo et al., 1999).
- The atmosphere model is that according to Krishna Swamy (1966).
- Mixing length theory was used to describe convection (a solar-calibrated parameter $\alpha_{\rm MLT} = 1.9657$ was adopted).
- Convective overshooting on the main sequence was set to $\alpha_{\rm ov} = 0.2H_p$, with H_p the pressure scale height. Overshooting was applied according to the Maeder (1975) step function scheme.
- No rotational mixing or diffusion was included.

Compared to the grids used in Rodrigues et al. (2017), we extend the mass range to $5\mathrm{M}_{\odot}$.

Using these stellar models, we derived the fundamental stellar properties using the stellar effective temperature, gravity, metallicity and luminosity as constraints. For the luminosity constraint, the luminosity may be estimated as follows (e.g. see Pijpers 2003):

$$\log_{10}\frac{L}{L_{\odot}} \;=\; 4.0 \;+\; 0.4M_{\rm bol,\odot} \;-\; 2.0\log_{10}\pi[\mathrm{mas}] \;-\; 0.4(V \;+\; BC(V)). \quad (4.2)$$

Johnson V magnitudes and uncertainties were taken from the Tycho-2 catalog (Høg et al., 2000). The solar bolometric magnitude $M_{\rm bol,\odot} = 4.73$ is taken from Torres (2010), from which we also take the polynomial expression for the bolometric correction[1] $BC(V)$. Given the proximity and brightness of all stars in the sample, extinction for all stars was assumed to be zero.

[1]The polynomial bolometric corrections presented in Torres (2010), are reprints of values presented in Flower (1996), having been corrected for typographical errors in the original

4.4.1 Parallaxes

Parallaxes π were taken from *Hipparcos* (van Leeuwen, 2007). They were not taken from the recent Tycho-Gaia Astrometric Solution (TGAS) data release, part of the *Gaia* Data Release 1 (Lindegren et al., 2016). This was to maintain a homogeneous analysis for all stars, for which *Gaia* parallaxes are not all available. When Gaia DR2 is released (expected April 2018), updated parallaxes should be available for the stars in this sample.[2]

4.5 Results

In Table 4.2 we present the final results for the spectroscopic analysis and the derived stellar properties. We then discuss our spectroscopic results, compared to literature values.

Table 4.2: SONG spectroscopic $\log g$, [M/H] and $T_{\rm eff}$ parameters along with final stellar properties, including $\log g$ returned by models for comparison. Host stars indicated by * superscript

HIP	$\log g_{\rm SONG}$	[M/H]	$T_{\rm eff}$	L ($L_\odot$)	Mass ($M_\odot$)	Radius ($R_\odot$)	$\log g_{\rm PARAM}$
HIP840	2.91 ± 0.08	-0.1 ± 0.02	4849 ± 34	17.3 ± 1.1	$1.23^{+0.09}_{-0.08}$	$5.88^{+0.2}_{-0.19}$	$2.97^{+0.04}_{-0.04}$
HIP1708	2.48 ± 0.17	0.15 ± 0.05	4970 ± 57	89.7 ± 7.9	$2.88^{+0.12}_{-0.13}$	$12.85^{+0.59}_{-0.57}$	$2.66^{+0.03}_{-0.04}$
HIP2611*	2.57 ± 0.13	-0.05 ± 0.03	4822 ± 46	62.0 ± 6.6	$1.61^{+0.17}_{-0.2}$	$11.0^{+0.26}_{-0.22}$	$2.53^{+0.06}_{-0.06}$
HIP3031	2.64 ± 0.05	-0.5 ± 0.03	5059 ± 27	46.8 ± 1.6	$1.7^{+0.06}_{-0.04}$	$9.04^{+0.16}_{-0.15}$	$2.74^{+0.02}_{-0.02}$
HIP3179	2.38 ± 0.18	0.02 ± 0.06	4806 ± 84	703.0 ± 25.4	$4.47^{+0.1}_{-0.1}$	$37.16^{+1.17}_{-1.04}$	$1.93^{+0.02}_{-0.02}$
HIP3231	2.86 ± 0.09	-0.03 ± 0.03	5169 ± 30	87.2 ± 6.4	$3.04^{+0.06}_{-0.06}$	$11.35^{+0.43}_{-0.42}$	$2.79^{+0.02}_{-0.02}$
HIP3607	2.74 ± 0.09	-0.12 ± 0.03	4948 ± 35	57.9 ± 3.9	$1.92^{+0.12}_{-0.09}$	$10.16^{+0.33}_{-0.31}$	$2.69^{+0.04}_{-0.04}$
HIP3750	2.84 ± 0.1	-0.1 ± 0.03	4825 ± 38	19.0 ± 2.4	$1.22^{+0.12}_{-0.1}$	$6.24^{+0.39}_{-0.36}$	$2.91^{+0.05}_{-0.05}$
HIP3834*	3.22 ± 0.09	0.04 ± 0.03	4988 ± 39	14.9 ± 1.1	$1.64^{+0.1}_{-0.08}$	$5.13^{+0.2}_{-0.19}$	$3.22^{+0.04}_{-0.04}$
HIP4422	2.5 ± 0.1	-0.33 ± 0.03	4905 ± 28	57.0 ± 2.3	$1.01^{+0.2}_{-0.1}$	$10.56^{+0.24}_{-0.29}$	$2.38^{+0.06}_{-0.02}$
HIP4552*	3.24 ± 0.16	0.14 ± 0.03	4917 ± 47	13.6 ± 0.7	$1.58^{+0.08}_{-0.1}$	$5.05^{+0.16}_{-0.15}$	$3.21^{+0.04}_{-0.04}$
HIP4906	2.6 ± 0.06	-0.23 ± 0.02	4929 ± 28	64.2 ± 2.4	$1.67^{+0.09}_{-0.1}$	$10.9^{+0.16}_{-0.22}$	$2.57^{+0.03}_{-0.04}$
HIP4914	2.4 ± 0.11	-0.27 ± 0.03	4598 ± 46	92.2 ± 5.8	$1.49^{+0.13}_{-0.16}$	$14.63^{+0.53}_{-0.52}$	$2.26^{+0.05}_{-0.06}$
HIP5364	2.49 ± 0.19	0.09 ± 0.05	4638 ± 85	74.2 ± 2.3	$1.71^{+0.21}_{-0.23}$	$13.18^{+0.47}_{-0.54}$	$2.42^{+0.06}_{-0.08}$
HIP9631	2.72 ± 0.14	-0.05 ± 0.05	4885 ± 59	55.0 ± 8.1	$1.9^{+0.18}_{-0.17}$	$10.31^{+0.62}_{-0.61}$	$2.68^{+0.08}_{-0.09}$
HIP9884*	2.32 ± 0.15	-0.13 ± 0.03	4575 ± 60	82.7 ± 2.6	$1.48^{+0.17}_{-0.23}$	$14.16^{+0.44}_{-0.38}$	$2.28^{+0.07}_{-0.09}$
HIP11432	2.42 ± 0.15	-0.07 ± 0.03	4613 ± 56	55.3 ± 4.1	$1.15^{+0.23}_{-0.17}$	$10.98^{+0.67}_{-0.29}$	$2.39^{+0.05}_{-0.05}$
HIP11791*	2.85 ± 0.09	0.03 ± 0.03	4885 ± 41	51.5 ± 4.1	$2.03^{+0.14}_{-0.1}$	$9.71^{+0.37}_{-0.36}$	$2.76^{+0.05}_{-0.05}$
HIP12247*	2.77 ± 0.12	0.05 ± 0.04	4897 ± 52	50.5 ± 4.5	$2.04^{+0.18}_{-0.12}$	$9.75^{+0.42}_{-0.42}$	$2.76^{+0.06}_{-0.06}$
HIP20889*	2.75 ± 0.17	0.22 ± 0.05	4954 ± 65	81.5 ± 3.0	$2.86^{+0.1}_{-0.11}$	$12.36^{+0.28}_{-0.27}$	$2.69^{+0.02}_{-0.03}$
HIP27253*	3.81 ± 0.07	0.36 ± 0.03	5632 ± 42	5.5 ± 0.2	$1.45^{+0.02}_{-0.02}$	$2.43^{+0.06}_{-0.06}$	$3.81^{+0.02}_{-0.02}$
HIP31592*	3.18 ± 0.17	0.22 ± 0.05	4801 ± 84	11.6 ± 0.4	$1.34^{+0.16}_{-0.16}$	$4.91^{+0.16}_{-0.15}$	$3.17^{+0.07}_{-0.08}$
HIP36616*	2.51 ± 0.14	0.14 ± 0.04	4648 ± 62	76.7 ± 4.7	$1.82^{+0.26}_{-0.23}$	$13.17^{+0.59}_{-0.63}$	$2.44^{+0.06}_{-0.06}$

[2]Should Gaia DR2 parallaxes be available before submission of this manuscript, they will be used instead of *Hipparcos* and this analysis reran.

HIP36795*	3.75 ± 0.12	0.05 ± 0.06	6289 ± 79	8.4 ± 0.3	$1.58^{+0.04}_{-0.1}$	$2.41^{+0.06}_{-0.06}$	$3.85^{+0.02}_{-0.03}$
HIP37826*	3.01 ± 0.1	0.11 ± 0.03	4943 ± 45	38.6 ± 1.2	$2.22^{+0.07}_{-0.07}$	$8.57^{+0.09}_{-0.07}$	$2.9^{+0.02}_{-0.02}$
HIP39311*	2.03 ± 0.16	-0.37 ± 0.02	4382 ± 54	157.2 ± 7.7	$1.13^{+0.14}_{-0.14}$	$21.17^{+0.69}_{-0.66}$	$1.82^{+0.07}_{-0.07}$
HIP40526*	1.41 ± 0.32	-0.25 ± 0.05	4153 ± 100	610.1 ± 28.0	$1.62^{+0.21}_{-0.25}$	$48.17^{+2.12}_{-2.05}$	$1.26^{+0.08}_{-0.1}$
HIP42527*	2.31 ± 0.17	-0.14 ± 0.04	4525 ± 65	120.0 ± 6.0	$1.66^{+0.21}_{-0.2}$	$17.4^{+0.66}_{-0.63}$	$2.16^{+0.08}_{-0.08}$
HIP46390	1.6 ± 0.35	-0.06 ± 0.05	4215 ± 110	835.0 ± 29.6	$3.1^{+0.67}_{-0.6}$	$52.51^{+3.52}_{-2.74}$	$1.47^{+0.13}_{-0.14}$
HIP46471*	2.42 ± 0.08	-0.29 ± 0.02	4817 ± 29	57.2 ± 4.2	$1.02^{+0.14}_{-0.09}$	$10.64^{+0.21}_{-0.26}$	$2.38^{+0.04}_{-0.02}$
HIP48455*	2.62 ± 0.32	0.22 ± 0.06	4572 ± 137	52.6 ± 1.7	$1.44^{+0.3}_{-0.2}$	$11.15^{+0.21}_{-0.22}$	$2.48^{+0.09}_{-0.06}$
HIP50546	3.34 ± 0.17	0.23 ± 0.05	4844 ± 83	8.7 ± 0.4	$1.35^{+0.15}_{-0.16}$	$4.16^{+0.14}_{-0.14}$	$3.31^{+0.07}_{-0.08}$
HIP50583*	2.01 ± 0.15	-0.38 ± 0.03	4495 ± 54	340.3 ± 17.3	$1.99^{+0.28}_{-0.18}$	$29.62^{+1.08}_{-1.04}$	$1.78^{+0.08}_{-0.06}$
HIP50786*	4.12 ± 0.18	0.36 ± 0.07	6408 ± 92	6.2 ± 0.2	$1.61^{+0.03}_{-0.03}$	$1.98^{+0.07}_{-0.07}$	$4.03^{+0.03}_{-0.03}$
HIP52686	2.71 ± 0.2	0.15 ± 0.04	4634 ± 74	25.7 ± 1.0	$1.24^{+0.18}_{-0.17}$	$7.86^{+0.31}_{-0.28}$	$2.72^{+0.08}_{-0.09}$
HIP56510	2.52 ± 0.09	-0.13 ± 0.03	4810 ± 39	114.3 ± 19.7	$2.17^{+0.37}_{-0.55}$	$13.77^{+1.59}_{-1.59}$	$2.46^{+0.05}_{-0.05}$
HIP56583	2.68 ± 0.07	-0.21 ± 0.03	4939 ± 34	46.7 ± 1.9	$1.89^{+0.04}_{-0.08}$	$9.27^{+0.22}_{-0.22}$	$2.76^{+0.03}_{-0.03}$
HIP57757	4.13 ± 0.14	0.27 ± 0.03	6268 ± 36	3.5 ± 0.1	$1.39^{+0.01}_{-0.01}$	$1.56^{+0.03}_{-0.03}$	$4.18^{+0.02}_{-0.02}$
HIP58110	3.22 ± 0.09	0.05 ± 0.03	5050 ± 36	16.4 ± 0.7	$1.87^{+0.07}_{-0.08}$	$5.26^{+0.14}_{-0.13}$	$3.25^{+0.03}_{-0.03}$
HIP58952*	2.55 ± 0.1	-0.28 ± 0.03	4766 ± 43	53.1 ± 3.0	$1.06^{+0.38}_{-0.14}$	$10.53^{+0.26}_{-0.26}$	$2.39^{+0.14}_{-0.03}$
HIP59316	1.83 ± 0.27	-0.01 ± 0.05	4436 ± 103	835.1 ± 35.8	$4.13^{+0.47}_{-0.41}$	$48.65^{+2.12}_{-2.38}$	$1.66^{+0.09}_{-0.07}$
HIP59501	2.75 ± 0.1	-0.05 ± 0.04	5004 ± 41	99.0 ± 7.6	$2.81^{+0.12}_{-0.15}$	$12.87^{+0.51}_{-0.49}$	$2.65^{+0.03}_{-0.03}$
HIP60202	2.49 ± 0.08	-0.26 ± 0.03	4830 ± 36	114.0 ± 5.6	$2.25^{+0.15}_{-0.17}$	$14.93^{+0.42}_{-0.41}$	$2.42^{+0.04}_{-0.04}$
HIP61740*	2.07 ± 0.3	0.15 ± 0.07	4487 ± 128	151.7 ± 9.1	$1.99^{+0.33}_{-0.42}$	$20.71^{+1.31}_{-1.16}$	$2.09^{+0.11}_{-0.15}$
HIP64078	2.55 ± 0.18	0.1 ± 0.04	4706 ± 57	92.5 ± 4.4	$2.26^{+0.27}_{-0.23}$	$14.26^{+0.5}_{-0.54}$	$2.46^{+0.07}_{-0.07}$
HIP64408*	4.02 ± 0.08	0.22 ± 0.02	5745 ± 27	4.1 ± 0.1	$1.28^{+0.01}_{-0.01}$	$2.02^{+0.04}_{-0.04}$	$3.92^{+0.01}_{-0.01}$
HIP66903*	2.68 ± 0.12	0.07 ± 0.03	4891 ± 44	47.3 ± 2.7	$2.03^{+0.12}_{-0.08}$	$9.56^{+0.31}_{-0.3}$	$2.77^{+0.04}_{-0.04}$
HIP67927	4.91 ± 0.2	0.19 ± 0.14	6319 ± 207	8.6 ± 0.3	$-99.9^{+0.0}_{-0.0}$	$-99.9^{+0.0}_{-0.0}$	$-99.9^{+0.0}_{-0.0}$
HIP68895	2.56 ± 0.13	-0.05 ± 0.03	4634 ± 54	59.9 ± 1.9	$1.41^{+0.17}_{-0.28}$	$11.6^{+0.39}_{-0.53}$	$2.44^{+0.06}_{-0.1}$
HIP70012	2.65 ± 0.1	-0.06 ± 0.03	4867 ± 42	61.7 ± 3.6	$1.75^{+0.15}_{-0.14}$	$10.88^{+0.23}_{-0.33}$	$2.59^{+0.05}_{-0.05}$
HIP70027	2.57 ± 0.24	0.26 ± 0.06	4618 ± 101	48.0 ± 1.9	$1.18^{+0.56}_{-0.13}$	$11.01^{+0.23}_{-0.35}$	$2.4^{+0.18}_{-0.04}$
HIP70987	2.5 ± 0.11	-0.06 ± 0.04	4812 ± 47	42.2 ± 4.3	$1.08^{+0.55}_{-0.15}$	$10.37^{+0.44}_{-0.67}$	$2.39^{+0.27}_{-0.03}$
HIP71837	2.83 ± 0.07	-0.13 ± 0.03	5038 ± 34	93.7 ± 8.1	$2.7^{+0.12}_{-0.15}$	$12.02^{+0.5}_{-0.49}$	$2.69^{+0.03}_{-0.03}$
HIP72125	3.07 ± 0.09	0.06 ± 0.04	5096 ± 48	79.9 ± 3.7	$3.03^{+0.05}_{-0.05}$	$11.07^{+0.28}_{-0.29}$	$2.81^{+0.02}_{-0.02}$
HIP72607*	1.55 ± 0.36	-0.27 ± 0.05	4188 ± 113	420.3 ± 13.0	$1.39^{+0.3}_{-0.28}$	$38.86^{+1.82}_{-1.69}$	$1.38^{+0.12}_{-0.13}$
HIP72631	2.55 ± 0.11	-0.32 ± 0.03	4838 ± 38	53.2 ± 3.3	$0.97^{+0.24}_{-0.07}$	$10.43^{+0.27}_{-0.25}$	$2.37^{+0.07}_{-0.02}$
HIP73133	1.76 ± 0.4	-0.07 ± 0.06	4182 ± 126	321.6 ± 40.1	$1.49^{+0.37}_{-0.32}$	$33.49^{+2.85}_{-2.64}$	$1.54^{+0.14}_{-0.14}$
HIP73634	2.72 ± 0.1	0.09 ± 0.03	4883 ± 40	49.4 ± 3.1	$2.03^{+0.13}_{-0.09}$	$9.75^{+0.31}_{-0.32}$	$2.75^{+0.04}_{-0.04}$
HIP74793*	2.1 ± 0.29	-0.02 ± 0.04	4337 ± 96	224.2 ± 12.3	$1.78^{+0.31}_{-0.3}$	$26.06^{+1.31}_{-1.24}$	$1.84^{+0.1}_{-0.11}$
HIP75049*	2.43 ± 0.09	-0.26 ± 0.02	4779 ± 29	49.1 ± 3.9	$0.95^{+0.12}_{-0.05}$	$10.45^{+0.22}_{-0.21}$	$2.36^{+0.03}_{-0.02}$
HIP75458*	2.81 ± 0.21	0.19 ± 0.04	4628 ± 86	58.2 ± 1.7	$1.65^{+0.19}_{-0.17}$	$11.27^{+0.45}_{-0.24}$	$2.53^{+0.06}_{-0.06}$
HIP76311*	2.59 ± 0.24	0.31 ± 0.05	4646 ± 100	70.6 ± 5.4	$2.04^{+0.59}_{-0.39}$	$12.47^{+0.73}_{-0.65}$	$2.53^{+0.15}_{-0.12}$
HIP76534	3.09 ± 0.04	-0.4 ± 0.02	5029 ± 18	22.0 ± 0.8	$1.48^{+0.05}_{-0.05}$	$6.01^{+0.12}_{-0.11}$	$3.03^{+0.02}_{-0.02}$
HIP77578*	2.66 ± 0.1	-0.11 ± 0.04	4903 ± 49	62.0 ± 3.4	$1.77^{+0.17}_{-0.15}$	$10.77^{+0.25}_{-0.34}$	$2.61^{+0.06}_{-0.06}$
HIP77655*	3.26 ± 0.1	0.14 ± 0.03	4883 ± 42	12.2 ± 0.4	$1.5^{+0.09}_{-0.09}$	$4.83^{+0.1}_{-0.1}$	$3.23^{+0.04}_{-0.04}$
HIP77853	2.56 ± 0.09	-0.21 ± 0.03	4844 ± 36	65.8 ± 2.2	$1.49^{+0.12}_{-0.12}$	$11.12^{+0.2}_{-0.17}$	$2.5^{+0.04}_{-0.04}$
HIP78159*	2.06 ± 0.18	-0.14 ± 0.03	4464 ± 54	141.6 ± 5.8	$1.56^{+0.16}_{-0.15}$	$19.68^{+0.61}_{-0.59}$	$2.03^{+0.06}_{-0.06}$
HIP79043	3.29 ± 0.15	0.01 ± 0.06	5238 ± 76	120.7 ± 15.4	$2.99^{+0.05}_{-0.06}$	$10.7^{+0.19}_{-0.33}$	$2.84^{+0.02}_{-0.01}$
HIP80894	2.94 ± 0.12	0.21 ± 0.04	5150 ± 52	104.8 ± 4.9	$3.32^{+0.05}_{-0.05}$	$12.53^{+0.43}_{-0.31}$	$2.74^{+0.02}_{-0.02}$
HIP81660	1.97 ± 0.18	-0.05 ± 0.05	4589 ± 74	756.7 ± 62.2	$4.46^{+0.19}_{-0.23}$	$42.37^{+2.2}_{-2.11}$	$1.82^{+0.04}_{-0.05}$
HIP81833	2.98 ± 0.08	-0.08 ± 0.03	5105 ± 30	44.7 ± 1.4	$2.28^{+0.06}_{-0.06}$	$8.66^{+0.13}_{-0.13}$	$2.9^{+0.01}_{-0.02}$
HIP85670	2.68 ± 0.31	0.04 ± 0.09	5428 ± 100	937.2 ± 35.1	$4.46^{+0.08}_{-0.08}$	$36.2^{+0.95}_{-0.84}$	$1.95^{+0.02}_{-0.02}$
HIP85715	2.89 ± 0.09	0.1 ± 0.04	5093 ± 50	81.6 ± 5.8	$2.81^{+0.1}_{-0.08}$	$11.67^{+0.43}_{-0.43}$	$2.73^{+0.03}_{-0.03}$
HIP87847	2.36 ± 0.14	-0.0 ± 0.04	4755 ± 58	116.7 ± 9.8	$2.49^{+0.22}_{-0.3}$	$15.68^{+0.77}_{-0.73}$	$2.42^{+0.06}_{-0.06}$
HIP88048	2.56 ± 0.13	0.18 ± 0.04	4959 ± 55	104.2 ± 4.0	$3.03^{+0.09}_{-0.1}$	$13.92^{+0.31}_{-0.3}$	$2.61^{+0.02}_{-0.02}$
HIP89047*	3.39 ± 0.08	0.07 ± 0.03	4993 ± 39	10.5 ± 0.4	$1.58^{+0.06}_{-0.07}$	$4.3^{+0.1}_{-0.1}$	$3.35^{+0.03}_{-0.03}$
HIP89962	3.09 ± 0.06	-0.14 ± 0.02	4984 ± 24	18.0 ± 0.5	$1.57^{+0.06}_{-0.06}$	$5.64^{+0.1}_{-0.1}$	$3.11^{+0.02}_{-0.02}$
HIP90067	2.12 ± 0.18	-0.14 ± 0.03	4464 ± 67	136.7 ± 10.2	$1.54^{+0.2}_{-0.19}$	$19.21^{+0.91}_{-0.87}$	$2.04^{+0.07}_{-0.08}$
HIP90344*	2.05 ± 0.12	-0.4 ± 0.03	4464 ± 48	153.0 ± 7.4	$1.26^{+0.13}_{-0.13}$	$20.19^{+0.62}_{-0.61}$	$1.91^{+0.06}_{-0.06}$
HIP90496	2.67 ± 0.11	-0.08 ± 0.03	4760 ± 39	49.6 ± 1.5	$1.61^{+0.16}_{-0.66}$	$10.32^{+0.21}_{-0.22}$	$2.6^{+0.06}_{-0.23}$
HIP91105	2.94 ± 0.11	0.1 ± 0.04	5183 ± 39	88.1 ± 5.3	$3.12^{+0.05}_{-0.05}$	$11.37^{+0.4}_{-0.38}$	$2.8^{+0.02}_{-0.02}$

HIP92782	2.32 ± 0.15	-0.03 ± 0.04	4636 ± 57	163.6 ± 16.3	$2.35^{+0.2}_{-0.26}$	$19.42^{+0.98}_{-0.9}$	$2.21^{+0.04}_{-0.05}$
HIP92997	2.52 ± 0.2	0.07 ± 0.04	4572 ± 84	50.1 ± 2.7	$1.1^{+0.22}_{-0.11}$	$10.88^{+0.22}_{-0.24}$	$2.39^{+0.07}_{-0.03}$
HIP93864	2.15 ± 0.17	-0.16 ± 0.04	4506 ± 67	88.3 ± 6.2	$1.25^{+0.19}_{-0.17}$	$15.2^{+0.69}_{-0.67}$	$2.15^{+0.08}_{-0.08}$
HIP94302	2.85 ± 0.14	0.18 ± 0.05	4969 ± 71	101.9 ± 6.2	$3.0^{+0.1}_{-0.12}$	$13.59^{+0.46}_{-0.44}$	$2.63^{+0.02}_{-0.03}$
HIP96327	2.73 ± 0.22	-0.0 ± 0.07	5004 ± 82	178.3 ± 17.3	$3.27^{+0.12}_{-0.13}$	$17.45^{+0.94}_{-0.88}$	$2.45^{+0.04}_{-0.04}$
HIP96459	3.32 ± 0.1	0.06 ± 0.02	5034 ± 34	14.5 ± 0.5	$1.81^{+0.06}_{-0.08}$	$4.97^{+0.11}_{-0.11}$	$3.28^{+0.03}_{-0.03}$
HIP96481	2.29 ± 0.21	-0.07 ± 0.07	5489 ± 77	497.7 ± 156.1	$4.17^{+0.32}_{-0.29}$	$22.81^{+4.56}_{-3.16}$	$2.32^{+0.1}_{-0.12}$
HIP96837	2.49 ± 0.29	-0.01 ± 0.07	4928 ± 95	336.4 ± 25.6	$3.78^{+0.13}_{-0.13}$	$24.88^{+1.16}_{-1.09}$	$2.21^{+0.03}_{-0.03}$
HIP97938	2.56 ± 0.11	-0.17 ± 0.03	4765 ± 49	47.8 ± 2.1	$1.08^{+0.47}_{-0.17}$	$10.23^{+0.22}_{-0.27}$	$2.4^{+0.21}_{-0.04}$
HIP98571	2.37 ± 0.15	0.11 ± 0.05	4801 ± 70	190.1 ± 12.0	$3.45^{+0.12}_{-0.15}$	$19.3^{+0.78}_{-0.72}$	$2.39^{+0.03}_{-0.04}$
HIP99031	3.74 ± 0.06	0.03 ± 0.03	5183 ± 36	3.9 ± 0.1	$1.27^{+0.02}_{-0.02}$	$2.43^{+0.05}_{-0.05}$	$3.75^{+0.02}_{-0.02}$
HIP99951	3.02 ± 0.12	0.12 ± 0.05	5206 ± 64	131.1 ± 10.3	$3.35^{+0.06}_{-0.07}$	$13.28^{+0.48}_{-0.54}$	$2.7^{+0.03}_{-0.02}$
HIP103294	2.1 ± 0.15	-0.12 ± 0.05	4677 ± 62	220.7 ± 18.1	$2.61^{+0.22}_{-0.25}$	$22.38^{+1.05}_{-1.0}$	$2.14^{+0.05}_{-0.06}$
HIP105515	3.21 ± 0.11	0.08 ± 0.05	5274 ± 56	66.3 ± 2.9	$2.87^{+0.05}_{-0.05}$	$9.51^{+0.25}_{-0.3}$	$2.92^{+0.02}_{-0.02}$
HIP105854*	2.27 ± 0.26	0.09 ± 0.05	4612 ± 88	45.8 ± 2.7	$1.01^{+0.19}_{-0.05}$	$10.68^{+0.24}_{-0.22}$	$2.37^{+0.05}_{-0.02}$
HIP108868	2.76 ± 0.11	0.04 ± 0.04	4995 ± 50	53.1 ± 3.7	$2.28^{+0.17}_{-0.18}$	$9.74^{+0.34}_{-0.34}$	$2.8^{+0.04}_{-0.05}$
HIP109352	2.64 ± 0.11	-0.13 ± 0.03	4931 ± 36	48.4 ± 2.9	$1.92^{+0.06}_{-0.06}$	$9.61^{+0.33}_{-0.33}$	$2.74^{+0.04}_{-0.04}$
HIP109572	4.11 ± 0.22	0.08 ± 0.12	6293 ± 187	8.8 ± 0.3	$1.62^{+0.06}_{-0.08}$	$2.4^{+0.11}_{-0.12}$	$3.86^{+0.05}_{-0.03}$
HIP109577	3.26 ± 0.09	0.09 ± 0.03	5001 ± 41	13.0 ± 0.7	$1.65^{+0.1}_{-0.07}$	$4.8^{+0.14}_{-0.14}$	$3.28^{+0.04}_{-0.03}$
HIP109754	1.88 ± 0.35	0.0 ± 0.06	4324 ± 124	536.9 ± 76.3	$3.01^{+0.51}_{-0.89}$	$39.72^{+3.61}_{-3.27}$	$1.7^{+0.11}_{-0.17}$
HIP110003	2.78 ± 0.12	0.18 ± 0.04	5022 ± 43	72.7 ± 2.9	$2.78^{+0.07}_{-0.07}$	$11.47^{+0.25}_{-0.24}$	$2.75^{+0.02}_{-0.02}$
HIP112731	2.13 ± 0.11	-0.48 ± 0.02	4476 ± 37	137.8 ± 9.3	$1.11^{+0.1}_{-0.09}$	$18.85^{+0.7}_{-0.67}$	$1.92^{+0.04}_{-0.05}$
HIP113148	3.1 ± 0.17	0.22 ± 0.04	4714 ± 71	12.4 ± 0.7	$1.22^{+0.15}_{-0.13}$	$5.2^{+0.19}_{-0.19}$	$3.07^{+0.07}_{-0.07}$
HIP114341	1.97 ± 0.17	-0.09 ± 0.04	4526 ± 68	309.9 ± 14.5	$2.69^{+0.27}_{-0.28}$	$28.29^{+1.01}_{-0.99}$	$1.95^{+0.06}_{-0.07}$
HIP114855*	2.7 ± 0.15	0.05 ± 0.04	4742 ± 62	49.8 ± 2.0	$1.64^{+0.28}_{-0.6}$	$10.52^{+0.37}_{-0.56}$	$2.58^{+0.13}_{-0.2}$
HIP115126	4.0 ± 0.06	0.2 ± 0.03	5527 ± 38	3.3 ± 0.4	$1.17^{+0.04}_{-0.04}$	$1.87^{+0.09}_{-0.09}$	$3.95^{+0.03}_{-0.03}$
HIP116727*	3.22 ± 0.14	0.13 ± 0.04	4801 ± 60	11.7 ± 0.4	$1.3^{+0.13}_{-0.13}$	$4.87^{+0.13}_{-0.13}$	$3.16^{+0.06}_{-0.06}$
HIP118209	3.23 ± 0.08	0.1 ± 0.04	5202 ± 53	55.4 ± 2.8	$2.74^{+0.04}_{-0.03}$	$8.54^{+0.14}_{-0.17}$	$3.0^{+0.01}_{-0.01}$

4.5.1 Comparison of spectroscopic parameters to literature values

For comparison to literature values, we used the PASTEL catalogue (Soubiran et al., 2016), a heterogeneous compilation of literature stellar atmospheric parameters. 104 of the 109 stars in our sample appear in the catalogue. If we compare our values to all values in the catalogue we have excellent agreement with a median and standard deviation offset (SONG value minus literature value) $\Delta T_{\rm eff} = 75 \pm 157$K, $\Delta \log g = 0.00 \pm 0.38$ dex and Δ[Fe/H] $= 0.06 \pm 0.12$ dex. If we compare to a homogeneous subsample of the PASTEL catalogue, the largest overlap is 75 stars from McWilliam (1990), and the offsets are $\Delta T_{\rm eff} = 133 \pm 82$K, $\Delta \log g = -0.12 \pm 0.29$ dex and Δ[FeH] $= 0.13 \pm 0.09$ dex respectively. We also have an overlap of 51 stars

with Hekker & Meléndez (2007), who also analyse their stars using ARES and MOOG. Here the offsets are are $\Delta T_{\rm eff} = 32 \pm 75$K, $\Delta \log g = -0.18 \pm 0.26$ dex and Δ[FeH] = 0.08$\pm$0.08 dex respectively. Figure 4.4 shows the results for SONG against results from PASTEL (blue dots), Hekker & Meléndez (2007) (orange triangles) and McWilliam (1990) (green stars). While overall agreement between our results and the PASTEL catalogue is good, there are some outliers for individual literature sources within PASTEL. HD 203949 has a reported $\log g = 4$ and $T_{\rm eff} = 6720$K in Glaspey et al. (1994). Other literature sources within PASTEL (Jones et al., 2011; Jofré et al., 2015a) find the star to be $\log g \approx 2.95$ dex and $T_{\rm eff} = 4750$K. SONG finds the star to be $\log g = 2.27 \pm 0.0.26$ dex and $T_{\rm eff} = 4612 \pm 88$K, in agreement within 3σ (1σ in temperature). For metallicity the largest offset between SONG and a PASTEL literature source is for HD 5395, where SONG [Fe/H] $= -0.34 \pm 0.03$, and Fernandez-Villacanas et al. (1990) that report [Fe/H] $= -1.00$ dex. Other literature sources within PASTEL report metallicites in the range [Fe/H]=-0.19 to -0.4 dex, with most other values around [Fe/H] $\approx -0.33 \pm 0.05$ dex.

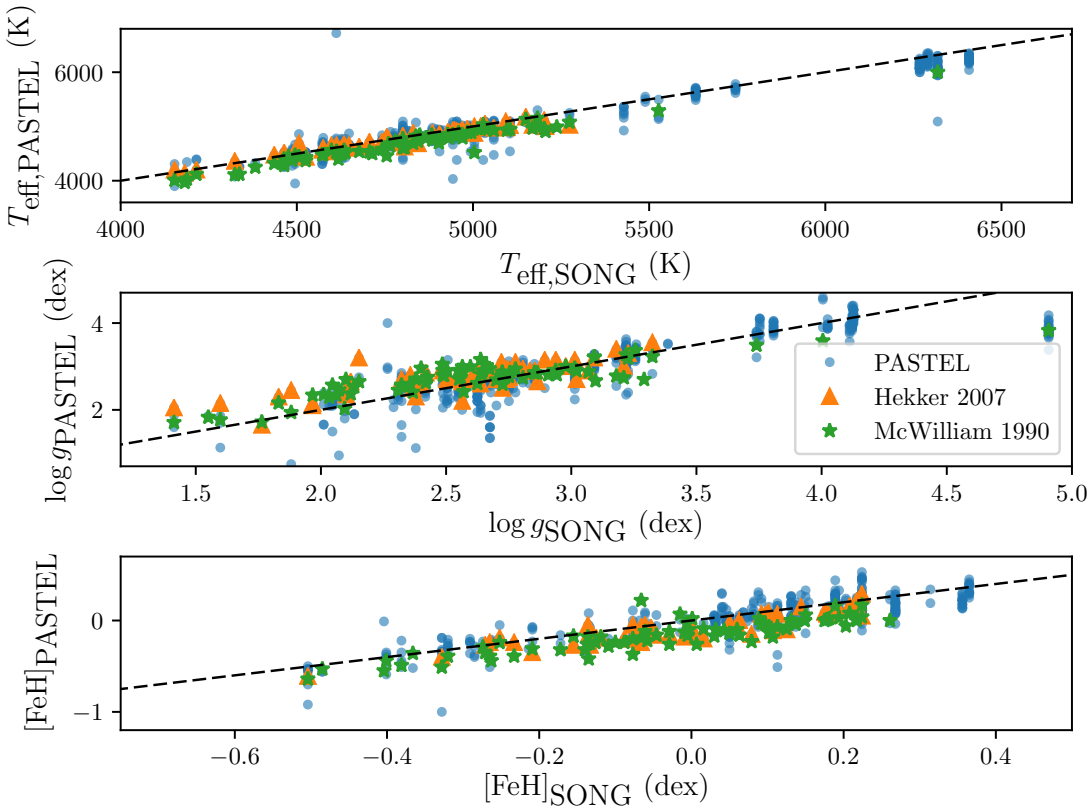

Figure 4.4: Comparison of SONG results to other literature values overall show good agreement within uncertainties. The large outlier in $T_{\rm eff}$ is a literature outlier, rather than SONG.

For only one star was PARAM unable to return a mass. HIP 67927/η Boo appears to have been misidentified in the spectral analysis as a dwarf star, rather than a subgiant. The star is also a suspected spectroscopic binary, and is listed in SIMBAD as such.

4.5.2 Comparison to literature stellar properties

Since the PASTEL catalogue only provides spectroscopic parameters, we cannot use it for comparison to stellar mass and other properties. Instead we compare our masses for the 51 stars in common with the radial velocity survey of Reffert et al. (2015), labelled Lick Giant Stars in Table 4.1. In Reffert et al. an additional estimate given is the probability of the star being either an RGB star or horizontal branch star. For each star we take the results assigned the highest probability.

The Reffert et al. results are on average cooler and lower mass than our values. We note that the $T_{\rm eff}$ values for Reffert et al. are model dependent, returned from the stellar models rather than observational values. Additionally, different stellar models are used between the two sets of results. The mean difference in mass is $\Delta M = 0.22 \pm 0.34 \mathrm{M}_{\odot}$. The largest individual mass difference is at the 2.7σ level, while the mean difference is 0.68σ, where the errors on both mass values were added in quadrature.

4.5.3 Comparison of input parameters and returned properties

Since $\log g$ is used as an input parameter (from the spectroscopic solution based upon SONG observations) during the recovery of the stellar properties with PARAM, it is worth investigating how well the output $\log g$ (from best fitting stellar models to all observables) agrees with the input, and to explore any discrepancies. This is primarily a sanity check that the recovered spectroscopic solutions are consistent with stellar evolution theory i.e., the observed spectroscopic and luminosity parameters describe a star that can physically exist. The greatest discrepancy is for η Boo as discussed above. The only other star with a $\log g$ difference at > 0.5dex is HIP 85670. It is a high mass giant star at the upper limit of the models we consider. Interestingly, PARAM is able to recover a mass and $\log g_{\rm PARAM}$ for this star consistent with literature sources. No $\log g$ discrepancy is at $> 3\sigma$ level. Figure 4.5 shows input and output $\log g$ plotted against one another (left panel). Also shown is the difference between input $\log g_{\rm SONG}$ and recovered $\log g_{\rm PARAM}$ as a function of effective temperature (right panel). The mean offset in $\log g$ (recovered - observed) is $\Delta \log g = -0.09 \pm 0.13$dex. In the right panel, the average error of $\log g_{\rm PARAM}$ was added in quadrature to the input $\log g_{\rm SONG}$ error. It can be seen the distribution of errors has a large spread. Therefore the weighted mean offset was calculated, using $1/\sigma^2$ as the weighting factor. The resulting weighted mean offset

was $\Delta \log g = -0.06 \pm 0.01$ dex, which does reflect a statistically significant offset. However the level of the offset is within the typical observational uncertainties of $\sim$0.1 dex.

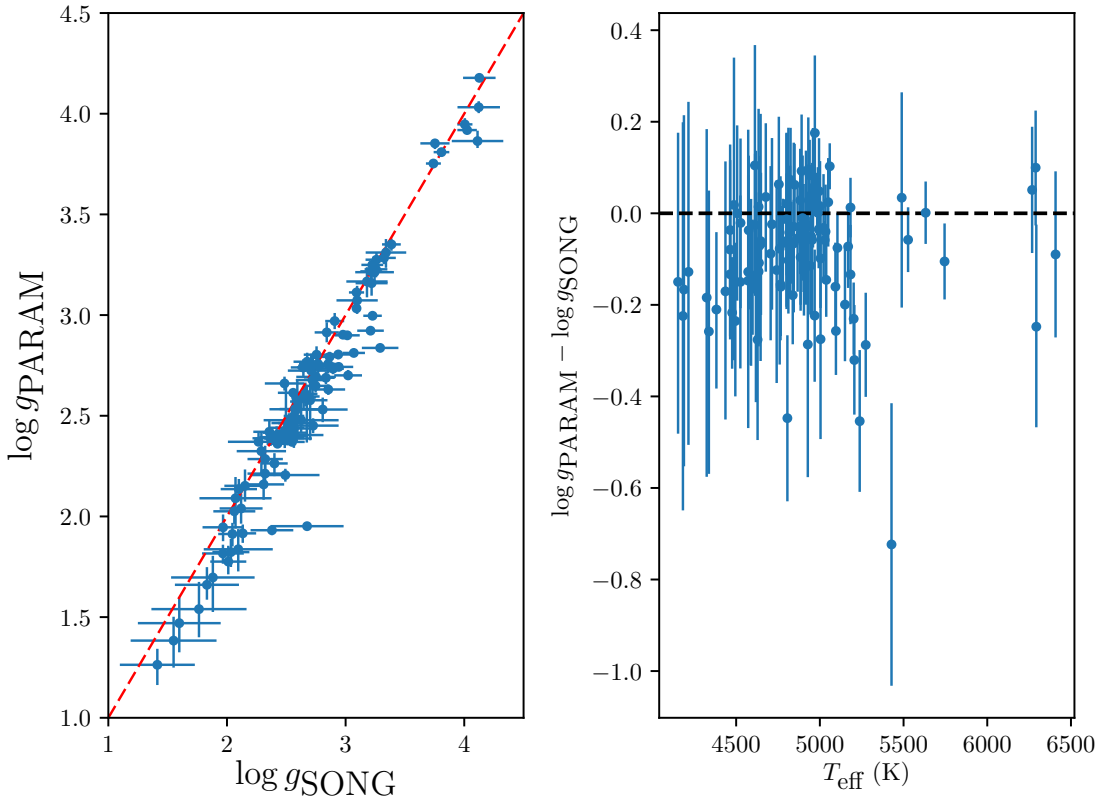

Figure 4.5: Left: $\log g_{\rm SONG}$ vs $\log g_{\rm PARAM}$. Right: Difference between SONG $\log g$ and PARAM $\log g$, as a function of stellar effective temperature

4.5.4 Different constraints during recovery of stellar properties

Given the controversy on the masses of evolved giants, the "retired A star" problem (see Chapter 2), it is worth investigating the impact of differing constraints on the recovered stellar properties. To do this, PARAM was run again, using only $T_{\rm eff}$, [Fe/H] and luminosity as constraints. This matches the stellar parameters used in Johnson et al. (2010a) to recover stellar properties, albeit from different stellar models. The average difference in recovered mass is small with $\Delta M = -0.03 \pm 0.11 M_{\odot}$. Figure 4.6 illustrates the shifts in recovered properties. Without $\log g$ as a

constraint, PARAM is allowed to shift $\log g$ to better match the other observables. Black lines in the figure indicate the same star. The upper panels show the recovered mass plotted against $T_{\rm eff}$ and the recovered $\log g$ from PARAM. The lower panels show the difference in mass between the two data sets.

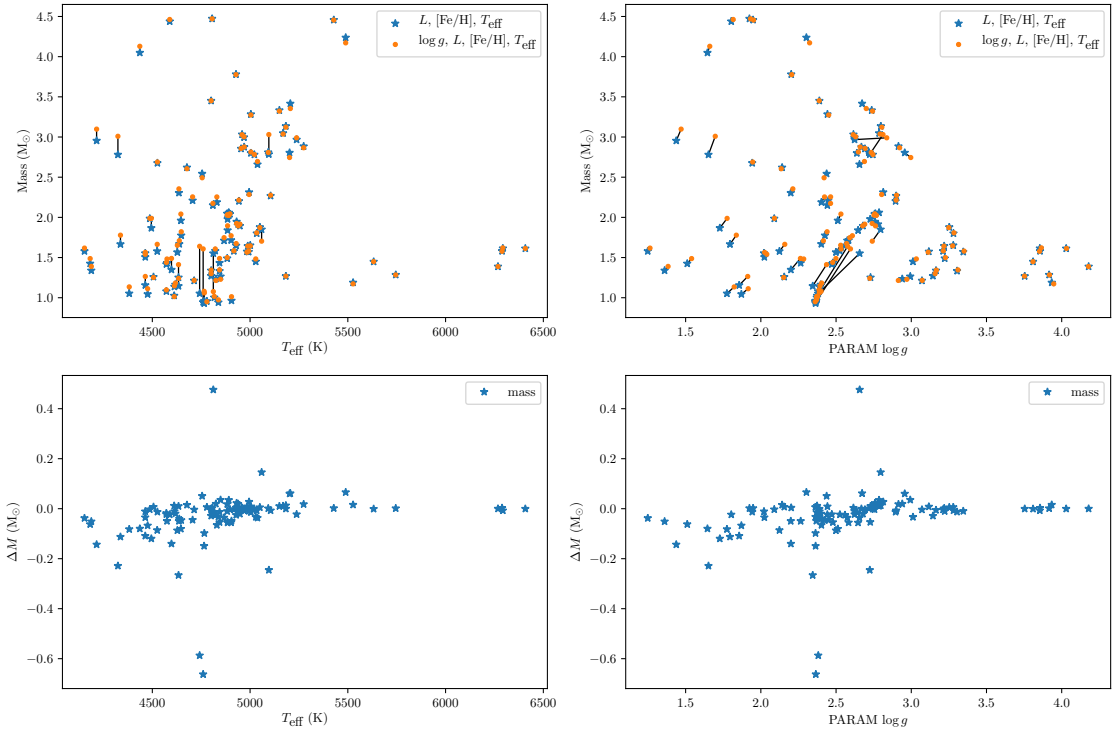

Figure 4.6: Removal of $\log g$ during PARAM fitting of stellar properties impacts the stellar mass recovered. Black lines link the same star between the two datasets. As can be seen in right upper panel, by removing $\log g$ as a constraint, PARAM will adjust $\log g$ to match other observables. Lower panels are the difference plots between PARAM without $\log g$ and with $\log g$ as a constraint.

4.5.5 Difference in metallicity distributions host and field stars

To assess if the metallicity distribution of the giant planet hosts differs from field stars, we calculated the Kolmogorov-Smirnov statistic on the two populations. We find a probability of $P = 20.7\%$. As such we cannot reject the hypothesis that the two samples are drawn from the same population. If the above is repeated after the removing the subgiants ($\log g > 3.5$) from the sample, then the probability increases

to $P = 33.2\%$. Given the small number of subgiants in our sample, we cannot statistically assess the metallicity distribution for these stars. Our results are in agreement with Mortier et al. (2013).

4.5.6 Asteroseismic stars

Only one star in the sample has detected solar-like oscillations HD 185351/HIP 96459, a star in the Johnson et al. (2006) Retired A Star sample. It was observed during the *Kepler* mission, and has since been subject to significant levels of research (Johnson et al., 2014; Ghezzi et al., 2015; Hjørringgaard et al., 2016; North et al., 2017a). Our spectroscopic results are consistent with values used in North et al. (2017a), as is our mass. As noted in that work, stellar masses derived from models without the inclusion of asteroseismology need to use carefully considered uncertainties on the spectroscopic and luminosity parameters, to ensure that the full parameter space can be explored. Underestimated uncertainties can bias the recovered mass. With the launch of the NASA TESS mission (Ricker et al., 2015), asteroseismology will be available on many of the stars in the this work (Campante et al., 2016), which combined with Gaia DR2 parallaxes, will allow for more accurate and precise masses to be produced.

4.6 Conclusions

In this work we have undertaken a homogeneous spectroscopic analysis of bright giant star exoplanet hosts previously detected by radial velocity measurements, and a suitable control of giant stars, also observed by radial velocity surveys, to assess if stars that host giant planets are at higher metallicities than giant stars without planets. This would be an extension of the relation seen in dwarf and subgiant stars. For our sample of 36 host stars and 73 field stars, we do not find statistical evidence that the hosts are of higher metallicity. We also present updated stellar properties for these stars. With the imminent launch of the NASA TESS Mission (Ricker et al., 2015), solar-like oscillations should be detected in many of these stars that will allow

characterisation using asteroseismology. Additionally *Gaia* DR2 parallaxes will be available to update luminosities for these stars.

5 Noise properties of red giants

The majority of the text in this chapter, beyond the opening paragraphs, is taken verbatim from North et al. (2017a). I was first author on the corresponding journal article. The introduction for this paper has been adapted in asteroseismology section of the thesis introduction (see Chapter 1). In terms of the work performed, all work in the chapter was done by myself, besides the definition of an appropriate filter, that was described in detail in Gilliland et al. (2011), and the development of the KASOC filter, that I compare my results to. This was described in Handberg & Lund (2014a). Since this paper was written with exoplanet researchers in mind, the asteroseismology was included in a self-contained manner. As can be seen, there is some repetition from the thesis introduction.

5.1 Introduction

All physical signals are subject to noise. Equally, one observer's noise is another's signal. An excellent example of this is found in the detection of exoplanets. When the first planets were detected using radial velocity observations, the stars were found to "jitter", with quasi-periodic signatures that can emulate the signal produced by a planet (Wright, 2005; Isaacson & Fischer, 2010; Oshagh et al., 2017; Robertson et al., 2014; Hatzes et al., 2018). For young, active stars, the stellar radial velocity jitter is caused by spots and phages on the stellar surface. For evolved stars, as the star evolves off the main sequence, and the convective outer regions deepen, the amplitude of the stellar granulation and oscillations increase, whilst magnetically driven stellar activity signatures decrease in amplitude. The stellar oscillations and

granulation, both well characterised by asteroseismology, are the dominant source of noise in subgiants and red giants (Bastien et al., 2013), in radial velocity and photometric observations. In this chapter we will only consider photometric observations from *Kepler*.

In this chapter we present a simple model of the noise properties relevant to transit detection around red giants, which employs scaling relations based on global asteroseismic parameters. The dominant contributions are those due to granulation and solar-like oscillations. This model is then used to estimate minimum detectable planet radii for different assumed orbital periods.

Red giants, stars near the end of their life – which have exhausted fuseable hydrogen in the stellar core, and bloated massively compared to their main-sequence radii – are a relatively new focus for photometric exoplanet research. The four years of near continuous, high-quality photometry from the NASA *Kepler* Mission has been a key driver in studies of exoplanets, including close in planets around evolved stars (Huber et al., 2013a; Steffen et al., 2013; Lillo-Box et al., 2014b; Ciceri et al., 2015; Barclay et al., 2015; Quinn et al., 2015). Previous exoplanet searches around giant stars have primarily been conducted using radial velocity measurements (Johnson et al., 2008; Reffert et al., 2015; Quirrenbach et al., 2015).

One reason for the interest in red giants is that when the Sun reaches this stage of evolution the fate of the Earth is a contentious matter, with the ultimate balance between mass loss and the maximum extent of the Sun being the deciding factors (Schröder & Connon Smith, 2008), along with the influence of tidal decay on the orbit. The timescales for dynamic evolution of the system are accelerated as the star evolves, with evidence of several planet hosts on course to devour their planets (Adamów et al., 2012b); an example is Kepler-56, a red giant with two detected transiting planets that are predicted to be consumed by their star in around 150 million years (Li et al., 2014).

Kepler has provided high precision measurements of stellar variability, and a

host of related phenomena, such as activity, stellar rotation (McQuillan et al., 2014) and the detection of intrinsic, oscillations in stars. The analysis of the detected oscillations – the field of asteroseismology – in principle provides very precise constraints on stellar properties, a key ingredient in the characterisation of exoplanets (Van Eylen et al., 2014). *Kepler* has observed solar-like oscillations in over 15,000 red giants (Hekker et al., 2011b; Mosser et al., 2012a,b; Stello et al., 2013a), another reason that a search for planets around giants is of interest. Asteroseismology may be used to discriminate between stars either ascending the red giant branch (RGB), or in the Helium core burning "red clump" (RC) phase (Bedding et al., 2011). This is particularly important for the possible detection, and existence, of close-in planets. Asteroseismic results on the stellar angle of inclination of the host star can also reveal if it is a misaligned system, where the stellar spin axis and plane of planetary orbits are not coplanar (Huber et al., 2013a). Finally, asteroseismology also provides well-constrained stellar ages (Silva Aguirre et al., 2015), allowing star and planet formation to be probed across Galactic history (Campante et al., 2015b).

The ability to detect a planetary transit is limited by multiple factors, the primary factor being the depth of the transit, which is directly related to the relative size of planet and host star. Another more subtle issue is the noise properties of the host star, which in cool main-sequence, sub-giant and red-giant stars can contain contributions from various stellar signals indicative of granulation, oscillations and activity. Additionally, there is a shot noise contribution to be considered and instrumental artefacts. Detecting the transit signal requires an understanding of the expected noise properties and the expected appearance of the transit in the lightcurve.

In this chapter we present a simple model of the noise properties relevant to transit detection around red giants, which employs scaling relations based on global asteroseismic parameters. The dominant contributions are those due to granulation and solar-like oscillations. This model is then used to estimate minimum detectable

planet radii for different assumed orbital periods.

Readers unfamiliar with asteroseismology will find an introduction to the relevant parameters in Section 5.2. The relevant parameters for the noise model are introduced in Section 5.2.1, and the current *Kepler* noise properties are discussed in Section 5.3. Finally, Section 5.4 covers the construction of the noise model and discusses the implications of the resulting predictions for detecting planets around red giants in *Kepler* data.

5.2 Asteroseismic global parameters

Solar-like oscillations are driven and damped by turbulent convection in the outer envelope of the star, with the amplitudes of these signals greatly enhanced in evolved stars (Baudin et al., 2011). Figure 5.1 shows an example red-giant frequency power spectrum, made from *Kepler* data on the target KIC 4953262. As discussed in Chapter 1, the asteroseismology I perform is based in the frequency power spectrum space, not the time domain.

The two main features of the power spectrum are the stellar granulation background, and solar-like oscillations. The oscillations are clearly visible above the background around 200μHz. Additionally, model fits to the components are overplotted, and will be returned to in Section 5.2.1. For the noise model detailed in Section 5.4, the individual oscillation modes do not need to be modelled, only the oscillation power envelope that contains them.

Figure 5.2 shows a zoom of the same power spectrum, around the region where the detected stellar oscillations are most prominent. The oscillations appear as fairly evenly spaced peaks in frequency. Overtones of the same angular degree, l, are spaced by the large frequency separation. The average large separation, $\Delta\nu$, scales to good approximation with the square-root of mean stellar density (Ulrich, 1986), i.e.,

$$\frac{\Delta\nu}{\Delta\nu_\odot} \simeq \left(\frac{M}{\mathrm{M}_\odot}\right)^{0.5} \left(\frac{R}{\mathrm{R}_\odot}\right)^{-1.5}. \tag{5.1}$$

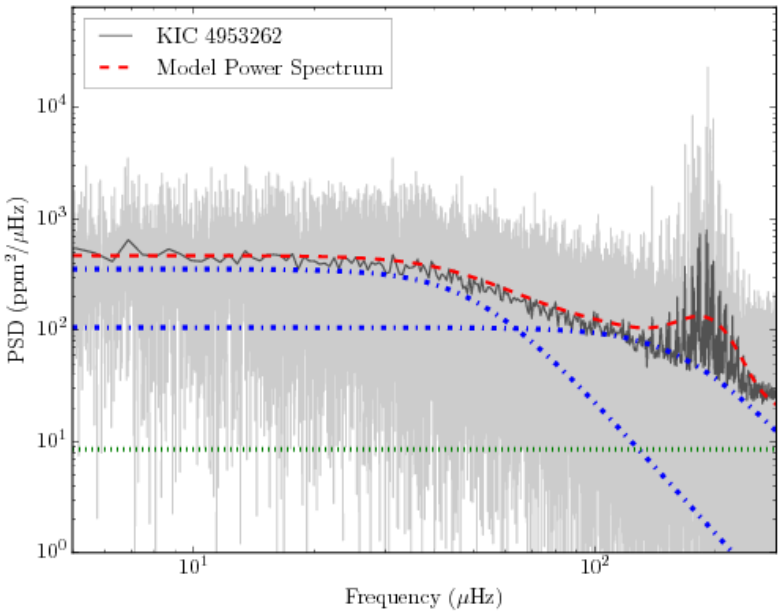

Figure 5.1: The power density spectrum for KIC 4953262, with the raw and smoothed power spectra in grey and black respectively. Green (dotted) indicates the shot noise level, showing it is a small factor for this star, whilst the blue (dashed dotted) show the two granulation components, red (dashed) is total model power spectrum including an oscillation component, where the individual modes are not modelled in this formulation.

The observed power of the mode peaks is modulated by an envelope that is usually taken as being a Gaussian, centered on the frequency $\nu_{\rm max}$, i.e., the frequency at which the detected oscillations show their strongest amplitudes. This characteristic frequency can be predicted from fundamental parameters. Its physical meaning is still debated (Belkacem et al., 2011), but it scales to very good approximation with the (isothermal) acoustic cut-off frequency in the stellar atmosphere, with numerous studies showing

$$\nu_{\rm ac} \propto \nu_{\rm max} \propto \frac{c}{H}. \tag{5.2}$$

Here, the speed of sound $c \propto \sqrt{T}$, T being the mean local atmospheric temperature, and $H \propto T/g$ is the pressure scale height of the atmosphere (Brown et al., 1991; Kjeldsen & Bedding, 1995). Equation 5.2 suggests the use of a relation scaled to solar values of the form

$$\frac{\nu_{\rm max}}{\nu_{\rm max,\odot}} \simeq \frac{g}{g_\odot}\left(\frac{T_{\rm eff}}{\rm T_{eff,\odot}}\right)^{-1/2}, \tag{5.3}$$

where, since oscillations are observed in the stellar photosphere, the temperature is set to $T = T_{\rm eff}$. In this work, the solar values adopted are: $g_\odot = 27400 {\rm cms}^{-2}$, $\nu_{\rm max,\odot} = 3090 \mu$Hz and $T_{\rm eff,\odot} = 5777$K (Chaplin et al., 2014). As discussed in Chap 1, these values are taken as absolute, however they may be subject to uncertainty.

Since all the stars considered in this chapter either have detected oscillations (real cohort) or would be predicted to show detected oscillations (synthetic cohort), $\nu_{\rm max}$ will typically be the parameter we choose to plot against when considering the noise properties of the stars.

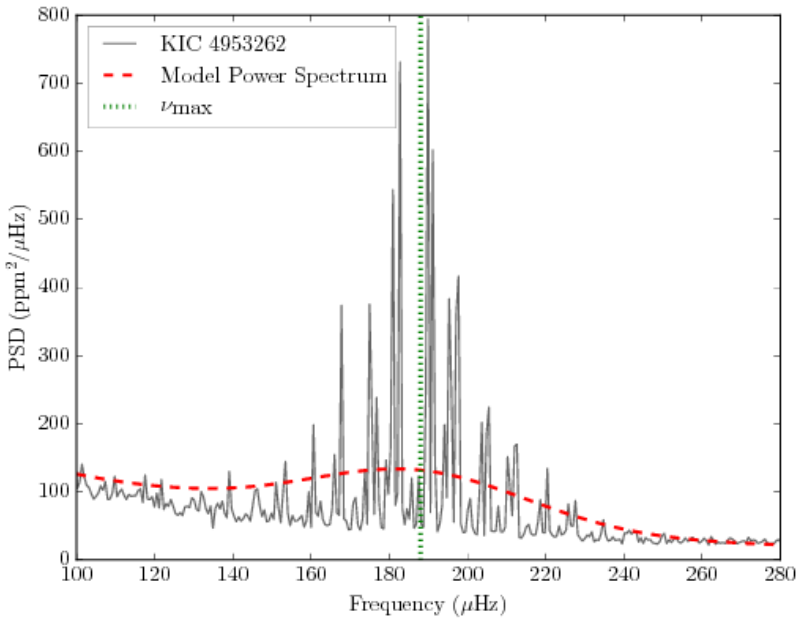

Figure 5.2: Smoothed power spectrum for KIC 4953262, a known oscillating red giant. The vertical dotted line indicates $\nu_{\rm max}$ for this star. Shown in red is a model of the power envelope of the oscillation spectrum.

First-order model independent estimates of stellar mass and radius can be estimated using the above scaling relations. Combining and re-arranging Equation 5.1 and Equation 5.3 gives (Chaplin & Miglio, 2013)

$$\frac{M}{\rm M_\odot} = \left(\frac{\nu_{\rm max}}{\nu_{\rm max,\odot}}\right)^3 \left(\frac{\Delta\nu}{\Delta\nu_\odot}\right)^{-4} \left(\frac{T_{\rm eff}}{\rm T_{eff,\odot}}\right)^{1.5}, \tag{5.4}$$

and

$$\frac{R}{\mathrm{R}_{\odot}} = \left(\frac{\nu_{\mathrm{max}}}{\nu_{\mathrm{max},\odot}}\right)\left(\frac{\Delta\nu}{\Delta\nu_{\odot}}\right)^{-2}\left(\frac{T_{\mathrm{eff}}}{\mathrm{T}_{\mathrm{eff},\odot}}\right)^{0.5}. \tag{5.5}$$

With the basic global asteroseismic parameters defined, we now go on to explore the noise properties of stars in terms of these parameters. All noise components will be described up to the Nyquist frequency of the long-cadence *Kepler* data. The 29.4-minute cadence leads to a Nyquist frequency of $\nu_{\mathrm{Nyq}} \approx 283\mu$Hz (Koch et al., 2010).

5.2.1 Modelling power due to the oscillations

For stars that have $\nu_{\mathrm{max}} \lesssim \nu_{\mathrm{Nyq}}$, the power contained in the oscillations must be considered a component of the background signal for transit detection. It is sufficient to describe the contribution due to the oscillations in terms of a Gaussian of excess power centred around the frequency ν_{max} (Equation 5.3). The width of the Gaussian is denoted by σ_{env}, as described by Equation 1 in Mosser et al. (2012a), i.e.,

$$\sigma_{\mathrm{env}} = \frac{\delta_{\mathrm{env}}}{2\sqrt{2\ln 2}}, \tag{5.6}$$

with δ_{env} describing the full width at half maximum (FWHM) of the oscillation envelope. The Gaussian also needs a height (maximum power spectral density), H, to give the final form of the oscillation envelope signature in the power spectrum:

$$\mathrm{PSD}_{\mathrm{osc}}(\nu) = H\exp\left[\frac{-(\nu-\nu_{\mathrm{max}})^2}{2\sigma_{\mathrm{env}}^2}\right]. \tag{5.7}$$

The height and envelope width, H and δ_{env}, may be described in terms of scaling relations expressed in the parameter ν_{max} (Mosser et al., 2012a), i.e.,

$$\begin{aligned} \delta_{\mathrm{env}} &= 0.66(\nu_{\mathrm{max}})^{0.88} \\ H &= 2.03\times10^{7}(\nu_{\mathrm{max}})^{-2.38}\ [\mathrm{ppm}^2\mu\mathrm{Hz}^{-1}]. \end{aligned} \tag{5.8}$$

As noted above, only the envelope describing the total oscillation power is considered and modelled. The power contained within individual modes is not required here. Returning to Figures 5.1 and 5.2, this envelope is plotted in red. With the oscillation contribution described, we move to describing the granulation parameters.

5.2.2 Granulation

A consequence of visible surface convection is granulation. As hot material rises on a plume, it cools at the surface and sinks back down. The stellar material forms cells, with a plume in the centre of each cell. Photometric granulation signatures for the Sun were initially modelled by Harvey (1985) as an exponentially decaying signal in the time domain. This is meant to represent the rapid rise in a convective plume, then the decay as the material cools. In photometric measurements this can be considered as the hotter material being intrinsically brighter, giving a brief spike in flux, before the material cools at the top of the plume, and grows dimmer, with the process occurring on some characteristic timescale.

This exponential in time leads to a Lorentzian when described in the power spectrum (in the frequency domain), and is known as a Harvey profile. Given that the exact nature of granulation is unclear, and that this simple formulation does not always appear to fit the granulation background well, this has in recent years led to a whole family of "Harvey-like" profiles (e.g., see Mathur et al. 2011), with varying formulations and exponents in the functions used. An important consideration for our work here is how granulation properties vary with stellar evolutionary state (once we have selected a preferred formulation). Does granulation in red giants exhibit the same behaviour as granulation observed in the Sun? In Kallinger et al. (2014), multiple models of granulation were fitted to power spectra over a range of stellar evolutionary states in cool stars to investigate updated versions of the original Harvey relation, including a change of exponent. Observed power spectra often require the use of multiple granulation components, operating at different

timescales, whereas the original Harvey model used only a single component, with an exponent of 2. We adopt a two-component granulation model, (described in Kallinger et al. 2014 as Model F) i,e.

$$\mathrm{PSD}_{\mathrm{gran}}(\nu) = \sum_{i=1}^{2} \frac{\xi_i a_i^2 / b_i}{1 + (\nu/b_i)^4}. \tag{5.9}$$

Here ξ_i is a normalisation constant equal to $2\sqrt{2}/\pi$ for the model, while a_i and b_i are the granulation amplitude and characteristic frequency, respectively, of each granulation component, which are both dependent on the fundamental properties of the stars. Since the granulation and stellar oscillations are both driven by convection, it is perhaps not surprising that the granulation amplitude and frequency can be described by scaling relations based on asteroseismic parameters. In this case they are based on the frequency of maximum power ν_{max}, i.e., from Kallinger et al. (2014) we have:

$$\begin{aligned} a_1 &= a_2 = 3710(\nu_{\mathrm{max}})^{-0.613}(M/\mathrm{M}_{\odot})^{-0.26}, \\ b_1 &= 0.317(\nu_{\mathrm{max}})^{0.97}, \\ b_2 &= 0.948(\nu_{\mathrm{max}})^{0.992}, \end{aligned} \tag{5.10}$$

with an additional constraint from the stellar mass for the granulation amplitude (which may be derived from Equation 5.4, using ν_{max}, $\Delta\nu$ and T_{eff} as input). Whilst in Kallinger et al. (2014) both amplitude components (a_1 and a_2) were allowed to vary during the fitting procedure, the final relation produced used a single amplitude relation for both components. The mass-dependent formulation was also found to be a better fit to the real data, and as such is the formulation used here for the granulation amplitude. For the cohort of real asteroseismic stars considered below (see Section 5.3) we estimate stellar masses and radii using the scaling relations defined in Equations 5.4 and 5.5, with the solar value taken to be 135.1μHz in this work (Chaplin et al., 2014)

Returning to Figure 5.1, the two granulation parameters plotted in blue, along

with the oscillation envelope detailed above, make up the model power spectrum in red. Additionally, the shot noise component is plotted in green, clearly a small contribution in this power spectrum. It is from the model spectrum that we may compute a suitable noise metric for the star.

5.3 *Kepler* CDPP

The primary *Kepler* noise metric is the CDPP, or Combined Differential Photometric Precision, which is designed to describe the noise properties of a star centred around a timescale of 6.5 hr (Christiansen et al., 2012; Gilliland et al., 2011). This is half the timescale on which an Earth analogue would transit a Sun-like star. Throughout the paper references to *Kepler* CDPP will refer to the 6.5 hr timescale. The CDPP will be composed of a shot noise component due to counting signals, but a significant stellar variability term should also be present. The nature of the stellar variability is dependent on the intrinsic stellar properties, with possible contributions from granulation, oscillations and activity.

Kepler lightcurves are produced in the Presearch Data Conditioning module (PDC) (Jenkins et al., 2010a; Smith et al., 2012; Stumpe et al., 2012), and in general the PDC pipeline is highly successful at removing systematics and instrumental effects in the lightcurves. However the PDC also removes real astrophysical signal at long periods (Murphy, 2014). This is of interest for evolved stars, having significant low-frequency signals typical of granulation and intrinsic oscillations. This loss of real signal has the effect of artificially reducing the reported CDPP, since real variability has been removed.

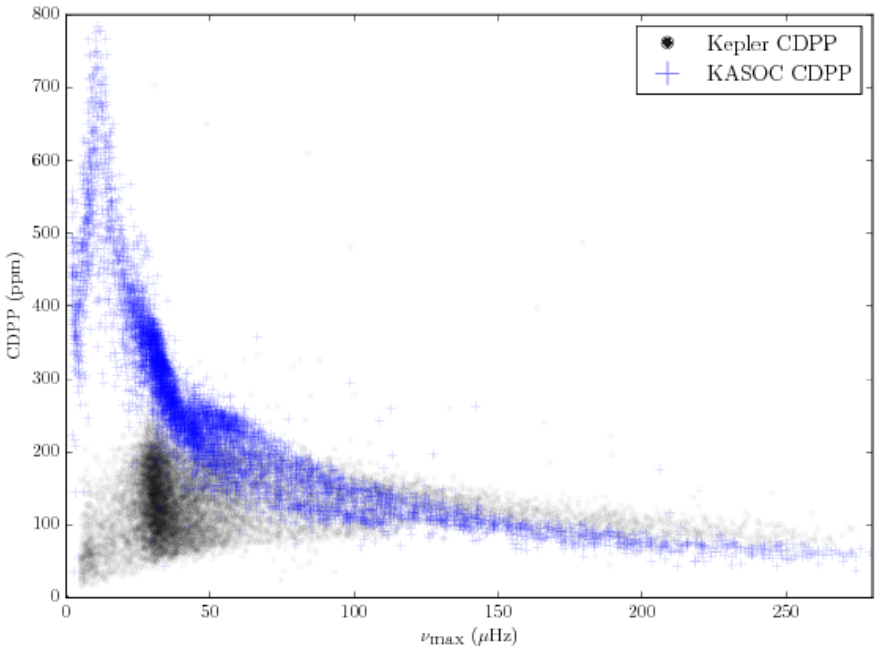

Figure 5.3: The reported CDPP for 13,000 evolved stars (Stello et al., 2013a) plotted against the reported asteroseismic $\nu_{\rm max}$ in black. The overall trend with decreasing $\nu_{\rm max}$ is expected due to the increasing granulation amplitude (see Equation 5.10), but the turnover and spread below 100μHz is evidence of the PDC pipeline removing astrophysical signal. Blue points are the result of work from KASOC (see text).

Figure 5.3 shows the reported CDPP for 13,000 red giants observed by *Kepler*. The reported CDPP appears to show increased scatter and attenuation at $\nu_{\rm max} <$ 100μHz, i.e., in the more evolved stars in the cohort. The level of signal attenuation was explored by Gilliland et al. (2015) and Thompson et al. (2013). Long-period signals were injected into lightcurves, and attempts made to recover them after PDC processing. It was found that signals on timescales longer than a day showed attenuation. The scatter below 100μHz in Figure 5.3 suggests that variability on timescales longer even than only 0.1 days will suffer some signal loss. Gilliland et al. (2015) also note that small-amplitude signals suffer more attenuation, in relative terms, than large-amplitude signals at the same frequency (period).

Taken at face value, Figure 5.3 suggests that some of the low $\nu_{\rm max}$ (larger, more evolved) stars would be ideal for planet searches, since they appear to be photometrically quiet. However the turnover around 100μHz is unphysical, a consequence of

the PDC lightcurve processing (Thompson et al., 2013; Stumpe et al., 2014). This is the primary motivation to formulate an accurate model of the CDPP for evolved stars.

The data plotted in blue are the CDPP values calculated from lightcurves produced by an independent processing of the raw *Kepler* pixel data by the *Kepler* Asteroseismic Science Operations Center (KASOC) pipeline (Handberg & Lund, 2014b). This pipeline was intentionally designed to preserve astrophysical signal on longer timescales, and does not show the same marked attenuation as the PDC data. As we shall now go on to discuss, our simple noise model – which is based on the scaling relations outlined above – is able to reproduce the observed KASOC CDPP values.

5.4 Noise Model

Of the 13,000 stars in Figure 5.3, 6400 were identified as stars ascending the RGB (Elsworth, private comm). For each of these stars we constructed basic model power spectra up to the Nyquist frequency of 283 μHz. The granulation and oscillation power envelope contributions to the spectrum – which below we label as $P_{\rm g}$ and $P_{\rm o}$ – were modelled as in Sections 5.2.1 and 5.2.2, using the measured asteroseismic parameters (Stello et al., 2013a) as input. The flat shot noise contribution $P_{\rm s}$ was modelled according to the upper envelope model described in Jenkins et al. (2010b). The RMS noise per long cadence in the time domain is

$$\sigma_{\rm s} = \sqrt{c + 7 \times 10^7}/c, \tag{5.11}$$

where

$$c = 3.46 \times 10^{0.4 \times (12 - Kp) + 8} \tag{5.12}$$

is the number of detected electrons per long cadence. The flat power-spectral density in the frequency domain then corresponds to:

$$P_{\rm s} = 2 \times 10^{-6} \sigma_{\rm s}^2 \Delta t \tag{5.13}$$

where Δt is the 29.4-minute cadence. Components due to the near-surface magnetic activity were not considered due to the evolved state of these stars. As we shall see below, this assumption appears to be validated by the good match of our model to the observations.

The model estimate of the CDPP may then be constructed as follows

$$\sigma_{\rm CDPP} = \left(\Delta_T \int_0^{\nu_{\rm Nyq}} F(\nu) \times [P_{\rm g} + P_{\rm o} + P_{\rm s}] \right)^{0.5}, \tag{5.14}$$

where Δ_T is the resolution on which the artificial power spectra were computed and $F(\nu)$ represents the bandpass filter response for the model CDPP, which is comprised of high- and low-pass responses. As noted in Gilliland et al. (2011) the high-pass response may be described by a 2-day Savitsky-Golay filter (Savitzky & Golay, 1964), whilst the low-pass response is a 6.5-hr sinc-squared function. The low-pass response ensures that the filter has zeros at harmonics of the 6.5-hr Earth-Sun half-transit duration, so that when constructing the noise metric transit signal is not included as misidentified stellar variability. The high-pass filter suppresses the model power spectral density around zero frequency. The filter has been tested against *Kepler* stars to ensure that the final values are similar to the PDC derived CDPP, for stars where no signal attenuation is occurs.

The attenuation of the signal due to the finite sampling time of *Kepler* is not considered here, due to the negligible influence of the effect around the region of the bandpass filter.

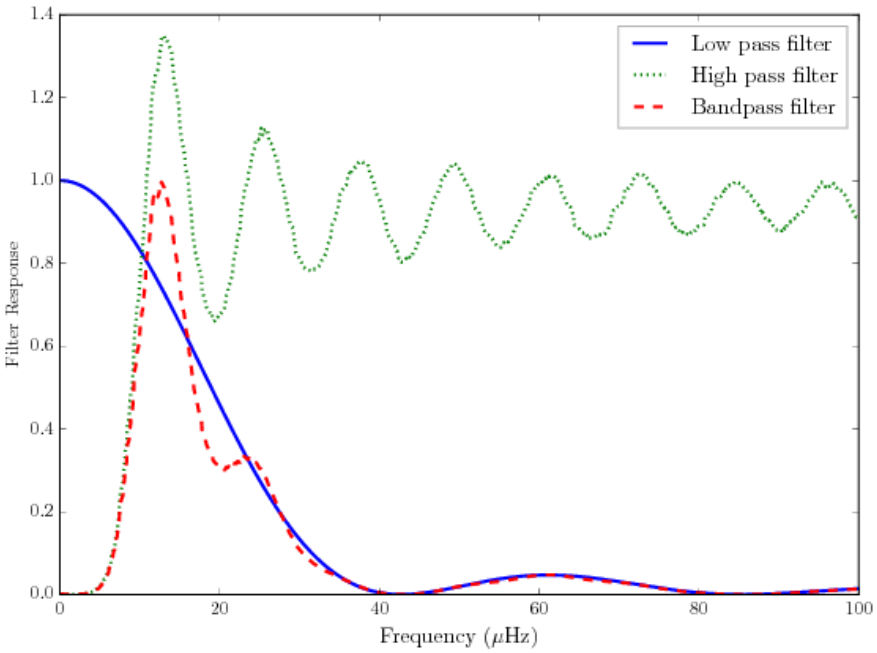

Figure 5.4: Filter response, with the Savitsky-Golay high-pass in green, 6.5-hr sinc-squared in blue, and the combined filter in red.

Figure 5.4 shows the main bandpass of the filter, whilst Figure 5.5 shows the filter imposed on a typical red giant power spectrum to indicate regions of the spectrum captured by the filter. Since the filter has higher-frequency structure, i.e., "ringing", the CDPP of even low-luminosity red giants with $\nu_{\rm max}$ values above 200 μHz will have some contribution from the oscillations. However it should be clear that for low-luminosity red giants the primary contribution to the stellar noise will come from the stellar granulation, with the oscillations being a relatively minor, but not insignificant, contribution.

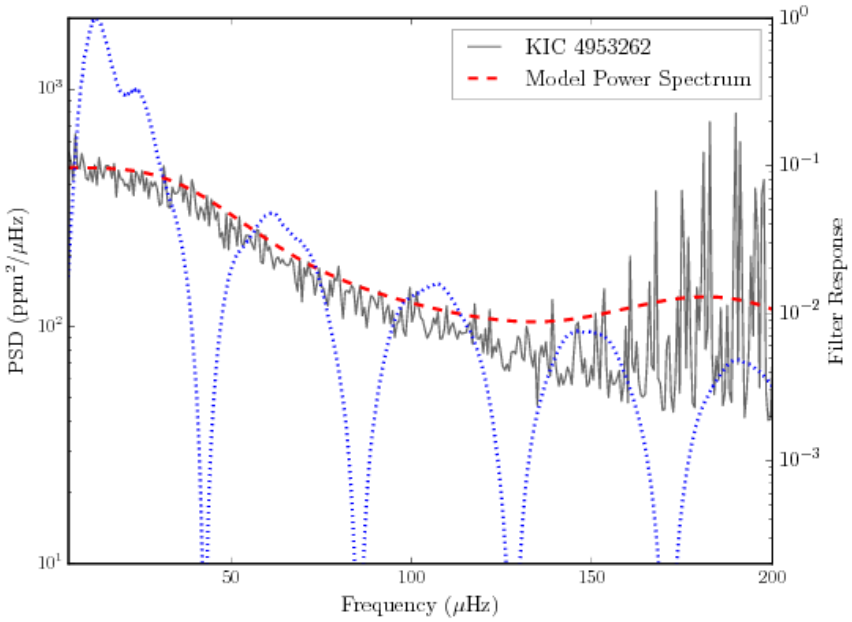

Figure 5.5: Filter response overplotted on KIC 4953262 power spectrum. Clearly most of the signal involved in the construction of the noise metric appears in the region $0 < \nu \lesssim 40\mu$Hz. The filter response is shown on a log scale to emphasise regions of the power spectrum that contribute to the noise metric.

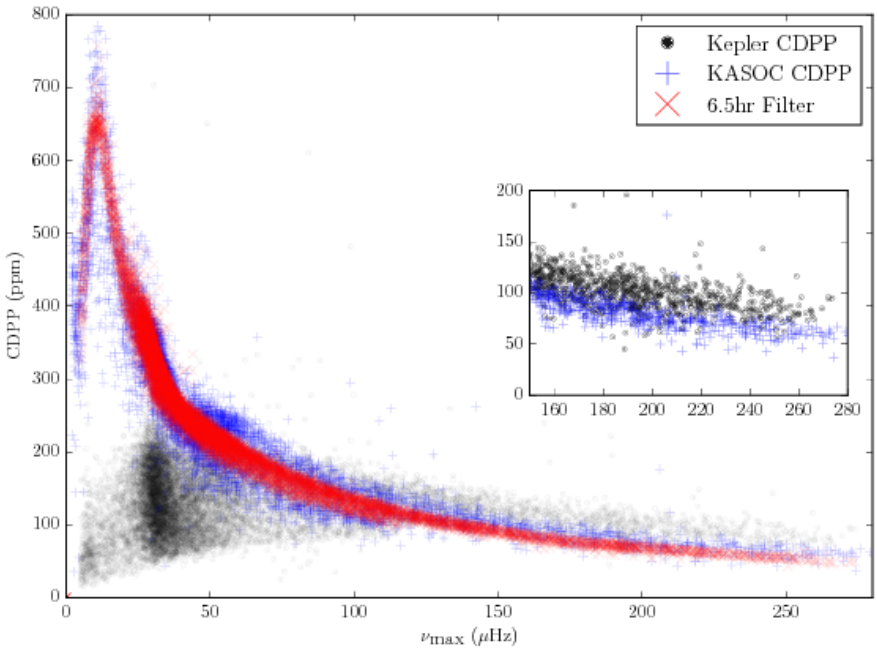

Figure 5.6: The model CDPP shows a strong trend with $\nu_{\rm max}$. Stars at lower $\nu_{\rm max}$ represent larger stars, with larger granulation signal, since the amplitude scales with $\nu_{\rm max}$ (see Eq 5.10). At low frequencies around 10μHz, the contribution from the stellar oscillations is of the same order as the granulation background. The KASOC results are also reproduced and show good agreement with the model results. The inset focuses on the high $\nu_{\rm max}$ ($\nu_{\rm max} > 150\mu$Hz) stars, and shows that the KASOC results show significantly less noise than the PDC derived CDPP.

Figure 5.6 shows the model-estimated CDPP values in red, overlaid on the observed CDPP values from Figure 5.3, (PDC pipeline CDPP values in black and the KASOC pipeline CDPP values in blue). We see good agreement between the model and the observed KASOC pipeline values. This is a clear indication that the model used is sufficiently robust, and additionally that a stellar activity component is not required for these stars. The turnover around 10μHz is due to the oscillation envelope passing through the frequency bandpass of the filter. The additional scatter seen in the KASOC results around 50μHz is due to the presence of RC stars, which do not obey the scaling relations used in construction of power spectra in the same way as stars on the RGB, we therefore removed these stars in the work that follows. The clump stars were also removed due to the assumption that upon ascent up the RGB, any existing low period planetary system will have been engulfed by the star.

As such they are of little relevance when considering the potential planet yield left in *Kepler* data.

Figure 5.7 also demonstrates that the intrinsic stellar oscillations are a key component of the stellar noise for low $\nu_{\rm max}$, high-luminosity RGBs. In the region around the turnover (ν 10μHz) in Figure 5.6, the signal from oscillations dominates by a factor of $\sim$1.5; there is also an enhancement in the oscillation contribution around the first ringing of the filter at 60μHz because this is where the oscillation envelope passes through the filter (with $\nu_{\rm max}$ aligning with a local maximum in the filter bandpass). It is important to note that even when granulation is the dominant noise source, the stellar oscillations remain a significant factor.

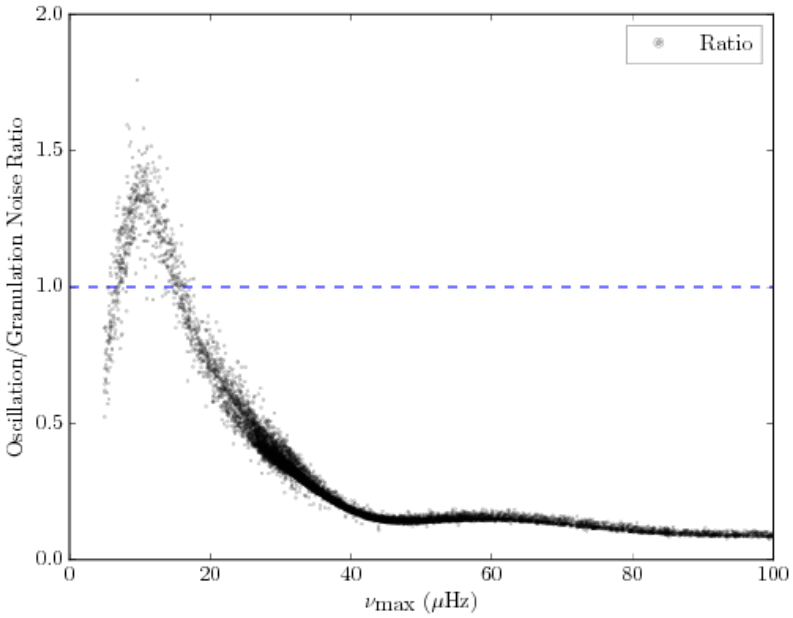

Figure 5.7: The ratio of the contribution to the model CDPP between oscillations and granulation, for 6400 known red giants. The dashed line marks unity.

Finally, it should be noted from Figure 5.6 that low-luminosity giants near the base of the RGB show lower noise in the KASOC pipeline data than in the PDC data, as highlighted in the inset. This would have consequences for the detection yield from these stars.

Having established earlier that our model does a good job of describing the

intrinsic stellar noise for evolved stars, we go on to apply this CDPP to estimate the minimum detectable planet radii around red giant stars in *Kepler* data.

5.4.1 Minimum Radius detection

The canonical *Kepler* CDPP is designed to capture the noise properties around a 6.5-hr timescale, related to the transit timescale of an Earth analogue. But is this filter appropriate to the red-giant case? The basic form of the transit duration equation (Seager & Mallén-Ornelas, 2003; Winn, 2010) is

$$t_{\rm dur} = \frac{R_\star P}{\pi a}\left(1 - b^2\right)^{0.5}, \tag{5.15}$$

where P is the orbital period, a is the semi-major axis, and b is the impact parameter, and there is the implicit assumption of circular orbits. This may be re-written in the form:

$$t_{\rm dur} = \left[\frac{4R_\star^2 a}{GM_\star}\left(1 - b^2\right)\right]^{0.5}. \tag{5.16}$$

The maximum transit duration (for $b = 0$) is therefore proportional to $R_\star a^{0.5}$. In the red giant case this can potentially vary anywhere from an Earth-analogue duration (e.g., Kepler-56b, a short-period planet around another low luminosity red giant, with a transit duration of 13.3hrs) up to durations exceeding one day (e.g., wide orbits around low-luminosity RGB stars, or closer orbits around more evolved giants).

Since the range of possible transit durations is so broad for stars ascending the RGB, the noise properties being considered need to capture the stellar variability over the relevant timescales. A 6.5-hr filter turns out to be more appropriate than it might at first seem. To explain why, we return to Figure 5.4. The maximum of the bandpass of the filter is at 12.5μHz, a timescale of around 22 hours. The half power points of the bandpass lie at 9.2μHz and 16.6μHz, corresponding to 30.2 and 16.7 hours respectively. There is also a significant contribution to the

bandpass at even shorter periods (i.e., note the secondary peak at around 25μHz, which corresponds to about 11 hours). As we shall see below, because the chances of detecting planets around very evolved red giants – where transit durations would be much longer than a day – are so low, our numbers above indicate that the current filter already does a reasonable job of capturing the necessary timescales of interest for transits of lower luminosity red giants.

The CDPP values from our model as inputs to calculate a minimum detectable planet radius for each of the *Kepler* RGB stars, according to Equation 1 in Howard et al. (2012):

$$R_{\rm min} = R_\star \left({\rm SNR} \times \sigma_{\rm CDPP}\right)^{1/2} \left(\frac{6.5{\rm hr}}{n_{\rm tr}\, t_{\rm dur}}\right)^{1/4}, \tag{5.17}$$

The assumed detection signal-to-noise ratio was taken as SNR=10, this value is adopted as a "secure" detection threshold. This is stronger than the 7.1σ threshold used in the *Kepler* mission for transit detections (Jenkins et al., 2010a) to ensure these planets would be detected (see Borucki et al. 2011; Howard et al. 2012; Fressin et al. 2013; Christiansen et al. 2013) .

The transit duration was calculated according to Equation 5.15, taking $b = 0$; the stellar radius was taken to be the asteroseismically determined value from Equation 5.5; and n, the number of observed transits, was assumed to equal $n =$ 4yr/Period(yr), rounded down to the nearest integer. The factor of 6.5 in Equation 5.17 accounts for the timescale on which the CDPP is calculated compared to the transit duration. It should also be noted that the 4-year factor in the number of transits assumes all stars were observed continuously for the entire duration of the *Kepler* mission, any missing transits would increase the minimum detectable radius.

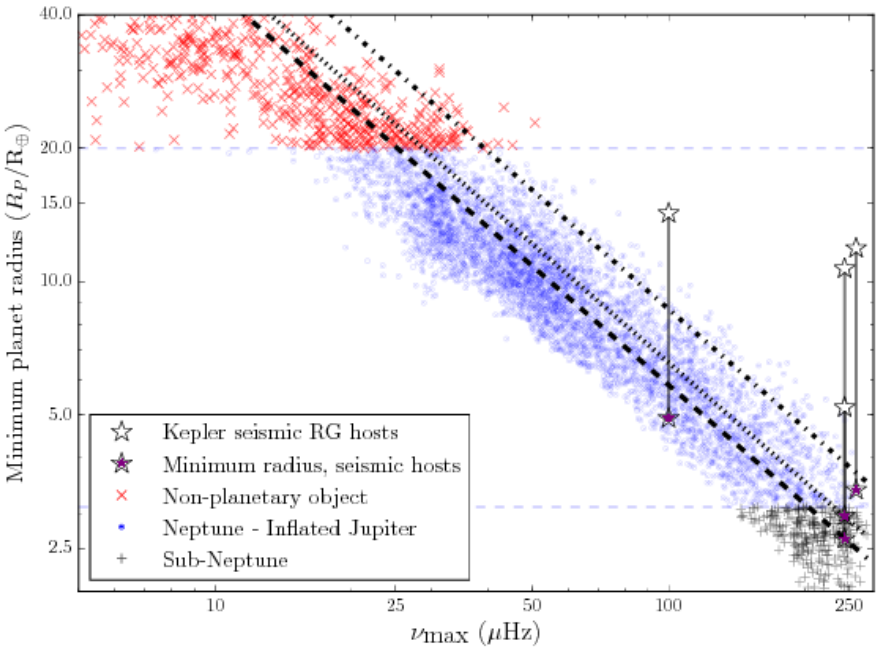

Figure 5.8: Minimum detection radius in Earth radii, for the 6400 *Kepler* stars. Clearly this is a strong function of $\nu_{\rm max}$, in this case a proxy for stellar radius. The diagonal lines are fits to a power-law relation between $\nu_{\rm max}$ and $R_{\rm min}$ for assumed periods of 10 days (dashed), 20 days (dotted) and 100 days (dot-dashed). Radii of known planets (open stars) and the corresponding estimated minimum radii (filled stars) for the same systems are also shown, connected by vertical black lines. Points and crosses indicate the minimum radii for illustrative distribution described in the text

The diagonal lines in Figure 5.8 show power-law fits to $\nu_{\rm max}$ of the calculated minimum detection radii $R_{\rm min}$ of the 6400 *Kepler* stars, assuming fixed orbital periods of 10 days (dashed line), 20 days (dotted line) and 100 days (dot-dashed line), respectively. The vertical offset seen between the diagonal lines is due to the reduced number of transits seen for longer period planets. The minimum radii here were calculated using the model CDPP predictions. But we could also have used the KASOC CDPP data, which give very similar results. The true, underlying period distribution for planets orbiting evolved hosts is of course very poorly constrained. For illustrative purposes only, we have also calculated minimum radii using an underlying distribution that is consistent with results on confirmed *Kepler* planets, with data taken from the NASA Exoplanet Archive (Akeson et al., 2013b) [1]. These

[1] http://exoplanetarchive.ipac.caltech.edu/

data are well described by a log-normal distribution, with the underlying normal distribution having a mean and standard deviation of 2.47 and 1.23 in $\log_e P$. The results are plotted on Figure 5.8, blue dots are super-Earth to Jupiter sized objects, whilst red crosses are objects with minimum radii greater than that which is feasible for a planet. Black crosses indicate a minimum radii of less than the radius of Neptune.

Figure 5.8 shows that even the most inflated hot-Jupiter planets will be undetectable around high RGB stars (i.e., stars with low $\nu_{\rm max}$). This is due to the large radii of these stars, and the resulting small transit depths. Due to the inflated nature of the stars themselves, finding Earth-like planets at high SNR will most likely prove unfeasible across the entire population of evolved stars. For low-luminosity red giants, there is the potential to reach super-Earth sized planets. However it is apparent that the focus for planets around red-giant hosts should be Neptune to Jupiter-sized giant planets.

Radii of known planets (open stars) and the estimated minimum radii (filled stars) for the same systems are also shown on Figure 5.8, connected by vertical black lines. As can also be seen, the currently known transiting planets around evolved hosts sit on the upper edge of the distribution in planet radius and $\nu_{\rm max}$. The lack of detections around low-$\nu_{\rm max}$ stars suggests that any systematic search for planets around evolved hosts should instead concentrate on low-luminosity RGB stars. We note that we might expect radii for actual detections to cover a range of radii at and above the minimum radii and this is what we see in Figure 5.8, albeit for a very small sample.

Figure 5.9 shows the same minimum radius calculation using the current *Kepler* PDC derived CDPP values. These results would (incorrectly) suggest that planets could be detected around low $\nu_{\rm max}$ stars due to the aforementioned attenuation of intrinsic stellar signals on long timescales. For the high $\nu_{\rm max}$ stars, the minimum radii are also larger than the results for the for updated noise model CDPP described

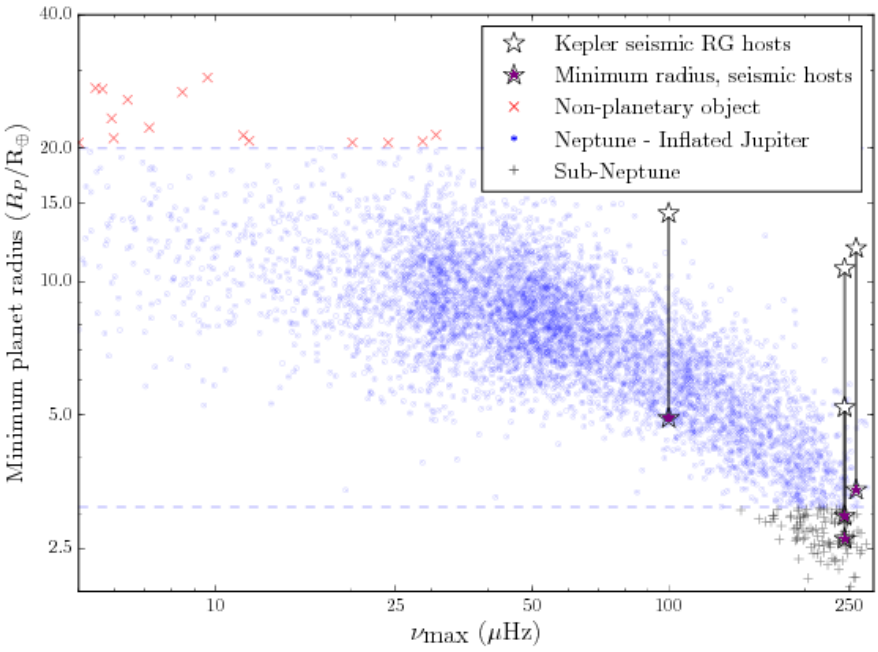

Figure 5.9: Minimum detection radius in Earth radii, if the PDC CDPP results are used. Again the 20 day distribution has been used here. Clearly the PDC results would suggest that planets would be detectable around low $\nu_{\rm max}$ stars, but this is purely an effect of the PDC processing producing anomalously low CDPP values.

here.

As stars ascend the RGB, planets on short periods are rapidly engulfed by the expanding star. Additionally the tidal decay timescale decreases for evolved stars (Schlaufman & Winn, 2013), e.g., the Kepler-56 system, where the planets are likely to be engulfed within ∼100 Myr (Li et al., 2014). Even without consideration of tidal decay, for the case of evolved RGB hosts, planets on short periods, and many cases in the *Kepler* period distribution described above, would have to exist inside the stellar envelope (these cases have been removed from Figure 5.8).

5.4.2 Transit Injection Test

To ensure the results for the minimum detection radius in Figure 5.8 are reasonable, a sensible test was to inject transit signals into real *Kepler* data and attempt to recover the transit signal. As an example a red giant with similar stellar and asteroseismic properties ($\nu_{\rm max} = 255\mu$Hz) to Kepler-56, but with no known transits, was

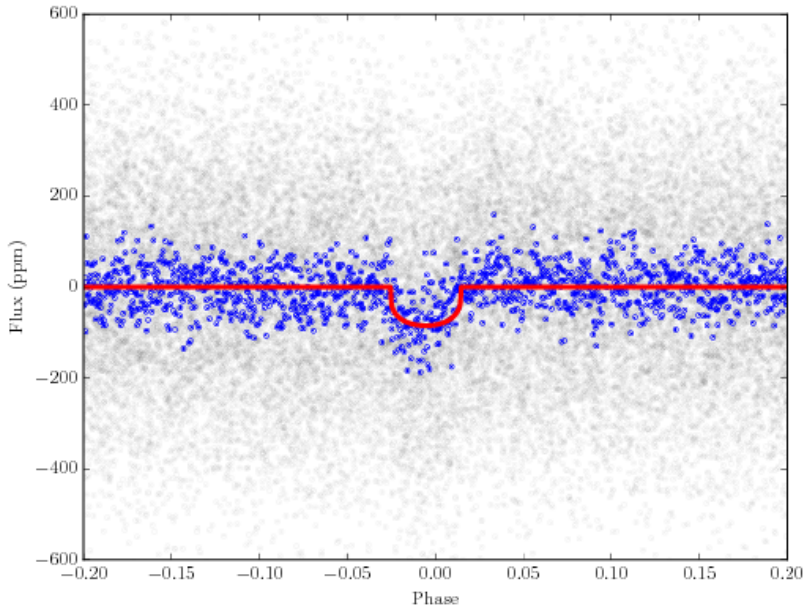

Figure 5.10: Injected transit into *Kepler* detrended lightcurve, folded on the 20 day period of injected planet (black). Also plotted is binned lightcurve, folded on period (blue), along with model for the planet injection (red)

selected and a transit signal injected into the detrended lightcurve. A planet with the minimum detection radius ($R_{\rm min} = 2.25R_{\oplus}$, for a planet on a 20 day orbit, at SNR=10) was injected into the lightcurve on a 20 day orbit, and was recovered using a box-least squares algorithm[2] (Kovács et al., 2002a) at the required SNR threshold. Figure 5.10 shows the injected transit in the lightcurve, folded on the period of the injected planet (grey points). Also shown is the re-binned lightcurve after folding on the period of the planet (blue points) and the model for the injected transit (red line).

This is of particular importance since the current sample of known transiting planets around evolved hosts in the NASA Exoplanet Archive all have a detection SNR$\geq$ 15. Returning once more to Kepler-56, the detection ratios in that system are 63 and 44, for planets b and c respectively. However as the BLS injection test shows, smaller planets are recoverable in the data. The transit injection performed here,

[2]python implementation of BLS created by Dan Foreman-Mackey and Ruth Angus https://github.com/dfm/python-bls

along with the minimum planet radii calculated above, suggest that Neptune-sized planets should be detectable in the *Kepler* lightcurves of low-luminosity, red-giant stars, if they are present. As of yet, a dedicated survey for such planets has not been carried out in a systematic fashion.

5.5 Conclusions

In this chapter we have presented a simple model to describe the noise properties of evolved stars as relevant to transit searches for exoplanets. Our model predictions of the commonly-used *Kepler* CDPP noise metric is dominated for evolved stars by granulation and oscillations. It includes a significant contribution from stellar oscillations, with the solar-like oscillations representing the dominant noise source for any photometric survey of stars near the tip of the red-giant branch. Importantly, our model also recovers the appropriate noise signatures for highly evolved stars, a feature not shared by current *Kepler* results. This noise model may be applied to the predictions of the noise properties of evolved stars for the upcoming TESS and PLATO missions.

As a simple application of this updated CDPP, we also estimated minimum detectable planet radii for low-luminosity red giants, for different assumed orbital periods. The results suggest that Neptune-sized planets on short-period ($P \leq 20$ days) orbits should be detectable in the *Kepler* data. We advocate a detailed search for planets around red giants. Giant planets around evolved stars will also be detectable in lightcurves from the upcoming TESS mission (Ricker et al., 2014) as well as the ongoing K2 mission, which has already targeted a dedicated sample of several thousand low-luminosity red giants to detect giant planets (Huber, 2015; Grunblatt et al., 2016, 2017) .

6 Conclusion

In this thesis I have discussed various aspects of evolved stars, and the planets or binary stars that orbit them. Through the use of asteroseismology, studying the solar-like oscillations of evolved red giant and red clump stars, and complementary data sources such as spectroscopy and parallaxes, the fundamental properties of stars may be estimated. Whilst the primary focus of investigation has been studying the host star to determine the properties of any exoplanet orbiting it, ensemble investigations of host and non-host stars have also been undertaken to understand the distributions in stellar properties of these classes of stars.

6.1 Asteroseismology as a tool

Using the so-called global asteroseismic parameters $\nu_{\rm max}$ and $\Delta\nu$, I have studied the masses of evolved exoplanet hosts, both in an ensemble fashion when studying "Retired A Stars" in Chapter 2, and on an individual basis when considering the discovery of individual systems of interest in Chapter 3. For the ensemble of Retired A Stars, the asteroseismic masses were not found to be significantly lower than the masses reported alongside the relevant planet discoveries. However, offsets in mass were found. After thorough investigation it was concluded that underestimated uncertainties on other parameters such as [Fe/H], $T_{\rm eff}$ and luminosity, not only biased the recovered mass, but also produced underestimated uncertainties. With updated parallaxes expected from *Gaia* for all the stars in this ensemble, combined with asteroseismic observations from TESS for many of the evolved radial velocity host stars in the "Retired A Star" ensemble, this work can be expanded upon in the future.

The problem of biased mass estimates for evolved stars using differing constraints is not limited to just planet hosts however, and in a general fashion understanding the impact of differing constraints during the recovery of stellar properties from models is important.

6.2 Evolved hosts and binaries

Two evolved transiting/eclipsing systems observed by *Kepler* are considered in detail in Chapter 3. In both cases asteroseismology was utilised during stellar modelling to recover the stellar properties. Additionally, asteroseismology was able to constrain the mean stellar density, which when incorporated in the simultaneous lightcurve and radial velocity modelling, was able to place additional constraint on the system parameters.

The first system, KOI-6194, is a member of a rare class of planets. The *Kepler* mission has detected a handful of giant planets transiting red giant host stars on relatively short period orbits ($P < 100$ days). Such systems have not been detected by radial velocity surveys, raising questions of differences in the populations of the observed stars.

For KOI-6194, there was insufficient radial velocity data to fully constrain the orbital eccentricity. The orbiting planet is a gas giant of radius $R_P = 0.88 \pm 0.04 \mathrm{R_J}$. An upper limit can be placed on the planet mass of $M < 0.9 \pm 0.1 \mathrm{M_J}$. The planet, on a 42.3 day orbit, will be consumed by the expanding star as it ascends the red giant branch in $\lesssim 140$ Myrs. At this point the planet will either be destroyed, or may trigger the ejection of the stellar envelope, to form a highly unusual sdB star.

The other system of note was KOI-3890, a red giant primary star in a highly eccentric ($e > 0.6$) eclipsing binary. The secondary is an M dwarf of mass $M = 0.23 \pm 0.01 \mathrm{M_\odot}$. One particular feature of interest in this system is evidence for tidal distortion of the primary star by the secondary star, inducing a "heartbeat" signal in the lightcurve of the primary star. This is evidence that the two stars have begun

to interact tidally as the red giant primary expands towards the orbital radius of the primary. As with KOI-6194, this system could be the progenitor of an sdB system. The current separation of the two stars at periastron is insufficient to prevent the M dwarf from being consumed by the expanding primary.

While these two systems were identified to be of interest in this thesis, other KOIs with evolved primary stars remain to have follow-up observations performed. It is likely there are still red giant hosts to be discovered in *Kepler* and K2 data. One focus of the soon to be launched TESS mission is the discovery of such systems, along with attempting to detect any transits of already known planets detected via radial velocity observations. Related to this is understanding the underlying cause of why radial velocity surveys do not find the short period planets that transit surveys detect.

6.3 Other methods

Whilst asteroseismology has been the main tool used in this thesis to analysis stars, such data are not always available, as is the case in Chapter 4, where high resolution spectroscopy was utilised to infer the spectroscopic parameters of many bright giant stars, both planet hosts and non-hosts. With the sample of hosts and non-hosts available, I do not find significant evidence to support the theory currently in discussion in the literature, that evolved planets hosts as an ensemble exist at higher metallicities than non-hosts as an extension of the established observations around dwarf stars. When performing a K-S test to find the probability that the two metallicity distributions, for the host and field stars, are drawn from the same population we recover a probability of $P = 33.2\%$ when subgiants are removed from the population. Our results are in agreement with Mortier et al. (2013), though we note the discussion on this issue is ongoing, while potential biases in the target selection in radial velocity surveys may have an impact on inferred results. Additionally a larger sample of homogeneously observed and analysed spectra may be required.

When our spectroscopic values are used to recover new estimates of fundamental stellar properties, differences are found in comparison to other literature values, though not at a significant level. These differences can mostly be attributed to the choice of stellar models used during the recovery process. Asteroseismic observations for many of these stars will soon be available with TESS. This will allow for additional constraint to be placed on the masses of these stars.

Other data utilised during this thesis has primarily been stellar luminosities, derived from parallax measurements. Where relevant both *Hipparcos* and *Gaia* parallaxes have been used. With the expected end of mission parallax measurements precision from *Gaia* predicted to be significantly higher than available precisions, stellar luminosity measurements will in turn, have higher precisions, and as such, greater constraint on inferred stellar properties. In addition to parallaxes, stellar extinctions must be utilised in the recovery of stellar luminosity. The increasing availability of 3D dustmaps for the Milky Way, will allow for extinction to be accurately accounted for when calculating luminosities.

6.4 Future Missions

Whilst the *Kepler* mission has no doubt drastically changed current knowledge of exoplanets and the properties of evolved exoplanetary systems, there is much left to be discovered. The upcoming NASA TESS mission (Ricker et al., 2014) will conduct an all sky survey looking for short period transiting planets. One subset of targets of particular interest to asteroseismology are red giant stars, already known to host exoplanets through radial velocity measurements, but that have not yet been studied to detect solar-like oscillations. Approximately 100 such stars will be bright enough to have detectable oscillations when observed by TESS (Campante et al., 2016). Additionally, the mission should also detect additional transiting giant planets around giant stars, similar to KOI-6194 thereby extending the sample discussed in Chapter 3. Further missions, including the ESA *PLATO* mission (Rauer

et al., 2014) will extend the work of *Kepler*, with continuous, long term observations of several fields of view across the sky, will approximately 50% sky coverage. In addition to this, the ESA *Gaia* mission will provide precise parallaxes for $\sim 1 \times 10^9$ stars in the Milky Way, including asteroseismic red giants, allowing additional constraints on their fundamental properties (and any planets orbiting them).

Bibliography

Aceituno J., et al., 2013, A&A, 552, A31

Adamów M., Niedzielski A., Villaver E., Nowak G., Wolszczan A., 2012a, ApJ, 754, L15

Adamów M., Niedzielski A., Villaver E., Nowak G., Wolszczan A., 2012b, ApJ, 754, L15

Akeson R. L., et al., 2013a, PASP, 125, 989

Akeson R. L., et al., 2013b, PASP, 125, 989

Alcalá J. M., Biazzo K., Covino E., Frasca A., Bedin L. R., 2011, A&A, 531, L12

Anderson E. R., Duvall Jr. T. L., Jefferies S. M., 1990, ApJ, 364, 699

Angulo C., et al., 1999, Nuclear Physics A, 656, 3

Arentoft T., et al., 2008, ApJ, 687, 1180

Baglin A., et al., 2006, in 36th COSPAR Scientific Assembly.

Bailes M., et al., 2011, Science, 333, 1717

Ballard S., et al., 2011, ApJ, 743, 200

Barclay T., Endl M., Huber D., Foreman-Mackey D., Cochran W. D., MacQueen P. J., Rowe J. F., Quintana E. V., 2015, ApJ, 800, 46

Barnes J. W., 2007, PASP, 119, 986

Barnes R., Jackson B., Raymond S. N., West A. A., Greenberg R., 2009, ApJ, 695, 1006

Baruteau C., Masset F., 2013, in Souchay J., Mathis S., Tokieda T., eds, Lecture Notes in Physics, Berlin Springer Verlag Vol. 861, Lecture Notes in Physics, Berlin Springer Verlag. p. 201 (arXiv:1203.3294), doi:10.1007/978-3-642-32961-6˙6

Bastien F. A., Stassun K. G., Basri G., Pepper J., 2013, Nature, 500, 427

Batalha N. M., 2014, Proceedings of the National Academy of Science, 111, 12647

Batalha N. M., et al., 2010, ApJ, 713, L103

Batygin K., Laughlin G., 2015, Proceedings of the National Academy of Science, 112, 4214

Baudin F., et al., 2011, A&A, 529, A84

Beck P. G., et al., 2011, Science, 332, 205

Beck P. G., et al., 2014, A&A, 564, A36

Becker J. C., Vanderburg A., Adams F. C., Rappaport S. A., Schwengeler H. M., 2015, ApJ, 812, L18

Bedding T. R., Kjeldsen H., 2003, PASA, 20, 203

Bedding T. R., et al., 2010, ApJ, 713, L176

Bedding T. R., et al., 2011, Nature, 471, 608

Belkacem K., Goupil M. J., Dupret M. A., Samadi R., Baudin F., Noels A., Mosser B., 2011, A&A, 530, A142

Blanco-Cuaresma S., et al., 2016, in 19th Cambridge Workshop on Cool Stars, Stellar Systems, and the Sun (CS19). p. 22 (arXiv:1609.08092), doi:10.5281/zenodo.155115

Bonfanti A., Ortolani S., Piotto G., Nascimbeni V., 2015, A&A, 575, A18

Bonfanti A., Ortolani S., Nascimbeni V., 2016, A&A, 585, A5

Borucki W. J., et al., 2010, Science, 327, 977

Borucki W. J., et al., 2011, ApJ, 736, 19

Borucki W. J., et al., 2012, ApJ, 745, 120

Bossini D., et al., 2015, MNRAS, 453, 2290

Bovy J., Rix H.-W., Green G. M., Schlafly E. F., Finkbeiner D. P., 2016, ApJ, 818, 130

Bowler B. P., et al., 2010, ApJ, 709, 396

Bressan A., Marigo P., Girardi L., Salasnich B., Dal Cero C., Rubele S., Nanni A., 2012, MNRAS, 427, 127

Brown T. M., Gilliland R. L., Noyes R. W., Ramsey L. W., 1991, ApJ, 368, 599

Brown T. M., Latham D. W., Everett M. E., Esquerdo G. A., 2011, AJ, 142, 112

Butler R. P., et al., 2017, AJ, 153, 208

Cameron A., Truran J., 1977, Icarus, 30, 447

Campante T. L., et al., 2015a, ApJ, 799, 170

Campante T. L., et al., 2015b, ApJ, 799, 170

Campante T. L., et al., 2016, ApJ, 830, 138

Campante T. L., et al., 2017, MNRAS, 469, 1360

Campbell B., Walker G. A. H., Yang S., 1988, ApJ, 331, 902

Carlberg J. K., Majewski S. R., Arras P., 2009, ApJ, 700, 832

Carlberg J. K., Smith V. V., Cunha K., Majewski S. R., Rood R. T., 2010, ApJ, 723, L103

Chaplin W. J., Miglio A., 2013, ARA&A, 51, 353

Chaplin W. J., et al., 2014, ApJS, 210, 1

Chaplin W. J., et al., 2015, PASP, 127, 1038

Charbonneau D., Brown T. M., Latham D. W., Mayor M., 2000, ApJ, 529, L45

Charpinet S., et al., 2011, Nature, 480, 496

Choi J., Dotter A., Conroy C., Cantiello M., Paxton B., Johnson B. D., 2016, ApJ, 823, 102

Christensen-Dalsgaard J., 1998, Ap&SS, 261, 1

Christiansen J. L., et al., 2012, PASP, 124, 1279

Christiansen J. L., et al., 2013, ApJS, 207, 35

Ciceri S., Lillo-Box J., Southworth J., Mancini L., Henning T., Barrado D., 2015, A&A, 573, L5

Claret A., Bloemen S., 2011, A&A, 529, A75

Claret A., Gimenez A., Cunha N. C. S., 1995, A&A, 299, 724

Cumming A., Marcy G. W., Butler R. P., 1999, ApJ, 526, 890

Davies G. R., Miglio A., 2016, Astronomische Nachrichten, 337, 774

Davies G. R., Handberg R., Miglio A., Campante T. L., Chaplin W. J., Elsworth Y., 2014, MNRAS, 445, L94

Davies G. R., et al., 2017, A&A, 598, L4

De Ridder J., Molenberghs G., Eyer L., Aerts C., 2016, A&A, 595, L3

Deheuvels S., Brandão I., Silva Aguirre V., Ballot J., Michel E., Cunha M. S., Lebreton Y., Appourchaux T., 2016, A&A, 589, A93

Désert J.-M., et al., 2015, ApJ, 804, 59

Döllinger M. P., Hatzes A. P., Pasquini L., Guenther E. W., Hartmann M., Girardi L., Esposito M., 2007, A&A, 472, 649

Döllinger M. P., et al., 2011, in Schuh S., Drechsel H., Heber U., eds, American Institute of Physics Conference Series Vol. 1331, American Institute of Physics Conference Series. pp 79–87 (`arXiv:1102.0499`), doi:10.1063/1.3556186

Doyle L. R., et al., 2011, Science, 333, 1602

Eggenberger P., et al., 2017, A&A, 599, A18

Ehrenreich D., et al., 2015, Nature, 522, 459

Ferguson J. W., Alexander D. R., Allard F., Barman T., Bodnarik J. G., Hauschildt P. H., Heffner-Wong A., Tamanai A., 2005, ApJ, 623, 585

Fernandez-Villacanas J. L., Rego M., Cornide M., 1990, AJ, 99, 1961

Feulner G., 2012, Reviews of Geophysics, 50, RG2006

Fischer D. A., Valenti J., 2005, ApJ, 622, 1102

Fischer D. A., Marcy G. W., Spronck J. F. P., 2014, ApJS, 210, 5

Flower P. J., 1996, ApJ, 469, 355

Foreman-Mackey D., 2016, The Journal of Open Source Software, 24

Foreman-Mackey D., Hogg D. W., Lang D., Goodman J., 2013, PASP, 125, 306

Fortney J. J., Marley M. S., Barnes J. W., 2007, ApJ, 659, 1661

Fressin F., et al., 2013, ApJ, 766, 81

Fuller J., Cantiello M., Stello D., Garcia R. A., Bildsten L., 2015, Science, 350, 423

Gaidos E., Mann A. W., 2013, ApJ, 762, 41

Gatewood G., Eichhorn H., 1973, AJ, 78, 769

Gaudi B. S., Seager S., Mallen-Ornelas G., 2005, ApJ, 623, 472

Gaulme P., McKeever J., Rawls M. L., Jackiewicz J., Mosser B., Guzik J. A., 2013, ApJ, 767, 82

Gaulme P., et al., 2016, ApJ, 832, 121

Ghezzi L., Johnson J. A., 2015, ApJ, 812, 96

Ghezzi L., do Nascimento Jr. J.-D., Johnson J. A., 2015, in van Belle G. T., Harris H. C., eds, Cambridge Workshop on Cool Stars, Stellar Systems, and the Sun Vol. 18, 18th Cambridge Workshop on Cool Stars, Stellar Systems, and the Sun. pp 743–748 (`arXiv:1408.3143`)

Giguere M. J., Fischer D. A., Payne M. J., Brewer J. M., Johnson J. A., Howard A. W., Isaacson H. T., 2015, ApJ, 799, 89

Gilliland R. L., et al., 2010, PASP, 122, 131

Gilliland R. L., et al., 2011, ApJS, 197, 6

Gilliland R. L., Chaplin W. J., Jenkins J. M., Ramsey L. W., Smith J. C., 2015, AJ, 150, 133

Gizon L., Solanki S. K., 2003, The Astrophysical Journal, 589, 1009

Glaspey J. W., Pritchet C. J., Stetson P. B., 1994, AJ, 108, 271

Green G. M., et al., 2015, ApJ, 810, 25

Grether D., Lineweaver C. H., 2006, ApJ, 640, 1051

Grevesse N., Noels A., 1993, Physica Scripta Volume T, 47, 133

Grunblatt S. K., Howard A. W., Haywood R. D., 2015, ApJ, 808, 127

Grunblatt S. K., et al., 2016, AJ, 152, 185

Grunblatt S. K., et al., 2017, AJ, 154, 254

Grundahl F., Christensen-Dalsgaard J., Gråe Jørgensen U., Frandsen S., Kjeldsen H., Kjærgaard Rasmussen P., 2011, in Journal of Physics Conference Series. p. 012083, doi:10.1088/1742-6596/271/1/012083

Grundahl F., et al., 2017, ApJ, 836, 142

Guggenberger E., Hekker S., Basu S., Bellinger E., 2016, MNRAS, 460, 4277

Handberg R., Campante T. L., 2011, A&A, 527, A56

Handberg R., Lund M. N., 2014a, MNRAS, 445, 2698

Handberg R., Lund M. N., 2014b, MNRAS, 445, 2698

Harvey J., 1985, in Rolfe E., Battrick B., eds, ESA Special Publication Vol. 235, Future Missions in Solar, Heliospheric & Space Plasma Physics.

Hatzes A. P., et al., 2018, preprint, (arXiv:1801.05239)

Hekker S., Meléndez J., 2007, A&A, 475, 1003

Hekker S., et al., 2010, MNRAS, 402, 2049

Hekker S., et al., 2011a, MNRAS, 414, 2594

Hekker S., et al., 2011b, MNRAS, 414, 2594

Hekker S., Elsworth Y., Mosser B., Kallinger T., Basu S., Chaplin W. J., Stello D., 2013, A&A, 556, A59

Hekker S., Elsworth Y., Angelou G. C., 2017, preprint, (arXiv:1712.05430)

Hjørringgaard J. G., Silva Aguirre V., White T. R., Huber D., Pope B. J. S., Casagrande L., Justesen A. B., Christensen-Dalsgaard J., 2016, MNRAS,

Høg E., et al., 2000, A&A, 355, L27

Howard A. W., et al., 2010, Science, 330, 653

Howard A. W., et al., 2012, ApJS, 201, 15

Howell S. B., et al., 2014, PASP, 126, 398

Huang C., Wu Y., Triaud A. H. M. J., 2016, ApJ, 825, 98

Huber D., 2015, preprint, (arXiv:1511.07441)

Huber D., Stello D., Bedding T. R., Chaplin W. J., Arentoft T., Quirion P.-O., Kjeldsen H., 2009, Communications in Asteroseismology, 160, 74

Huber D., et al., 2010, ApJ, 723, 1607

Huber D., et al., 2012, ApJ, 760, 32

Huber D., et al., 2013a, Science, 342, 331

Huber D., et al., 2013b, ApJ, 767, 127

Huber D., et al., 2014, ApJS, 211, 2

Huber D., et al., 2016, ApJS, 224, 2

Huber D., et al., 2017, preprint, (arXiv:1705.04697)

Iglesias C. A., Rogers F. J., 1996, ApJ, 464, 943

Isaacson H., Fischer D., 2010, ApJ, 725, 875

Jenkins J. M., et al., 2010a, ApJ, 713, L87

Jenkins J. M., et al., 2010b, ApJ, 713, L120

Jofré E., Petrucci R., Saffe C., Saker L., de la Villarmois E. A., Chavero C., Gómez M., Mauas P. J. D., 2015a, A&A, 574, A50

Jofré E., Petrucci R., García L., Gómez M., 2015b, A&A, 584, L3

Johnson J. A., Marcy G. W., Fischer D. A., Henry G. W., Wright J. T., Isaacson H., McCarthy C., 2006, ApJ, 652, 1724

Johnson J. A., et al., 2007a, ApJ, 665, 785

Johnson J. A., Butler R. P., Marcy G. W., Fischer D. A., Vogt S. S., Wright J. T., Peek K. M. G., 2007b, ApJ, 670, 833

Johnson J. A., Marcy G. W., Fischer D. A., Wright J. T., Reffert S., Kregenow J. M., Williams P. K. G., Peek K. M. G., 2008, ApJ, 675, 784

Johnson J. A., Howard A. W., Bowler B. P., Henry G. W., Marcy G. W., Wright J. T., Fischer D. A., Isaacson H., 2010a, PASP, 122, 701

Johnson J. A., Aller K. M., Howard A. W., Crepp J. R., 2010b, PASP, 122, 905

Johnson J. A., et al., 2011, ApJS, 197, 26

Johnson J. A., et al., 2014, ApJ, 794, 15

Jones M. I., Jenkins J. S., Rojo P., Melo C. H. F., 2011, A&A, 536, A71

Jones M. I., et al., 2016, A&A, 590, A38

Kallinger T., et al., 2014, A&A, 570, A41

Kaltenegger L., Traub W. A., 2009, ApJ, 698, 519

Kjeldsen H., Bedding T. R., 1995, A&A, 293

Kjeldsen H., Bedding T. R., Viskum M., Frandsen S., 1995, AJ, 109, 1313

Klein B., Jura M., Koester D., Zuckerman B., Melis C., 2010, ApJ, 709, 950

Knutson H. A., Charbonneau D., Noyes R. W., Brown T. M., Gilliland R. L., 2007, ApJ, 655, 564

Koch D. G., et al., 2010, ApJ, 713, L79

Kovács G., Zucker S., Mazeh T., 2002a, A&A, 391, 369

Kovács G., Zucker S., Mazeh T., 2002b, A&A, 391, 369

Kreidberg L., 2015, PASP, 127, 1161

Krishna Swamy K. S., 1966, ApJ, 145, 174

Kulkarni S. R., 1997, Science, 276, 1350

Kumar S. S., 1963, ApJ, 137, 1121

Kumar P., Ao C. O., Quataert E. J., 1995, ApJ, 449, 294

Kurucz R. L., 1993, SYNTHE spectrum synthesis programs and line data

Kuszlewicz J. S., 2017, PhD thesis, University of Birmingham

Kuzuhara M., et al., 2013, ApJ, 774, 11

Lagarde N., Bossini D., Miglio A., Vrard M., Mosser B., 2016, MNRAS, 457, L59

Larson R. B., 1969, MNRAS, 145, 271

Latham D. W., Stefanik R. P., Mazeh T., Mayor M., Burki G., 1989, Nature, 339, 38

Laughlin G., Bodenheimer P., Adams F. C., 1997, ApJ, 482, 420

Lee B.-C., Mkrtichian D. E., Han I., Park M.-G., Kim K.-M., 2012, A&A, 548, A118

Lee B.-C., Han I., Park M.-G., Mkrtichian D. E., Hatzes A. P., Kim K.-M., 2014, A&A, 566, A67

Leitzinger M., et al., 2011, Planet. Space Sci., 59, 1472

Li G., Naoz S., Valsecchi F., Johnson J. A., Rasio F. A., 2014, ApJ, 794, 131

Lillo-Box J., et al., 2014a, A&A, 562, A109

Lillo-Box J., et al., 2014b, A&A, 562, A109

Lillo-Box J., Barrado D., Mancini L., Henning T., Figueira P., Ciceri S., Santos N., 2015, A&A, 576, A88

Lindegren L., et al., 2016, preprint, (arXiv:1609.04303)

Lissauer J. J., 1993, ARA&A, 31, 129

Lloyd J. P., 2011, ApJ, 739, L49

Lopez E. D., Fortney J. J., 2016, ApJ, 818, 4

Lund M. N., Handberg R., Davies G. R., Chaplin W. J., Jones C. D., 2015, ApJ, 806, 30

Lund M. N., et al., 2016, MNRAS, 463, 2600

Maeder A., 1975, A&A, 40, 303

Maldonado J., Villaver E., Eiroa C., 2013, A&A, 554, A84

Mandel K., Agol E., 2002, ApJ, 580, L171

Marois C., Macintosh B., Barman T., Zuckerman B., Song I., Patience J., Lafrenière D., Doyon R., 2008, Science, 322, 1348

Marois C., Zuckerman B., Konopacky Q. M., Macintosh B., Barman T., 2010, Nature, 468, 1080

Martin R. G., Livio M., 2012, MNRAS, 425, L6

Martin R. G., Livio M., 2013, MNRAS, 434, 633

Massarotti A., 2008, AJ, 135, 2287

Masset F., Snellgrove M., 2001, MNRAS, 320, L55

Mathur S., Turck-Chièze S., Couvidat S., García R. A., 2007, ApJ, 668, 594

Mathur S., et al., 2010, A&A, 511, A46

Mathur S., et al., 2011, ApJ, 741, 119

Mayor M., Queloz D., 1995, Nature, 378, 355

McQuillan A., Mazeh T., Aigrain S., 2014, ApJS, 211, 24

McWilliam A., 1990, ApJS, 74, 1075

Meech K. J., et al., 2017, Nature, p. nature25020

Miglio A., et al., 2012, MNRAS, 419, 2077

Miglio A., Chaplin W. J., Farmer R., Kolb U., Girardi L., Elsworth Y., Appourchaux T., Handberg R., 2014, ApJ, 784, L3

Montalbán J., Miglio A., Noels A., Dupret M.-A., Scuflaire R., Ventura P., 2013, ApJ, 766, 118

Mortier A., Santos N. C., Sousa S. G., Adibekyan V. Z., Delgado Mena E., Tsantaki M., Israelian G., Mayor M., 2013, A&A, 557, A70

Morton T. D., Winn J. N., 2014, ApJ, 796, 47

Mosser B., et al., 2011, A&A, 532, A86

Mosser B., et al., 2012a, A&A, 537, A30

Mosser B., et al., 2012b, A&A, 540, A143

Mosser B., et al., 2012c, A&A, 548, A10

Mosser B., et al., 2016, preprint, (arXiv:1610.03872)

Mullally F., Barclay T., Barentsen G., 2016, K2fov: Field of view software for NASA's K2 mission, Astrophysics Source Code Library (ascl:1601.009)

Murphy S., 2014, Investigating the A-Type Stars Using Kepler Data. Springer Theses, Springer International Publishing, https://books.google.co.uk/books?id=HfuSBAAAQBAJ

North T. S. H., et al., 2017a, MNRAS, 465, 1308

North T. S. H., et al., 2017b, MNRAS, 472, 1866

O'Toole S. J., Tinney C. G., Jones H. R. A., 2008, MNRAS, 386, 516

Oshagh M., et al., 2017, A&A, 606, A107

Otor O. J., et al., 2016, AJ, 152, 165

Paxton B., Bildsten L., Dotter A., Herwig F., Lesaffre P., Timmes F., 2011, ApJS, 192, 3

Paxton B., et al., 2013, ApJS, 208, 4

Perryman M., 2011, The Exoplanet Handbook

Perryman M. A. C., et al., 1997, A&A, 323, L49

Perryman M., Hartman J., Bakos G. Á., Lindegren L., 2014, ApJ, 797, 14

Petrovich C., 2015, ApJ, 805, 75

Pickles A. J., 1998, PASP, 110, 863

Pijpers F. P., 2003, A&A, 400, 241

Pinsonneault M. H., et al., 2014, ApJS, 215, 19

Pollack J. B., Hubickyj O., Bodenheimer P., Lissauer J. J., Podolak M., Greenzweig Y., 1996, Icarus, 124, 62

Pols O. R., Schröder K.-P., Hurley J. R., Tout C. A., Eggleton P. P., 1998, MNRAS, 298, 525

Quinn S. N., et al., 2015, ApJ, 803, 49

Quirrenbach A., Reffert S., Trifonov T., Bergmann C., Schwab C., 2015, in AAS/Division for Extreme Solar Systems Abstracts. p. 502.01

Rauer H., et al., 2014, Experimental Astronomy, 38, 249

Reffert S., Quirrenbach A., Mitchell D. S., Albrecht S., Hekker S., Fischer D. A., Marcy G. W., Butler R. P., 2006, ApJ, 652, 661

Reffert S., Bergmann C., Quirrenbach A., Trifonov T., Künstler A., 2015, A&A, 574, A116

Ricker G. R., et al., 2014, in Society of Photo-Optical Instrumentation Engineers (SPIE) Conference Series. p. 20 (arXiv:1406.0151), doi:10.1117/12.2063489

Ricker G. R., et al., 2015, Journal of Astronomical Telescopes, Instruments, and Systems, 1, 014003

Robertson P., Mahadevan S., Endl M., Roy A., 2014, Science, 345, 440

Robinson S. E., et al., 2007, ApJ, 670, 1391

Rodrigues T. S., et al., 2014, MNRAS, 445, 2758

Rodrigues T. S., et al., 2017, MNRAS, 467, 1433

Rogers F. J., Nayfonov A., 2002, ApJ, 576, 1064

Rybicki K., Denis C., 2001, Icarus, 151, 130

Saar S. H., Butler R. P., Marcy G. W., 1998, ApJ, 498, L153

Salaris M., Cassisi S., 2005, Evolution of Stars and Stellar Populations. Wiley, https://books.google.co.uk/books?id=p4ojTNkcFx8C

Sandquist E. L., Dokter J. J., Lin D. N. C., Mardling R. A., 2002, ApJ, 572, 1012

Savitzky A., Golay M. J. E., 1964, Analytical Chemistry, 36, 1627

Schlafly E. F., Finkbeiner D. P., 2011, ApJ, 737, 103

Schlaufman K. C., Winn J. N., 2013, ApJ, 772, 143

Schlaufman K. C., Winn J. N., 2016, ApJ, 825, 62

Schlegel D. J., Finkbeiner D. P., Davis M., 1998, ApJ, 500, 525

Schröder K.-P., Connon Smith R., 2008, MNRAS, 386, 155

Schwarz G., 1978, Ann. Statist., 6, 461

Seager S., Mallén-Ornelas G., 2003, ApJ, 585, 1038

Setiawan J., Pasquini L., da Silva L., Hatzes A. P., von der Lühe O., Girardi L., de Medeiros J. R., Guenther E., 2004, A&A, 421, 241

Shporer A., et al., 2016, ApJ, 829, 34

Silva Aguirre V., et al., 2015, MNRAS, 452, 2127

Silvotti R., et al., 2007, Nature, 449, 189

Sing D. K., 2010, A&A, 510, A21

Smalley B., 2005, Memorie della Societa Astronomica Italiana Supplementi, 8, 130

Smith J. C., et al., 2012, PASP, 124, 1000

Sneden C. A., 1973, PhD thesis, THE UNIVERSITY OF TEXAS AT AUSTIN.

Soubiran C., Le Campion J.-F., Brouillet N., Chemin L., 2016, A&A, 591, A118

Sousa S. G., 2014, ARES + MOOG: A Practical Overview of an Equivalent Width (EW) Method to Derive Stellar Parameters. pp 297–310, doi:10.1007/978-3-319-06956-2˙26

Sousa S. G., Santos N. C., Israelian G., Mayor M., Monteiro M. J. P. F. G., 2007, A&A, 469, 783

Sousa S. G., et al., 2008, A&A, 487, 373

Sousa S. G., Santos N. C., Israelian G., Mayor M., Udry S., 2011, A&A, 533, A141

Sousa S. G., Santos N. C., Adibekyan V., Delgado-Mena E., Israelian G., 2015, A&A, 577, A67

Spiegel D. S., Burrows A., Milsom J. A., 2011, ApJ, 727, 57

Stassun K. G., Torres G., 2016, preprint, (arXiv:1609.05390)

Steffen J. H., et al., 2013, MNRAS, 428, 1077

Stello D., et al., 2013a, ApJ, 765, L41

Stello D., et al., 2013b, ApJ, 765, L41

Stello D., et al., 2015, ApJ, 809, L3

Stello D., Cantiello M., Fuller J., Huber D., García R. A., Bedding T. R., Bildsten L., Silva Aguirre V., 2016, Nature, 529, 364

Stetson P. B., Pancino E., 2008, PASP, 120, 1332

Stumpe M. C., et al., 2012, PASP, 124, 985

Stumpe M. C., Smith J. C., Catanzarite J. H., Van Cleve J. E., Jenkins J. M., Twicken J. D., Girouard F. R., 2014, PASP, 126, 100

Szentgyorgyi A. H., Furész G., 2007, in Kurtz S., ed., Revista Mexicana de Astronomia y Astrofisica Conference Series Vol. 28, Revista Mexicana de Astronomia y Astrofisica Conference Series. pp 129–133

Takeda Y., Sato B., Murata D., 2008, PASJ, 60, 781

Tassoul M., 1980, ApJS, 43, 469

Thommes E. W., Duncan M. J., Levison H. F., 2002, AJ, 123, 2862

Thompson S. E., et al., 2012, ApJ, 753, 86

Thompson S. E., Christiansen J. L., Jenkins J. M., Caldwell D. A., Barclay T., Bryson S. T., Burke C. J., Campbell J. R., 2013, Kepler Data Release 21, (KSCI-19061-001)

Torres G., 2010, AJ, 140, 1158

Torres G., Fischer D. A., Sozzetti A., Buchhave L. A., Winn J. N., Holman M. J., Carter J. A., 2012a, ApJ, 757, 161

Torres G., Fischer D. A., Sozzetti A., Buchhave L. A., Winn J. N., Holman M. J., Carter J. A., 2012b, ApJ, 757, 161

Tsantaki M., Sousa S. G., Adibekyan V. Z., Santos N. C., Mortier A., Israelian G., 2013, A&A, 555, A150

Udry S., Fischer D., Queloz D., 2007, Protostars and Planets V, pp 685–699

Ulrich R. K., 1986, ApJ, 306, L37

Upper D., 1974, Journal of Applied Behavior Analysis, 7, 497

Valenti J. A., Fischer D. A., 2005, ApJS, 159, 141

Valenti J. A., Piskunov N., 1996, A&AS, 118, 595

Van Eylen V., Albrecht S., 2015, ApJ, 808, 126

Van Eylen V., et al., 2014, preprint, (`arXiv:1412.4848`)

Van Eylen V., et al., 2016, AJ, 152, 143

Veras D., 2016, preprint, (`arXiv:1601.05419`)

Verner G. A., et al., 2011, MNRAS, 415, 3539

Viani L. S., Basu S., Chaplin W. J., Davies G. R., Elsworth Y., 2017, ApJ, 843, 11

Vogt S. S., et al., 1994, in Crawford D. L., Craine E. R., eds, Proc. SPIEVol. 2198, Instrumentation in Astronomy VIII. p. 362, doi:10.1117/12.176725

Vrard M., Mosser B., Samadi R., 2016, A&A, 588, A87

Walsh K. J., Morbidelli A., Raymond S. N., O'Brien D. P., Mandell A. M., 2011, Nature, 475, 206

Welsh W. F., et al., 2011, ApJS, 197, 4

Winn J. N., 2010, preprint (`arXiv:1001.2010`)

Wittenmyer R. A., Endl M., Wang L., Johnson J. A., Tinney C. G., O'Toole S. J., 2011, ApJ, 743, 184

Wittenmyer R. A., Liu F., Wang L., Casagrande L., Johnson J. A., Tinney C. G., 2016, AJ, 152, 19

Wolszczan A., Frail D. A., 1992, Nature, 355, 145

Wright J. T., 2005, PASP, 117, 657

da Silva L., et al., 2006, A&A, 458, 609

de Mooij E. J. W., et al., 2012, A&A, 538, A46

van Leeuwen F., 2007, A&A, 474, 653

van de Kamp P., 1963, AJ, 68, 515

van de Kamp P., 1969, AJ, 74, 757